



NATIONAL TECHNICAL UNIVERSITY OF ATHENS
SCHOOL OF ELECTRICAL AND COMPUTER ENGINEERING
DIVISION OF SIGNALS, CONTROL AND ROBOTICS
COMPUTER VISION, SPEECH COMMUNICATION AND SIGNAL PROCESSING GROUP

Improving the HESS-IU Camera calibration

DIPLOMA THESIS

of

Despoina Mousadi

Supervisor : Petros Maragos
Professor NTUA

Co-supervisors : Dmitriy Kostunin
Researcher at DESY

Gianluca Giavitto
Researcher at DESY

Stefan Ohm
Researcher at DESY

Athens, October 2023



National Technical University of Athens
School of Electrical and Computer Engineering
Division of Signals, Control and Robotics
Computer Vision, Speech Communication and Signal Processing Group

Improving the HESS-IU Camera calibration

DIPLOMA THESIS

of

Despoina Mousadi

Supervisor : Petros Maragos
Professor NTUA

Co-supervisors : Dmitriy Kostunin
Researcher at DESY

Gianluca Giavitto
Researcher at DESY

Stefan Ohm
Researcher at DESY

Approved by the Examining Committee on the 20th October, 2023.

.....
Petros Maragos
Professor NTUA

.....
Gerasimos Potamianos
Assoc. Professor UTH

.....
Konstantinos Tzafestas
Assoc. Professor NTUA

Athens, October 2023

.....
DESPOINA MOUSADI
Electrical and Computer Engineering Graduate, NTUA

Copyright © – All rights reserved Despoina Mousadi, 2023.
All rights reserved.

This work is copyright and may not be reproduced, stored nor distributed in whole or in part for commercial purposes. Permission is hereby granted to reproduce, store and distribute this work for non-profit, educational and research purposes, provided that the source is acknowledged and the present copyright message is retained. Enquiries regarding use for profit should be directed to the author.

The views and conclusions contained in this document are those of the author and should not be interpreted as representing the official policies, either expressed or implied, of the National Technical University of Athens.

Περίληψη

Η αστρονομία των ακτίνων γάμμα, η μελέτη της πιο υψηλής ενέργειας μορφής της ηλεκτρομαγνητικής ακτινοβολίας που εκπέμπεται από κοσμικές πηγές, έχει δει σημαντικές επιστημονικές και τεχνολογικές επιτυχίες τις τελευταίες δεκαετίες. Ένα από τα κορυφαία αστρονομικά παρατηρητήρια για τις ακτίνες γάμμα είναι το High Energy Stereoscopic System (H.E.S.S.), ένα σύστημα πέντε τηλεσκοπίων Cherenkov που βρίσκονται στη Ναμίμπια. Τα τηλεσκόπια μετρούν τη ροή των ακτίνων γάμμα χρησιμοποιώντας μεγάλους καθρέφτες που αντανακλούν το φως Cherenkov, το οποίο παράγεται από τις ηλεκτρομαγνητικές βροχές που προκαλούνται από τις ακτίνες γάμμα, σε ειδικές κάμερες με pixel που αποτελούνται από φωτοπολλαπλασιαστές (PMTs). Το H.E.S.S. λειτουργεί από το 2002, επιτρέποντας στους επιστήμονες να ερευνούν τις ακτίνες γάμμα πολύ υψηλών ενεργειών έως 30 TeV. Η λειτουργία του παρατηρητηρίου χωρίζεται σε δύο φάσεις: Η φάση I του H.E.S.S. αποτελείται από τέσσερα τηλεσκόπια με διάμετρο καθρέφτη 12 μέτρων, ενώ η Φάση II του H.E.S.S. χαρακτηρίζεται από την εγκατάσταση ενός πέμπτου τηλεσκοπίου το 2015 με καθρέφτη 28 μέτρων και χαμηλότερο κατώφλι ενέργειας.

Για να μειωθεί το κατώφλι του συνόλου των τηλεσκοπίων, καθώς και για να χρησιμοποιηθούν νεότερες τεχνολογίες για την πιο αξιόπιστη απόδοση της κάμερας, οι κάμερες των τεσσάρων τηλεσκοπίων H.E.S.S. I έχουν αναβαθμιστεί (HESS-IU). Το πιο σημαντικό κομμάτι της αναβάθμισης είναι το NECTAr chip, που αναπτύχθηκε για το παρατηρητήριο της επόμενης γενιάς, CTA, και δοκιμάστηκε πρώτα στο H.E.S.S.. Αποτελείται από μία αναλογική κυκλική μνήμη, από την οποία τιμές μέσα σε ένα συγκεκριμένο παράθυρο ανάγνωσης διαβάζονται γρήγορα κάθε φορά που υπάρχει ενεργό σήμα ενεργοποίησης. Καθώς η αξιοπιστία των δεδομένων εξαρτάται από την ορθή λειτουργία της κάμερας, η τακτική βαθμονόμηση αποτελεί ένα θεμελιώδες βήμα για την επίτευξη των επιστημονικών στόχων του παρατηρητηρίου.

Σε αυτή τη διπλωματική προτείνουμε κάποιες βελτιώσεις στη βαθμονόμηση της κάμερας HESS-IU. Η πρώτη είναι μια μέθοδος για τη ρύθμιση της θέσης του παραθύρου ανάγνωσης του κάθε pixel υπέρ χαμηλότερων ενεργειακά σημάτων, λαμβάνοντας υπόψη την ένταση των φωτεινών παλμών από τη μονάδα Flat-Fielding του τηλεσκοπίου. Η δεύτερη είναι μια τεχνική για τη βαθμονόμηση του παράγοντα μετατροπής μεταξύ των ADC counts και των μετρημένων φωτοηλεκτρονίων, δηλαδή του κέρδους του κάθε PMT, με την υπόθεση ότι υπάρχει γραμμική σχέση μεταξύ του κέρδους και της τάσης του PMT. Οι δύο προσεγγίσεις χρησιμοποιούν μια global fitting μέθοδο για τα δεδομένα, όπου δείγματα της έντασης ή του φορτίου του ίδιου pixel δεν θεωρούνται ανεξάρτητα και συνεπώς γίνονται fitted σε μια συνάρτηση παράλληλα αντί για σειριακά. Η αποτελεσματικότητα των προτεινόμενων τακτικών έχει δοκιμαστεί, δίνοντας βελτιωμένη χρονική ομοιομορφία μεταξύ των τηλεσκοπίων και συνεπή αποτελέσματα σε σχέση με τον προηγούμενο χρησιμοποιούμενο αλγόριθμο, ενώ επιταχύνει και σταθεροποιεί τις σχετικές διαδικασίες βαθμονόμησης.

Ένας άλλος στόχος αυτής της εργασίας είναι να δείξει ότι είναι δυνατόν να ανακατασκευάσουμε ατελή δεδομένα που έχουν επηρεαστεί από ένα λανθασμένα βαθμονομημένο παράθυρο ανάγνωσης, όπως συνέβη μετά από μια αλλαγή στο υλικό της κάμερας. Χρησιμοποιώντας ειδικά runs βαθμονόμησης με φωτεινούς παλμούς διαφορετικής έντασης, παραμετροποιούμε το φορτίο ολόκληρου του σήματος 16 ns, χρησιμοποιώντας το φορτίο που μετρήθηκε 9 ns γύρω από την κορυφή του σήματος. Στη συνέχεια εξάγουμε τους συντελεστές ανακατασκευής που μπορούν να χρησιμοποιηθούν για την ανάκτηση του ελλιπούς μέρους των δεδομένων. Αυτή η παραμετροποίηση δοκιμάστηκε χρησιμοποιώντας δεδομένα από πραγματικές παρατηρήσεις, δείχνοντας ότι αυτή η προσέγγιση έχει καλές προοπτικές, αφού ληφθούν υπόψη οι συνθήκες στις οποίες γίνονται οι παρατηρήσεις (θόρυβος, υπόβαθρο νυχτερινού ουρανού κ.α.).

Λέξεις Κλειδιά — Αστρονομία ακτίνων γάμμα, τηλεσκόπια Cherenkov, High Energy Stereoscopic System, βαθμονόμηση, NECTAr

Abstract

Gamma-ray astronomy, the study of the most energetic form of electromagnetic radiation emitted from cosmic sources, has witnessed significant scientific and engineering accomplishments through the last decades. One of the leading gamma-ray observatories is the High Energy Stereoscopic System (H.E.S.S.), an array of five Imaging Atmospheric Cherenkov Telescopes located in Namibia. The telescopes measure the flux of gamma-rays using large mirrors which reflect the Cherenkov light produced by gamma-ray induced electromagnetic showers on special cameras with pixels consisting of photomultiplier tubes (PMTs). It has been collecting data since 2002, allowing scientists to investigate gamma-rays with very high energies up to 30 TeV. The observatory's operation is split into two phases: H.E.S.S. Phase I consists of four telescopes with a 12 m mirror diameter, while H.E.S.S. Phase II is characterised by the installation of a fifth 28 m telescope with a lower energy threshold in 2015.

In order to decrease the threshold of the array altogether, as well as use newer technologies for more reliable camera performance, the cameras of the four H.E.S.S. I telescopes have been upgraded (HESS-IU). The most important component of the upgrade is the NECTAR readout chip, developed for the next generation observatory, CTA, and first tested on H.E.S.S.. It consists of an analogue memory cyclical buffer, from which values inside a specific readout window are swiftly read out whenever there is an active trigger signal. Since the reliability of the data depends on the proper function of the camera, regular calibration is a fundamental step in achieving the observatory's scientific goals.

In this thesis we propose some improvements in the calibration of the HESS-IU camera. The first one is a method to adjust the position of the readout window of each pixel towards lower energy signals, taking into consideration the intensity of the light pulses from the telescope's Flat-Fielding unit. The second one is a technique for the calibration of the ratio factor between ADC counts and measured photoelectrons, in other words the gain of each PMT, under the hypothesis that there is a linear relationship between gain and PMT voltage. The two approaches use a global data fitting method, where samples of the intensity or charge of the same pixel are not considered independent and hence are fitted to a function in parallel instead of serially. The efficiency of the proposed schemes has been tested, giving improved time uniformity between telescopes and consistent results with the previously used algorithm, while speeding up and stabilising the relevant calibration processes.

Another goal of this work is to show that it is possible to reconstruct incomplete data affected by a miscalibrated readout window, as was the case after a hardware change. Using special calibration runs with light pulses of different intensities, we parametrise the charge of the whole signal of 16 ns, using the charge measured 9 ns around the peak of the signal. We then deduce reconstruction coefficients which can be used to recover the missing part of the data. The parametrisation is tested using observation data, showing that this approach has a great potential after accounting for real observation conditions (pedestals, night sky background, etc).

Keywords — Gamma-ray astronomy, Imaging Atmospheric Cherenkov Telescopes, High Energy Stereoscopic System, calibration, NECTAR

Acknowledgements

This thesis marks the end of my five years as a student at the School of Electrical and Computer Engineering at the National Technical University of Athens. I would like to thank the following people for helping me throughout this journey:

Prof. Petros Maragos, for supervising this thesis. His courses were the ones that made me interested in the field of signal processing and without this knowledge I would not have been able to complete this work.

Dr. Dmitriy Kostunin, Dr. Gianluca Giavitto and Dr. Stefan Ohm from the H.E.S.S. group at DESY (Deutsches Elektronen Synchrotron) for welcoming me as a part of the team, coming up with this project and trusting me to complete it. Especially Dima's help has been very important for me, for all his regular guidance, advice and understanding through the last year.

My family and friends for their continuous support.

Table of Contents

Table of contents	11
List of figures	13
List of tables	17
Εκτεταμένη Περίληψη στα Ελληνικά	18
1 Introduction	43
1.1 Gamma-Ray Astronomy	44
1.1.1 Cosmic accelerators	44
1.1.2 Why Gamma Rays?	44
1.1.3 Generation mechanisms of γ -rays	45
1.1.4 Sources of VHE γ -rays	46
1.2 But how can we detect these photons?	48
1.3 Goals and organisation of the thesis	49
2 Very High Energy γ-ray ground-based detection	51
2.1 Introduction	52
2.2 Atmospheric showers	52
2.2.1 Processes involved in the development of showers	52
2.2.2 Cherenkov radiation	53
2.3 Detection techniques	55
2.3.1 Photomultiplier tubes	57
2.3.2 Sampling experiments	58
2.3.3 Imaging Atmospheric Cherenkov Telescopes	58
2.4 The H.E.S.S. experiment	59
2.4.1 The H.E.S.S. telescopes	61
2.4.2 H.E.S.S. Phase I	61
2.4.3 H.E.S.S. Phase II	63
2.4.4 Camera upgrades	65
2.4.5 Central trigger system, data acquisition and monitoring	66
2.4.6 Event selection	67
2.5 The next generation observatory: CTA	67
3 The HESS-IU Camera	69
3.1 Introduction	70
3.2 Architecture of the HESS-IU Camera	70
3.2.1 Front-end electronics	70
3.2.2 Back-end electronics	74
3.2.3 Sensors and calibration devices	76
3.2.4 Camera network and software	77
3.3 Camera calibration	77
3.3.1 Readout	77
3.3.2 Pixel calibration parameters	78

3.3.3	Trigger	80
4	Improving the HESS-IU Calibration	83
4.1	Introduction	84
4.2	Flat Field calibration and readout window adjustment	84
4.2.1	Flat Field calibration	84
4.2.2	Global fit vs local fit	84
4.2.3	Readout window adjustment taking into account the intensity of the FF LED	85
4.2.4	Results	91
4.3	Adjusting Single Photoelectron gain calibration with a global fit	91
4.3.1	Converting ADC counts to photoelectrons	92
4.3.2	Model of the photomultiplier response	92
4.3.3	SPE Calibration	93
4.3.4	Another global fit, assuming linear gain	93
4.3.5	Results and comparison to standard algorithm	95
5	Sample mode to charge mode converter	99
5.1	Introduction	100
5.2	Charge recovery and a few integrals	100
5.3	Calibration and recovery coefficients	100
5.4	Cross-check with observation data	101
6	Conclusion	109
6.1	Summary and conclusions	110
6.2	Limitations and future work	110
6.3	Future application of technique and impact on CTA	110
	Bibliography	115

List of figures

0.0.1	Local fitting scheme: κάθε δείγμα γίνεται fitted ξεχωριστά, με διαφορετική κατανομή θορύβου, η οποία αφαιρείται από κάθε δείγμα.	23
0.0.2	Global fitting scheme: μία κατανομή θορύβου περιγράφει ταυτόχρονα και τα 16 δείγματα, με ξεχωριστές κατανομές γάμμα για το χρήσιμο σήμα, σε αντίθεση με τον προηγούμενο αλγόριθμο. Ο ίδιος θόρυβος αφαιρείται από όλα τα δείγματα.	23
0.0.3	ROOT5 ιστογράμματα για ένα pixel. Πάνω: Αρχικό ROOT5 format. Ο οριζόντιος άξονας αντιπροσωπεύει τον χρόνο, δίνοντας τον αριθμό κάθε δείγματος του 1 ns, ενώ ο κάθετος άξονας αντιπροσωπεύει πλάτος σε ADC counts. Τα ADC counts για κάθε δείγμα δίνονται ως ιστογράμματα. Κάτω: Προβολή των ιστογραμμάτων για τα δείγματα στα 6 και 10 ns, με το καθένα να αντιστοιχεί σε μία κάθετη λωρίδα του πάνω σχήματος.	25
0.0.4	Ακολουθία δειγμάτων fitted με το άθροισμα μία κανονικής (pedestal) και μιας γάμμα κατανομήσ (χρήσιμο σήμα). Το αρχικό σήμα φαίνεται με τη μπλε συνεχή γραμμή, η κανονική και οι γάμμα κατανομές φαίνονται με διακεκομμένη μπλε και πράσινη γραμμή αντίστοιχα, ενώ η συνολική συνάρτηση μοντελοποίησης με κόκκινη συνεχή γραμμή.	27
0.0.5	Ανακατασκευασμένοι παλμοί πάνω σε ιστογράμματα τύπου ROOT. Πάνω αριστερά: CT1 pixel 255, Πάνω δεξιά: CT2 pixel 7, Κάτω αριστερά: CT3 pixel 684, Κάτω δεξιά: CT4 pixel 778 . . .	28
0.0.6	Παλμός για το CT1 pixel 255, με το κατώφλι των 5,5 p.e. και χρονοσφραγίδα στα 7 ns. . . .	28
0.0.7	Ιστογράμματα προτεινόμενων μετατοπίσεων του παραθύρου ανάγνωσης.	29
0.0.8	Global fit στο κέρδος του CT2 pixel 0, σε λογαριθμική κλίμακα. Το αρχικό σήμα φαίνεται με τη σκούρα μπλε γραμμή, ενώ οι διαφορετικές κανονικές κατανομές που αντιστοιχούν σε διαφορετικές τιμές φωτοηλεκτρονίων (p.e.) φαίνονται με διαφορετικό χρώμα η κάθε μία. Η τελική κατανομή φαίνεται με κόκκινο. Πάνω αριστερά: run 0 ($dV = -20$) ; Πάνω δεξιά: run 2 ($dV = -10$); Κάτω: run 8 $dV = +15$	32
0.0.9	Ευθεία κέρδους μετά το global fit για CT2 pixel 0. Για μηδενική προσαρμογή στην τάση, το κέρδος είναι μερικά ADC counts κάτω από το 60.	32
0.0.10	1D και 2D ιστογράμματα των προτεινόμενων αλλαγών σε τάση για τα CT1-4 σύμφωνα με τον καινούργιο και τον παλιό αλγόριθμο.	33
0.0.11	Ιστογράμματα των συντελεστών διόρθωσης.	35
0.0.12	Μέση τιμή και τυπική απόκλιση των συντελεστών.	36
0.0.13	Συντελεστές σε σχέση με ένταση του φωτός. Υπάρχει μεγαλύτερη αβεβαιότητα για τα πρώτα 2 runs, αλλά ελαχιστοποιείται στις μεγαλύτερες εντάσεις.	36
0.0.14	Cross-check ανάμεσα στο πραγματικό q_{16} των δεδομένων βαθμονόμησης και στο ανακατασκευασμένο q_{16} για τιμές χρόνου κορυφής από 7 ως 15 ns.	37
0.0.15	Αναλογία μεταξύ της πραγματικής τιμής q_{16} από τα δεδομένα παρατήρησης έναντι της ανακατασκευασμένης τιμής του χρησιμοποιώντας το q_9 και τους συντελεστές μας, σε σχέση με τον χρόνο της κορυφής. Τα διαγράμματα αντιστοιχούν σε διάφορικά pixel των τεσσάρων τηλεσκοπίων. Τιμές διάφορες από το 1 για μεγαλύτερη απόκλιση στη θέση της κορυφής υπονοούν την ύπαρξη θορύβου. Επάνω αριστερά: CT1, Επάνω δεξιά: CT2, Κάτω αριστερά: CT3, Κάτω δεξιά: CT4.	38
0.0.16	Σύγκριση μεταξύ της πραγματικής και της ανακατασκευασμένης έντασης από τα δεδομένα παρατήρησης. Καθώς ο χρόνος της μέγιστης έντασης αυξάνεται, υπάρχει μεγαλύτερη αβεβαιότητα. Επάνω αριστερά: CT1, $t=11$, Επάνω δεξιά: CT2, $t=9$, Κάτω αριστερά: CT4, $t=9$, Κάτω δεξιά: CT4, $t=19$	39

0.0.17	Αναλογία μεταξύ της πραγματικής και της ανακατασκευασμένης τιμής q_{16} από τα δεδομένα παρατήρησης σε σχέση με την ένταση. Βλέπουμε ότι για χαμηλότερη ένταση υπάρχει μεγαλύτερη αβεβαιότητα, όπως ήταν και στην περίπτωση του ελέγχου μας χρησιμοποιώντας μόνο δεδομένα βαθμονόμησης. Επίσης, καθώς ο χρόνος της κορυφής αυξάνεται, υπάρχει μεγαλύτερη αβεβαιότητα, πιθανώς λόγω θορύβου. Επάνω αριστερά: CT1, t=13, Επάνω δεξιά: CT2, t=3, Κάτω αριστερά: CT3, t=10, Κάτω δεξιά: CT3, t=15.	40
1.1.1	Energy spectrum of cosmic rays. The vertical axis indicates cosmic ray flux, which decreases with increasing particle energy. On the horizontal axis we see a comparison with the particle center of mass energy of colliders. Very high energy cosmic rays have a significantly higher energy than that of LHC (Large Hadron Collider). From [17].	44
1.1.2	Electromagnetic spectrum, relative wavelength size and sources. Gamma rays are at the higher energy part of the spectrum. Cherenkov telescopes are able to detect very high energy cosmic sources from the ground. Image from the website of the Cherenkov Telescope Array (CTA) observatory[7].	45
1.1.3	The H.E.S.S. Galactic Plane Survey (HGPS), with data from H.E.S.S. observations until 2016 superimposed with the data from previous surveys by HEGRA and VERITAS experiments, as well as data from FermiLAT, of which galactic sources are marked with triangles, while extragalactic sources are marked with stars. Figure from [3]	47
1.1.4	Predicted extragalactic sources to be detected by the CTA Observatory. From [19].	48
2.2.1	Schematic representation of an electromagnetic air shower. From [26]	52
2.2.2	Top: Simulation of 10 electromagnetic showers initiated each by a γ -ray of 300 GeV. Bottom: Simulation of 10 electromagnetic showers initiated each by a proton of 300 GeV, showing larger fluctuations. From [28].	54
2.2.3	Illustration of Cherenkov radiation. Left: spherical wavefronts of radiation from a charged particle moving with a velocity less than the velocity of light through the dielectric medium. Right: conical wavefronts of radiation from a charged particle moving with a higher velocity than that of light. From [4].	55
2.2.4	Shower development and generation of Cherenkov light pool. From [27]	56
2.3.1	Elements of a photomultiplier tube (PMT). From [29].	57
2.3.2	Left: Layout of the HAWC tanks. The green tanks correspond to its VAMOS (Verification And Measuring of Observatory System) array. Right: Operating principle of the Water Cherenkov Technique: relativistic charged particles constituting an air shower front emit Cherenkov radiation with an angle θ_c as they travel through the water. PMTs at the bottom of the tank detect this Cherenkov radiation. From [31].	58
2.3.3	Schematic illustration of the IACT technique. Telescopes detect an extensive air shower induced by a high energy gamma-ray. The source is depicted with a yellow star, while the red tracks denote the paths of the secondary particles. The Cherenkov light pool on the ground is depicted with black. From [36].	60
2.3.4	The stereoscopic technique, where different telescopes view the same shower from different angles, allows more reliable geometric reconstruction of the shower and its properties. The images of all telescopes are superimposed in order to find the actual impact point. From [36].	60
2.4.1	A timeline illustrating the major hardware updates of H.E.S.S. From [37].	61
2.4.2	An overview of the H.E.S.S. array, with CT1-4 arranged in a square and CT5 in the middle. From [36].	62
2.4.3	One of the first Cherenkov images recorded by CT1 in 2002, illustrating a typical elongated view of an air shower. From [6].	63
2.4.4	A 12 meter H.E.S.S. Phase I telescope. From [6].	64
2.4.5	Technical designs of H.E.S.S. Phase I telescopes. From [6].	64
2.4.6	Mirror facets of a H.E.S.S. I telescope. From [6].	65
2.4.7	The 28 m H.E.S.S. Phase II telescope. From [6].	66
3.2.1	Left: The first upgraded H.E.S.S. I camera, on CT1. Right: Rear view of the camera, with open back door. Figure from [10].	70

3.2.2	Illustration of the H.E.S.S. I Upgrade architecture. Green-colored lines indicate original components, blue-colored lines represent commercial custom-made components, and orange-colored lines denote commercially available off-the-shelf components. The red lines correspond to power distribution, and the arrows indicate the direction of power flow. If labeled as "Optical Fiber," the arrows represent bidirectional optical fiber links. Additionally, green lines with circle terminations signify copper Ethernet links, and black lines with arrows represent electrical signals. To mark the physical locations of subsystems, light grey boxes are used: "HESS1U Camera" refers to the camera body, the "Telescope Shelter" represents the camera daytime parking shelter, the "Telescope Hut" is a service container linked to the telescope structure, and the "Farm" denotes the server room within the array control building. Figure from [10].	71
3.2.3	Top: Partially assembled drawer and important components. Bottom: Fully assembled drawer. From [10].	72
3.2.4	Left: Partial view of an analogue board. The signal amplification components are marked with light green, while the NECTAR chips appear in black colour. Right: detailed view of the NECTAR chip. From [10].	73
3.2.5	Left: rear view of the inside of HESS-IU. Right: Camera cabling; the Ethernet cables are red, the trigger and clock cables are blue, while the power cables are black. All of the above are connected to the drawer connection boards. From [10].	73
3.2.6	Left: Drawer interface box with open top lid, showing the analogue board, which is on top of the main and front panel boards, while the GPS module is located at the back. Right: Power distribution box. From [10].	75
3.2.7	Left: Digitised PMT pulse from a flat-field run, showing the distribution of around 2000 light pulses. The red line corresponds to a spline interpolation of the mean value for every sample, with the FWHM shown with dashed lines. Right: Charge distribution from an SPE run, fitted to a linear combination of Gaussians. From [10].	76
3.3.1	Left: Sample baseline of NECTAR capacitor array line before calibration. Right: Baseline after 5 iterations of calibration process. There is an evident decrease in the baseline RMS value. From [10].	78
3.3.2	Impact of night sky background on pedestal width. From [9]	80
3.3.3	Sigmoid curves of pixel (left) and sector (right) trigger efficiency, for different thresholds P and Q . Thresholds are given in DAC counts (0.76 mV/count). The lower insets show the linear relationship between sigmoid centers and illumination (in p.e.) and active pixels respectively. From [10].	81
3.3.4	Results of a threshold scan during a Galactic source observation under regular NSB, showing trigger rate versus pixel threshold in photo-electrons. From [10].	82
4.2.1	Local fitting scheme: each sample is fitted separately, with an individual pedestal distribution. This results in a different pedestal being subtracted from each sample.	85
4.2.2	Global fitting scheme: one pedestal noise distribution is fitted simultaneously for all 16 samples, along with their separate useful signal gamma distributions, in contrast to the previous algorithm. The same pedestal is subtracted from each individual sample.	86
4.2.3	ROOT5 format histograms for a pixel. Top: Original ROOT5 format. The horizontal axis represents time, giving the number of each 1 ns sample, while the vertical axis represents amplitude in ADC counts. The ADC counts for each sample are given in histograms. ; Bottom: Profiled histograms for samples at 6 and 10 ns, each representing one vertical slice of the previous plot.	87
4.2.4	Sequence of samples fitted to sum of gaussian (pedestal) and gamma distribution (useful signal). The original signal is shown with blue solid line, the gaussian and the gamma distributions with dashed blue and green lines respectively, and the overall modelling function with a red solid line.	89
4.2.5	Recreated pulses on ROOT format histograms. Top left: CT1 pixel 255 ; Top right: CT2 pixel 7 ; Bottom left: CT3 pixel 684 ; Bottom right: CT4 pixel 778	90
4.2.6	Pulse for CT1 pixel 255, indicating trigger threshold at 5.5 p.e. and 7 ns timestamp.	90
4.2.7	Histograms of proposed shifts in readout window positioning.	91

4.3.1	Global fit on gain for runs from $dV = -20$ to $dV = +20$ for CT2 pixel 0, in logarithmic scale. The original signal is marked with a dark blue line, while the different gaussian distributions corresponding to different p.e. values are marked each with a different colour. The resulting distribution is shown with red. It describes the data well, with the gain (in ADC counts) increasing as the voltage increases.	94
4.3.2	Resulting gain line after global fit for CT2 pixel 0. For zero adjustment to voltage, the gain is a few ADC counts below 60.	95
4.3.3	Histograms of PMT gain values for all telescopes. Most pixels need correction, as their gain value does not coincide with the desired value.	96
4.3.4	1D and 2D histograms of proposed changes in pixel gain in Volts for CT1-4 according to new and old algorithm.	97
5.3.1	Pulse from the SPE unit used for the calculation of charge recovery coefficients. The pulse has been fitted to an analytical function after removing the pedestal offset and calculating the mean value of the ADC distribution for each sample.	101
5.3.2	Histograms of correction coefficients from q_9 to q_{16}	102
5.3.3	Mean coefficients with standard deviation. If the pulse is shifted only by a few ns, q_{16} almost equal to q_9 , while for time of peak higher than 12, their ratio steeply falls to zero.	103
5.3.4	Coefficients in relation to run (with rising light intensity). There is a higher uncertainty for the first two runs, but it is diminished when the runs have higher intensity.	103
5.3.5	Cross-check between true q_{16} of calibration data and reconstructed q_{16} for different readout window positions.	104
5.4.1	Ratio between true q_{16} from observation data versus its reconstructed value using q_9 and our coefficients, in relation to time of peak. The plots correspond to different pixels of the four telescopes. Values different than 1 for higher time offset imply the existence of noise. Top left: CT1; Top right: CT2; Bottom left: CT3; Bottom right: CT4.	105
5.4.2	Comparison between true and reconstructed intensity from observation data. As time of maximum increases, there is higher uncertainty. Top left: CT1, $t=11$; Top right: CT2, $t=9$; Bottom left: CT4, $t=9$; Bottom right: CT4, $t=19$	106
5.4.3	Ratio between true and reconstructed q_{16} from observation data in relation to intensity. We see that for lower intensity there is higher uncertainty, as was the case with our crosscheck using only calibration data. Also, as time of peak increases, there is higher uncertainty, presumably because of noise. Top left: CT1, $t=13$; Top right: CT2, $t=3$; Bottom left: CT3, $t=10$; Bottom right: CT3, $t=15$	107

List of tables

5.1 Reconstruction coefficients for different times of peak. 102

Εκτεταμένη περίληψη στα Ελληνικά

Εισαγωγή

Στη διάρκεια των τελευταίων τριάντα χρόνων, η αστρονομία ακτίνων γ έχει βιώσει πολλές θεωρητικές και τεχνολογικές εξελίξεις, καθιστώντας την ένα ισχυρό μέσο για την εξερεύνηση ορισμένων από τα βαθύτερα μυστήρια του σύμπαντος. Αυτό το πεδίο περιλαμβάνει την παρατήρηση και την ανάλυση των ακτίνων γ κοσμικής προέλευσης, όπως αυτές που εκπέμπονται από πάλσαρς, υπερκαινοφανείς αστέρες και ενεργούς γαλαξιακούς πυρήνες.

Οι κοσμικές ακτίνες ανακαλύφθηκαν για πρώτη φορά από τον V. Hess το 1912. Αποτελούνται από υψηλής ενέργειας σωματίδια ($10^9 - 10^{20}$ eV), κυρίως πρωτόνια και πυρήνες, συνοδευόμενους από ένα μικρό ποσοστό ηλεκτρονίων και ποζιτρονίων, τα οποία προέρχονται από κοσμικές πηγές. Ένα πρόβλημα που σχετίζεται με τα φορτισμένα σωματίδια από τα οποία αποτελούνται οι κοσμικές ακτίνες είναι ότι η πορεία τους αλλάζει συνεχώς λόγω των μαγνητικών πεδίων που συναντούν στον δρόμο τους προς τη Γη. Ως αποτέλεσμα, η αρχική τους κατεύθυνση δεν μπορεί να οριστεί.

Τα σωματίδια που μπορούν να λύσουν το πρόβλημα αυτό είναι τα φωτόνια. Δεδομένου ότι δεν έχουν φορτίο, ταξιδεύουν μέσα από τον διάστημα σε ευθεία γραμμή, επιτρέποντάς μας να ανιχνεύσουμε την προέλευσή τους. Οι υψηλής ενέργειας ακτίνες γ παράγονται ως δευτερεύοντα προϊόντα των υψηλής ενέργειας κοσμικών ακτίνων, καθώς τα συστατικά τους τους αλληλεπιδρούν με το περιβάλλον τους.

Οι ακτίνες γ είναι υψηλής ενέργειας ηλεκτρομαγνητική ακτινοβολία που αντιστοιχεί σε φωτόνια με ενέργειες μεγαλύτερες από 0,5 MeV, ενώ οι υψηλότερες ενέργειες ακτίνων γ που έχουν ανιχνευτεί μέχρι σήμερα φτάνουν τα 1,4 PeV[1]. Βρίσκονται στο άκρο του ηλεκτρομαγνητικού φάσματος με το μικρότερο μήκος κύματος, πέρα από το ορατό φως και τις ακτίνες X. Σε αυτή την εργασία θα επικεντρωθούμε στην αστρονομία των ακτίνων γ πολύ υψηλής ενέργειας (Very High Energy, VHE), με ενέργειες φωτονίων στην κλίμακα των TeV, καθώς αυτές αποτελούν ιχνηλάτες των κοσμικών ακτίνων υψηλής ενέργειας[2].

Ένα παρατηρητήριο που έχει οδηγήσει στην ανίχνευση πολλών πηγών ακτινοβολίας γ είναι το High Energy Stereoscopic System (H.E.S.S.)[3]. Για να αποφευχθούν αναξιόπιστα αποτελέσματα, είναι απαραίτητο να εξασφαλιστεί η σωστή λειτουργία του οπτικού συστήματος των τηλεσκοπίων του H.E.S.S. Συνεπώς, όλα τα στοιχεία των καμερών τους πρέπει να βαθμονομούνται συχνά, για να ελαχιστοποιηθούν οι επιδράσεις από το περιβάλλον, καθώς και από τον χρόνο λειτουργίας τους.

Σε αυτή την εργασία θα ασχοληθούμε με τη βαθμονόμηση των καμερών HESS-IU των τηλεσκοπίων του H.E.S.S., προτείνοντας τρεις αλλαγές που έχουν να κάνουν με τη θέση του readout window, την προσαρμογή του κέρδους των pixel και την ανάκτηση μερικής καταγεγραμμένων δεδομένων.

Ανίχνευση από την επιφάνεια της Γης

Κατά την είσοδο στην ατμόσφαιρα, ένα φωτόνιο υψηλής ενέργειας θα αλληλεπιδράσει με τα άτομά της, προκαλώντας μια ακολουθία γεγονότων: το φωτόνιο θα αλληλεπιδράσει με τον ηλεκτρικό πεδίο των πυρήνων της ατμόσφαιρας, οδηγώντας στην παραγωγή ενός ζεύγους ηλεκτρονίου-ποζιτρονίου. Το ηλεκτρόνιο και το ποζιτρόνιο, κατά την αλληλεπίδρασή τους με το ηλεκτρικό πεδίο, θα οδηγήσουν στην παραγωγή νέων χαμηλότερης (υψηλής) ενεργειας ακτίνων γ . Αυτές οι ακτίνες γ θα παράγουν νέα ζεύγη ηλεκτρονίου-ποζιτρονίου και ούτω καθεξής. Αυτού του τύπου τα γεγονότα συνιστούν μία εκτεταμένη ατμοσφαιρική βροχή (extensive air shower, EAS).

Παρόλο που ένα φορτισμένο σωματίδιο, όπως ένα ηλεκτρόνιο, που κινείται σε ευθεία γραμμή με σταθερή ταχύτητα στο κενό δεν εκπέμπει ακτινοβολία, ένα ηλεκτρόνιο που κινείται ομοιόμορφα μέσα σε ένα διηλεκτρικό μέσο με μια ταχύτητα μεγαλύτερη από τη φασική ταχύτητα του φωτός σε εκείνο το μέσο μπορεί να εκπέμψει ακτινοβολία[4]. Αυτός ο τύπος ακτινοβολίας ονομάζεται ακτινοβολία Cherenkov, και αντιστοιχεί σε ένα πολύ αχνό μπλε φως. Αυτό το φως ανιχνεύεται από τα Imaging Atmospheric Cherenkov Telescopes (IACTs), δείχνοντάς μας την κατεύθυνση της αρχικής ακτίνας γ . Στα IACTs, ένας μεγάλος καθρέφτης συλλέγει τα φωτόνια Cherenkov και τα αντανάκλα στο εστιακό επίπεδο όπου βρίσκεται η κάμερα. Αυτή αποτελείται από φωτοπολλαπλασιαστές (photomultiplier tubes, PMTs), που λειτουργούν ως pixel της κάμερας[5].

Το High Energy Stereoscopic System (H.E.S.S.) είναι ένα σύστημα πέντε IACTs που βρίσκονται στη σαβάνα της Ναμίμπια. Λειτουργεί πλήρως από το 2004, με σκοπό να ερευνήσει τις ακτίνες γ που φτάνουν στη Γη από κοσμικές πηγές με ενέργειες που κυμαίνονται από 30 GeV έως 30 TeV. Το σύνολο των τηλεσκοπίων H.E.S.S. χωρίζεται σε δύο φάσεις: Η Φάση I αποτελείται από τέσσερα τηλεσκόπια 12 μέτρων (CT1-4), από τα οποία το πρώτο άρχισε να λειτουργεί το 2002, ενώ τα υπόλοιπα τρία ήταν πλήρως λειτουργικά το 2004. Η Φάση II εισήγαγε ένα μεγαλύτερο πέμπτο τηλεσκόπιο 28 μέτρων (CT5) το 2012, με στόχο την αύξηση της ευαισθησίας στο χαμηλότερο εύρος ενεργειών[6].

Οι κάμερες των τηλεσκοπίων H.E.S.S. I αποτελούνται από 960 PMTs που λειτουργούν ως pixel, οργανωμένα σε 60 μονάδες, που ονομάζονται "συρτάρια" (drawers), με 16 PMTs καθένα, και περιλαμβάνουν την ηλεκτρονικά κυκλώματα που είναι υπεύθυνα για την ενίσχυση, την ψηφιοποίηση και τη σύγκριση των σημάτων. Κάθε κάμερα ενεργοποιείται με τη σύμπτωση ενός καθορισμένου αριθμού pixel σε επικαλυπτόμενους τομείς της κάμερας, ενώ εάν περισσότερες από μία κάμερες έχουν ενεργοποιηθεί για ένα γεγονός, τα σήματα των αντίστοιχων τηλεσκοπίων αποθηκεύονται, προκειμένου να ανακατασκευαστεί στερεοσκοπικά η εικόνα Cherenkov.

Επιπλέον, η κάμερα του H.E.S.S. II σχεδιάστηκε με τις ίδιες αρχές όπως οι κάμερες του H.E.S.S. I. Ωστόσο, είναι πολύ μεγαλύτερη, περιλαμβάνοντας 2048 PMTs που είναι οργανωμένα σε 128 συρτάρια. Αυτό, μαζί με το μεγαλύτερο εστιακό μήκος, αντιστοιχεί σε πολύ υψηλότερη ανάλυση σε σύγκριση με τις κάμερες των μικρότερων τηλεσκοπίων, επιτρέποντας την ανίχνευση ατμοσφαιρικών βροχών χαμηλότερων ενεργειών. Η κάμερα αυτή διαθέτει επίσης πολύ υψηλότερο ρυθμό καταγραφής εικόνων, 10 φορές υψηλότερο από αυτόν των μικρότερων τηλεσκοπίων.

Οι κάμερες και των πέντε τηλεσκοπίων έχουν υποβληθεί σε αναβαθμίσεις, κατά τις οποίες χρησιμοποιήθηκαν νεότερα ηλεκτρονικά που αναπτύχθηκαν για το παρατηρητήριο της επόμενης γενιάς, το CTA (Cherenkov Telescope Array)[7], προκειμένου να αξιολογηθεί η απόδοσή τους.

Οι κάμερες των τηλεσκοπίων H.E.S.S. I υποβλήθηκαν σε αναβάθμιση (HESS-IU) το 2015. Ο βασικός στόχος αυτής της αναβάθμισης ήταν να μειώσει το κατώτατο όριο ενέργειας των CT1-4, ώστε να μπορούν να καταγράψουν περισσότερα γεγονότα μαζί με το CT5. Το πιο σημαντικό μέρος της αναβάθμισης ήταν η χρήση του NeCTAr (New electronics for the Cherenkov Telescope Array) readout chip, που λειτουργεί ως κυκλική αναλογική μνήμη που μπορεί να αποθηκεύσει τα σήματα εισόδου από τους PMTs με συχνότητα δειγματοληψίας 1 ns και έχει αρκετά μικρό χρόνο ανάγνωσης.

Η κάμερα HESS-IU

Τα μόνα εξαρτήματα που διατηρήθηκαν στις νέες κάμερες σε σχέση με τις προηγούμενες κάμερες του H.E.S.S. I ήταν οι φωτοπολλαπλασιαστές και οι βάσεις τους που παράγουν την υψηλή τάση. Η πλειονότητα της ανάπτυξης, παραγωγής και δοκιμής των καμερών πραγματοποιήθηκε στο site του DESY στο Zeuthen[8].

Το μπροστινό μέρος της κάμερας, όπου ανιχνεύεται και ψηφιοποιείται το φως Cherenkov από τις σωματιδιακές βροχές, αποτελείται από 960 PMTs. Αυτά οργανώνονται σε 60 "συρτάρια". Κάθε συρτάρι αποτελείται από 16 PMT, δύο αναλογικές πλακέτες (analogue boards) με 8 κανάλια η καθεμία και μια πλακέτα αργού ελέγχου (slow control board). Οι αναλογικές πλακέτες περιλαμβάνουν τα ολοκληρωμένα κυκλώματα που είναι υπεύθυνα για την ενίσχυση, τη σύγκριση και την ψηφιοποίηση των σημάτων των PMT. Η πλακέτα αργού ελέγχου, από την άλλη, περιλαμβάνει ένα FPGA (Altera Cyclone IV) που ελέγχει ολόκληρο το συρτάρι, έναν μονοπύρηνου υπολογιστή ARM9 (TaskIt Stamp9G45), ρυθμιστές ισχύος και υποδοχές για τις βάσεις υψηλής τάσης των PMT. Το μπροστινό μέρος της κάμερας χωρίζεται από το πίσω μέρος με μηχανική δομή που υποστηρίζει τα παραπάνω συρτάρια. Η πλακέτα συνδέσεων (connection board) στο πίσω μέρος αυτής της δομής φιλοξενεί υποδοχές δικτύου, ενεργοποίησης και τροφοδοσίας.

Το αναλογικό σήμα που ανιχνεύεται από τα PMT στέλνεται στις αναλογικές πλακέτες σε μορφή σύντομων παλμών αρνητικής πολικότητας. Το πλάτος τους κυμαίνεται στο εύρος $1mV - \sim 1V$, ανάλογα με τον αριθμό των ανιχνευμένων φωτονίων. Αφού φτάσουν στην πλακέτα προ-ενισχύονται κατά 9,8 χωρίζονται σε τρεις κλάδους και ενισχύονται από διαφορετικούς ενισχυτές χαμηλού θορύβου, όπου αντιστρέφεται και η πολικότητά τους.

Στη συνέχεια, το NECTAr chip λαμβάνει δύο από τους τρεις κλάδους για δειγματοληψία και ψηφιοποίηση, με παράγοντες ενίσχυσης για δύο κανάλια, υψηλής ενίσχυσης (high gain, HG) και χαμηλής ενίσχυσης (low gain, LG), που είναι ίσοι με 15,1 και 0,68 αντίστοιχα. Για να εξασφαλιστεί ότι το σήμα παραμένει εντός του εύρους εισόδου, προστίθεται μια σταθερή αντιστάθμιση βάσης περίπου 0,2 V (~ 420 ADC counts).

Ταυτόχρονα, στον τρίτο κλάδο, το σήμα ενισχύεται κατά παράγοντα 45 και δρομολογείται σε έναν υψηλής ταχύτητας συγκριτή. Το ψηφιακό σήμα εξόδου του συγκριτή αποστέλλεται απευθείας στο FPGA της πλακέτας αργού ελέγχου, όπου αναφέρεται ως το επίπεδο 0 (L0) σήμα ενεργοποίησης (trigger).

Η ανάγνωση πραγματοποιείται χρησιμοποιώντας το αναλογικό επεξεργαστικό τσιπ NeCTAr. Διαθέτει ένα κανάλι για κάθε ενίσχυση (LG, HG), το οποίο φιλοξενεί μία συστοιχία πυκνωτών με 1024 κελιά που λειτουργούν ως αναλογική κυκλική μνήμη.

Το τσιπ έχει δύο λειτουργίες: κατά τη φάση εγγραφής, η τιμή του σήματος εισόδου αποθηκεύεται στον πίνακα χωρητικότητας με συχνότητα 1 GHz. Οι τιμές γράφονται κυκλικά στη μνήμη, πράγμα που σημαίνει ότι αντικαθίστανται κάθε 1024 ns. Η διαδικασία εγγραφής σταματά όταν το τσιπ NECTAr λαμβάνει ένα σήμα ενεργοποίησης, ξεκινώντας τη φάση ανάγνωσης. Κατά τη διάρκεια της διαδικασίας ανάγνωσης, οι τιμές μιας μικρής περιοχής ενδιαφέροντος (region of interest, ROI) των κελιών διαβάζονται και ψηφιοποιούνται από τον 12-bit αναλογικό σε ψηφιακό μετατροπέα (ADC) με ρυθμό δειγματοληψίας 21 Msamples/s που φιλοξενείται στο τσιπ, και το ψηφιακό σήμα που προκύπτει κατευθύνεται στο FPGA μέσω ενός σειριοποιητή. Για τις κανονικές παρατηρήσεις, η ROI αντιστοιχεί σε 16 κελιά (16 ns). Αυτές οι τιμές στη συνέχεια μεταδίδονται στον διακομιστή της κάμερας ως μια τιμή ολοκληρωμένη πάνω στη ROI ανά pixel ανά ενίσχυση.

Το σύστημα ενεργοποίησης της κάμερας ακολουθεί μια αρχιτεκτονική N-fold σε 38 επικαλυπτόμενους τομείς των 64 PMT, με το N συνήθως να ορίζεται σε 3. Αυτό σημαίνει ότι μια N-fold σύμπτωση pixel εντός ενός τομέα θα προκαλέσει την ενεργοποίηση της κάμερας. Η αρχιτεκτονική ενεργοποίησης της κάμερας υλοποιείται ως εξής: το σήμα PMT που φτάνει στην αναλογική πλακέτα υφίσταται ενίσχυση και σύγκριση με ένα κατώφλι P (αυτήν τη στιγμή αντιστοιχεί περίπου σε 5,5 p.e.) για τη δημιουργία του σήματος L0. Το FPGA μαζί με το κουτί διεπιφάνειας του συρταριού (drawer interface box, DIB) υπολογίζουν τον αριθμό ενεργών L0 ανά τομέα. Το συνολικό σήμα κάθε τομέα αποστέλλεται στο FPGA του συρταριού, όπου συγκρίνεται με ένα κατώφλι Q, το οποίο αντιστοιχεί σε έναν αριθμό N ενεργών pixel. Οι έξοδοι του συγκριτή κατευθύνονται στο FPGA του DIB, το οποίο τις συνδυάζει με μια λογική OR πράξη, παράγοντας το σήμα ενεργοποίησης επιπέδου 1, L1. Κάθε φορά που υπάρχει ενεργό σήμα L1, το DIB μεταδίδει ένα μήνυμα "stop" σε όλα τα συρτάρια το οποίο οδηγεί στην παύση της φάσης εγγραφής του τσιπ NECTAr. Αν περισσότερα από 2 τηλεσκόπια έχουν ενεργό L1 μέσα σε ένα συγκεκριμένο χρονικό διάστημα, τότε το κεντρικό σύστημα ενεργοποίησης (central array trigger) στέλνει σήμα στα τηλεσκόπια ώστε να αρχίσουν να στέλνουν πληροφορίες οι οποίες θα καταγραφούν από τον κεντρικό υπολογιστή.

Βελτιώσεις στη βαθμονόμηση της κάμερας HESS-IU

Σε αυτή την ενότητα θα εισαγάγουμε δύο νέες μεθόδους που μπορούν να εφαρμοστούν για τη βελτίωση της βαθμονόμησης της κάμερας HESS-IU: η πρώτη αφορά την προσαρμογή του παραθύρου ανάγνωσης (readout window) στον χρόνο και η δεύτερη τον καθορισμό του παράγοντα μετατροπής ανάμεσα σε ADC counts και φωτοηλεκτρόνια ανά pixel.

Flat Field calibration και προσαρμογή του readout window

Flat Field calibration

Μία από τις κύριες μεθόδους βαθμονόμησης της κάμερας HESS-IU είναι η βαθμονόμηση Flat Field. Δεδομένου ότι το υλικό δεν είναι ιδανικό και η απόδοσή του αλλάζει αργά με τον χρόνο, διαφορετικά pixel μπορεί να έχουν

διαφορετικές αποκρίσεις σε ομοιόμορφο φωτισμό[9]. Για να διορθωθεί αυτό, ορίζεται ένας διαφορετικός συντελεστής FF για κάθε pixel. Το πλάτος κάθε σήματος που ανιχνεύεται από ένα πίξελ υπολογίζεται στη συνέχεια πολλαπλασιάζοντάς το με τον συντελεστή FF, έτσι ώστε να υπολογίζεται η τιμή του σε φωτοηλεκτρόνια. Μια άλλη διαφορά στην απόκριση στον ομοιόμορφο φωτισμό μπορεί να σχετίζεται με το χρονισμό του παραθύρου ανάγνωσης, καθώς μερικά pixel μπορεί να καταγράφουν έναν παλμό φωτός αργότερα στο παράθυρο ανάγνωσης σε σχέση με άλλα.

Περίπου κάθε δύο ημέρες πραγματοποιούνται συγκεκριμένα FF runs, κατά τη διάρκεια των οποίων, χρησιμοποιείται μία συσκευή που ονομάζεται flat-fielding unit και βρίσκεται στο κέντρο του καθρέφτη του τηλεσκοπίου, σε απόσταση 15 μέτρων από την κάμερα. Τα ειδικά FF runs χρησιμοποιούν LED φακούς που εκπέμπουν σύντομους (<3 ns FWHM - full width at half maximum) μπλε (390-420 nm) παλμούς φωτός σταθερής έντασης (περίπου 100 φωτοηλεκτρόνια)[10]. Η διαδικασία επαναλαμβάνεται πολλές φορές κατά τη διάρκεια λίγων λεπτών, προκειμένου να υπάρξει μια ακριβής κατανομή των εισερχομένων φωτονίων στην κάμερα για κάθε στιγμή κατά τη διάρκεια ενός παλμού, καθώς τα εντοπισμένα φωτόνια μπορεί να προέρχονται είτε από τη μονάδα FF είτε από τον θόρυβο του νυχτερινού ουρανού (night sky background - NSB). Η χρήση ενός ολογραφικού διαχυτή μπροστά από την κάμερα, μαζί με την ασήμαντη γωνία μεταξύ της κάμερας και της μονάδας FF, διασφαλίζουν ότι ο φωτισμός είναι ομοιόμορφος, με τη μη ομοιομορφία να είναι κάτω από 5% RMS.

Εκτός από τον καθορισμό των συντελεστών FF, αυτά τα runs χρησιμοποιούνται και για την προσαρμογή του παραθύρου ανάγνωσης 16 ns κάθε pixel, ώστε η κορυφή του παλμού FF να βρίσκεται στο κέντρο του. Με αυτόν τον τρόπο, διασφαλίζεται ότι οι περισσότεροι παλμοί από φωτόνια Cherenkov, δεδομένου ότι ακολουθούν ένα παρόμοιο μοτίβο, θα αποθηκεύονται στον buffer με το μέγιστό τους στο κέντρο του παραθύρου ανάγνωσης. Είναι σημαντικό οι κορυφές των παλμών για κάθε pixel να συμπίπτουν στα καταγεγραμμένα δεδομένα, καθώς αυτό θα οδηγήσει σε πιο ακριβή ανάλυση.

Global fit vs local fit

Για τη ρύθμιση της θέσης του παραθύρου ανάγνωσης, η οποία αναμένεται να διακυμαίνεται με την πάροδο του χρόνου εφόσον το υλικό της κάμερας δεν είναι ιδανικό, είναι απαραίτητο να μετασχηματιστούν τα δεδομένα των ιστογραμμάτων των κατανομών από κάθε pixel σε έναν μόνο παλμό. Μετά το fitting των δεδομένων, αφαιρούμε την επίδραση του θορύβου. Στη συνέχεια, εντοπίζουμε τη χρονική στιγμή στην οποία συμβαίνει η ενεργοποίηση επιπέδου 0 (L0) για το ανιχνευμένο σήμα. Με τις τρέχουσες παραμέτρους υπολογισμού, αυτό συμβαίνει σε ένα κατώφλι pixel $P=5,5$ p.e., πράγμα που σημαίνει ότι μας ενδιαφέρει το σημείο όπου κάθε παλμός FF φτάνει σε αυτήν την ένταση.

Ο προηγούμενος αλγόριθμος που χρησιμοποιούνταν για το fit των κατανομών για τον εντοπισμό της κορυφής ενός παλμού FF χρησιμοποιούσε ένα σειριακό fit του θορύβου βάσης από το παράθυρο ανάγνωσης για κάθε ένα από τα 16 δείγματα με χρονική απόσταση 1 ns σε μια διαφορετική κανονική κατανομή. Έτσι, δινόταν διαφορετική θέση για τον θόρυβο, ακόμα και αν είναι πολύ πιθανό αυτή να παραμένει σταθερή κατά τη διάρκεια ενός παλμού 16 ns, καθώς είναι ένα πολύ μικρό χρονικό διάστημα για σημαντικές αλλαγές που σχετίζονται με το περιβάλλον ή το υλικό. Η χρήση διαφορετικών παραμέτρων για κάθε κατανομή θορύβου μπορεί να οδηγήσει στο να υπερεκτιμηθεί είτε ο θόρυβος είτε το χρήσιμο σήμα και να υποεκτιμηθεί το άλλο, σε δείγματα όπου οι δύο κατανομές είναι κοντά μεταξύ τους, δίνοντας biased μέση τιμή και τυπική απόκλιση των κατανομών τους. Μια πιο αξιόπιστη προσαρμογή επιτυγχάνεται χρησιμοποιώντας έναν αλγόριθμο που καθορίζει τις τιμές του θορύβου globally, για όλες τις 16 κατανομές δειγμάτων ενός FF-run ενός pixel. Επιπλέον, η προηγούμενη μέθοδος χρησιμοποιεί μια κανονική κατανομή για να περιγράψει το χρήσιμο σήμα, ακόμα κι αν δεν είναι συμμετρικό, προσθέτοντας κάποια επιπλέον προκατάληψη στα αποτελέσματα. Η local μέθοδος προσαρμογής έναντι της προτεινόμενης global μεθόδου προσαρμογής φαίνεται στα διαγράμματα στα Σχήματα 0.0.1 και 0.0.2 αντίστοιχα.

Ένα άλλο πρόβλημα είναι ότι ο αλγόριθμος απαιτούσε τις ρυθμίσεις να γίνονται χρησιμοποιώντας τον on site server (στη Ναμίμπια) και την επεξεργασία μεγάλων ROOT5 αντικειμένων, με αποτέλεσμα να απαιτούνται περισσότερα από 10 λεπτά για να υπολογιστούν όλοι οι απαραίτητοι παράγοντες για τη ρύθμιση του παραθύρου ανάγνωσης. Ένα χρήσιμο εργαλείο για την αντιμετώπιση αυτής της πρόκλησης είναι η υποδομή Grid του DESY[11], η οποία προσφέρει μία υποδομή με περίπου 400 υπολογιστές, επιτρέποντας την παράλληλη εκτέλεση του fitting των δεδομένων για διαφορετικές κατανομές.

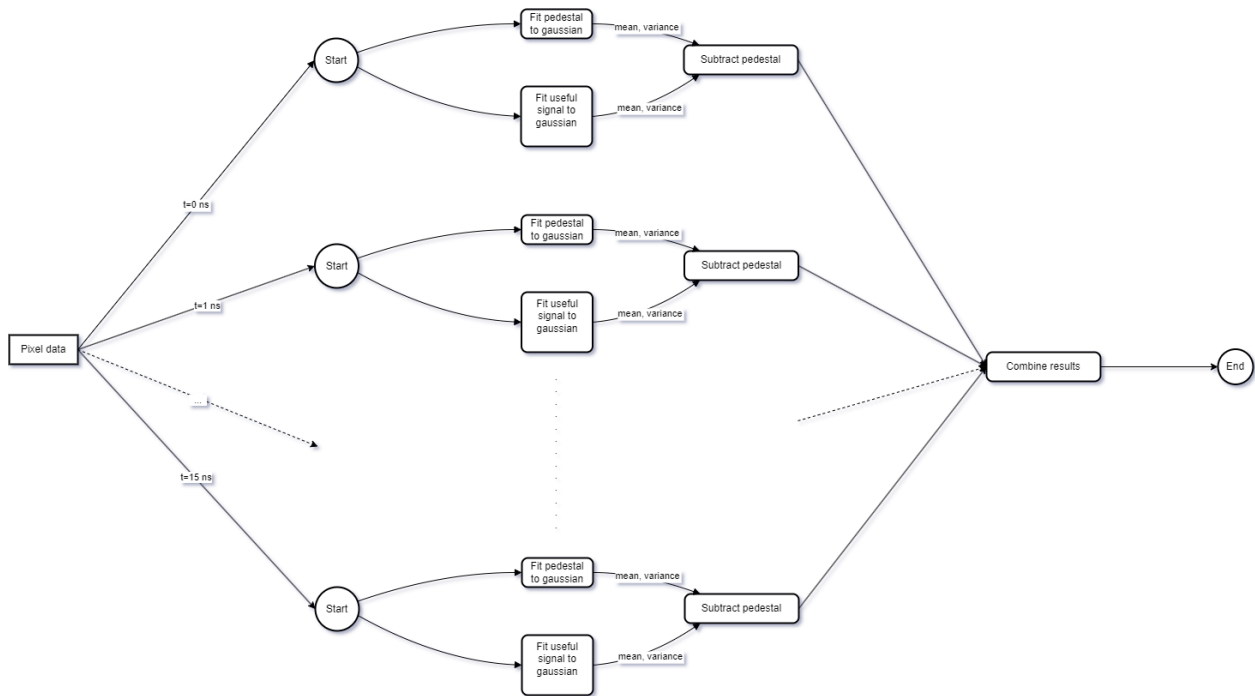


Figure 0.0.1: Local fitting scheme: κάθε δείγμα γίνεται fitted ξεχωριστά, με διαφορετική κατανομή θορύβου, η οποία αφαιρείται από κάθε δείγμα.

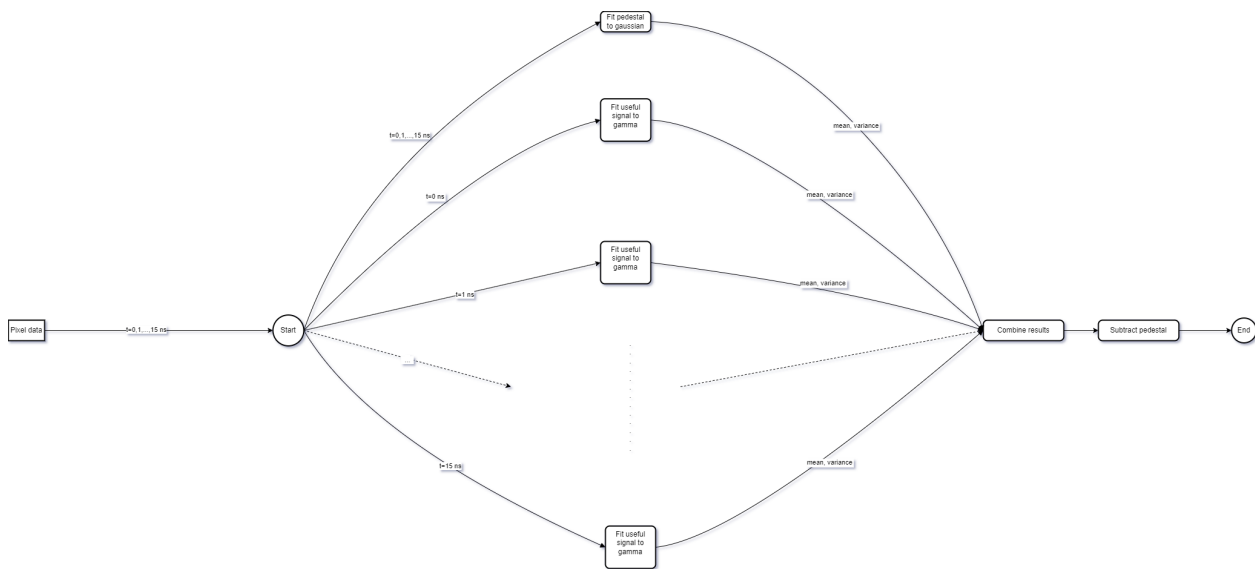


Figure 0.0.2: Global fitting scheme: μία κατανομή θορύβου περιγράφει ταυτόχρονα και τα 16 δείγματα, με ξεχωριστές κατανομές γάμμα για το χρήσιμο σήμα, σε αντίθεση με τον προηγούμενο αλγόριθμο. Ο ίδιος θόρυβος αφαιρείται από όλα τα δείγματα.

Ρύθμιση του παραθύρου ανάγνωσης λαμβάνοντας υπόψη την ένταση του LED

Καθώς η ενεργοποίηση (trigger) γίνεται όταν το σήμα φτάσει στα 5,5 p.e., η κάμερα είναι βαθμονομημένη υπέρ σημάτων μεγαλύτερου πλάτους, καθώς οι πληροφορίες που αποθηκεύονται στον προσωρινό αποθηκευτικό χώρο θα ξεκινήσουν μετά την ενεργοποίηση. Αυτό σημαίνει ότι εάν το σήμα που προκάλεσε την ενεργοποίηση δεν αυξηθεί πέρα από τα 5,5 p.e., είτε δεν θα καταγραφεί καθόλου είτε θα καταγραφεί μόνο η φθίνουσα ακμή του (αν η κορυφή είναι ίση με 5,5 p.e.), πιθανώς χάνοντας σημαντική πληροφορία. Ωστόσο, με την προσθήκη του CT5, που έχει χαμηλότερο κατώφλι ανίχνευσης, το H.E.S.S. προσπαθεί να μειώσει γενικά το κατώφλι του συστήματος, έτσι ώστε να είναι δυνατή και η ανίχνευση και η στερεοσκοπική ανακατασκευή χαμηλότερης ενέργειας φωτός Cherenkov. Αυτό το πρόβλημα μπορεί να αντιμετωπιστεί με τη ρύθμιση του παραθύρου ανάγνωσης 16 ns, ώστε το κέντρο του να βρίσκεται στη στιγμή της ενεργοποίησης, κθιστώντας πιο πιθανή τη σωστή ανίχνευση αδύναμων παλμών.

To ROOT format

Τα αρχικά δεδομένα από τις διαδικασίες βαθμονόμησης της HESS-IU αποθηκεύονται σε μορφή ROOT5. Το ROOT είναι ένα framework ανάλυσης δεδομένων που αναπτύχθηκε από το CERN [12] και είναι γραμμένο σε C++, ενώ χρησιμοποιείται για αναλύσεις και προσομοιώσεις σε διάφορα πειράματα σωματιδιακής φυσικής. Ωστόσο, η υπερπολυπλοκότητά του, με την υπερβολική ανάγκη για global μεταβλητές και περίπλοκη ιεραρχία κλάσεων, προκαλεί ορισμένους περιορισμούς στον χειρισμό των δεδομένων σε σύγκριση με την Python. Αυτός είναι ο λόγος για τον οποίο η παρακάτω ανάλυση γίνεται χρησιμοποιώντας την Python.

Ειδικά για τις FF διαδικασίες, τα δεδομένα προέρχονται σε τρισδιάστατα ιστογράμματα κατανομής του πλάτους (σε μονάδες ADC) των παλμών τάσης που παράγονται από τα PMTs για κάθε pixel, για 16 δείγματα, με απόσταση $\tau = 1\text{ns}$ μεταξύ τους. Χρησιμοποιείται μόνο το High Gain (HG) κανάλι. Η προβολή των ιστογραμμάτων σε δύο διαστάσεις παράγει ένα ιστόγραμμα για κάθε δείγμα, όπως φαίνεται στο Σχήμα 0.0.3. Σε αυτό το σχήμα μπορεί κανείς επίσης να διακρίνει τον θόρυβο βάνου (pedestal), που προκαλεί την οριζόντια γραμμή, και το χρήσιμο σήμα σε μορφή παλμού. Το pedestal παραμένει στο ίδιο σημείο καθώς περνά ο χρόνος, ενώ η ένταση και η διακύμανση του χρήσιμου σήματος αλλάζει. Για να χειριστούμε τα δεδομένα πιο εύκολα σε Python, σε αυτήν την ανάλυση τα αρχικά αρχεία .root μετατρέπονται σε αρχεία .hpy, χρησιμοποιώντας τη διεπαφή PyROOT [13].

Κάνοντας ένα global fit στα δεδομένα

Στην αρχική μορφή, καθώς και στα μεμονωμένα ιστογράμματα κάθε δείγματος, υπάρχει ένα εμφανές pedestal με μέση τιμή περίπου 415 μονάδες ADC, που προκαλείται από ηλεκτρονικό θόρυβο, ενώ το πλάτος του εξαρτάται από το φόντο του νυχτερινού ουρανού (NSB). Τα υπόλοιπα δεδομένα αποτελούν το χρήσιμο σήμα, από το οποίο προκύπτουν οι παράμετροι βαθμονόμησης.

Για να γίνει το fit των δεδομένων παράλληλα, για κάθε pixel υποθέτουμε ότι το pedestal ακολουθεί μια κανονική κατανομή με σταθερό πλάτος A , μέση τιμή μ και τυπική απόκλιση σ για κάθε ένα από τα 16 δείγματα:

$$g_1(x) = A \frac{1}{\sigma\sqrt{2\pi}} e^{-\frac{1}{2}\left(\frac{x-\mu}{\sigma}\right)^2} \quad (0.0.1)$$

Από την άλλη, δεδομένου ότι το χρήσιμο σήμα δεν είναι απαραίτητα συμμετρικό και μπορεί να "γέρνει", θεωρείται ότι το σήμα ακολουθεί μια κατανομή Γάμμα με διαφορετικές παραμέτρους C , α και β , καθώς και μια απόκλιση l για κάθε δείγμα του ίδιου pixel:

$$g_2^{(i)}(x) = C_i \frac{(x-l_i)^{\alpha_i-1} e^{-\beta_i(x-l_i)} \beta_i^{\alpha_i}}{\Gamma(\alpha_i)}, \quad i = 1, \dots, 16 \quad (0.0.2)$$

όπου $\Gamma(x)$ είναι η συνάρτηση Γάμμα, ορισμένη ως:

$$\Gamma(x) = \int_0^{\infty} s^{x-1} e^{-s} ds \quad (0.0.3)$$

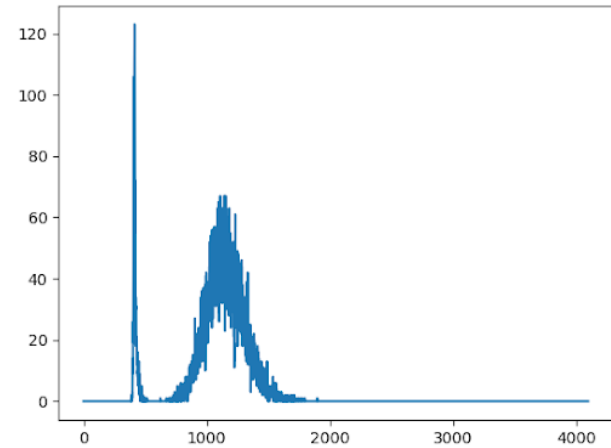
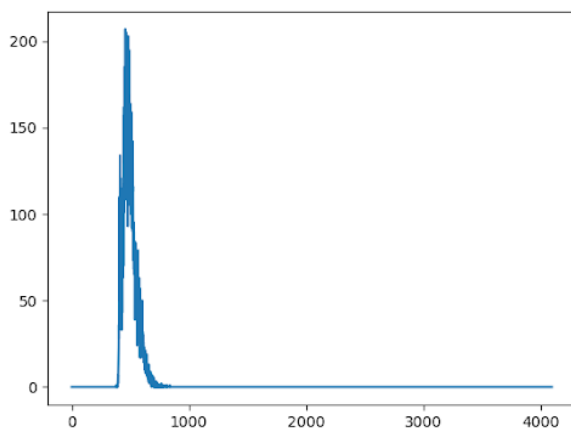
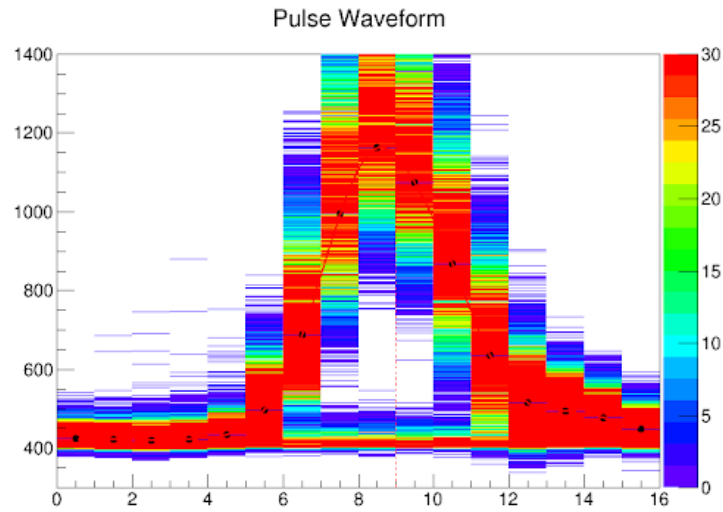


Figure 0.0.3: ROOT5 ιστογράμματα για ένα pixel. Πάνω: Αρχικό ROOT5 format. Ο οριζόντιος άξονας αντιπροσωπεύει τον χρόνο, δίνοντας τον αριθμό κάθε δείγματος του 1 ns, ενώ ο κάθετος άξονας αντιπροσωπεύει πλάτος σε ADC counts. Τα ADC counts για κάθε δείγμα δίνονται ως ιστογράμματα. Κάτω: Προβολή των ιστογραμμάτων για τα δείγματα στα 6 και 10 ns, με το καθένα να αντιστοιχεί σε μία κάθετη λωρίδα του πάνω σχήματος.

Η τελική κατανομή είναι το αποτέλεσμα της υπέρθεσης των παραπάνω δύο κατανομών:

$$G_i(x) = g_1(x) + g_2^{(i)}(x), \quad i = 1, \dots, 16 \quad (0.0.4)$$

Ορίζοντας αυτές τις συναρτήσεις για έναν παλμό για ένα pixel δημιουργούμε 67 άγνωστες μεταβλητές που πρέπει να προβλεφθούν. Από αυτές, 3 είναι κοινές σε όλα τα 16 ιστογράμματα και εξαρτώνται από τις άλλες. Αυτό είναι απαραίτητο για να διασφαλιστεί ότι το pedestal θα είναι το ίδιο για όλα τα δείγματα.

Ο αλγόριθμος περιλαμβάνει τα εξής βήματα για κάθε pixel:

1. Προεπεξεργασία κάθε δείγματος ξεχωριστά για τον εντοπισμό των αρχικών παραμέτρων.
2. Fit της μοναδικής κανονικής κατανομής για το βάθρο μαζί με τις κατανομές Γάμμα για όλα τα ατομικά δείγματα.
3. Υπολογισμός της μέσης τιμής κάθε κατανομής Γάμμα και αφαίρεση του pedestal.
4. Fit των παραπάνω τιμών για την αναπαράσταση ενός μοναδικού παλμού.
5. Υπολογισμός μετατόπισης για το παράθυρο ανάγνωσης.

Κάθε δείγμα υποβάλλεται σε προεπεξεργασία για τον καθορισμό αρχικών παραμέτρων, διότι διαφορετικά η διαδικασία θα ήταν υπερβολικά χρονοβόρα. Στη συνέχεια, κάνουμε fit κάθε ιστογράμματος με τη μέθοδο των ελαχίστων τετραγώνων, που μεταβάλλει τις παραμέτρους κατανομής μέχρι να ελαχιστοποιηθεί το τετραγωνικό άθροισμα των σφαλμάτων για όλα τα σημεία ή να επιτευχθεί ο μέγιστος αριθμός επαναλήψεων, παράγοντας την παραπάνω συνάρτηση που είναι ένα άθροισμα μιας κανονικής και μιας κατανομής Γάμμα, όπως φαίνεται στο Σχήμα 0.0.4.

Το σημαντικό κομμάτι της παραγόμενης συνάρτησης είναι η μέση τιμή και το σφάλμα της κατανομής Γάμμα για κάθε δείγμα, καθώς αυτά θα χρησιμοποιηθούν στη συνέχεια για τη μοντελοποίηση του τελικού σχήματος παλμού. Η μέση τιμή της κατανομής Γάμμα ορίζεται ως:

$$\mu_i = \frac{\alpha_i}{\beta_i} - l_i, \quad i = 1, \dots, 16 \quad (0.0.5)$$

Αφαιρώντας το pedestal και χρησιμοποιώντας τις μέσες τιμές και τα σφάλματα της χρήσιμης από κάθε δείγμα, καθορίζεται η μορφή του σήματος. Ο τελικός παλμός μοντελοποιείται εμπειρικά από την παρακάτω αναλυτική συνάρτηση:

$$f(t) = ct^q e^{-bt} \quad (0.0.6)$$

όπου c , b , q είναι οι σταθερές που πρέπει να προβλεφθούν. Αυτό γίνεται ξανά με τη βοήθεια της μεθόδου των ελαχίστων τετραγώνων.

Η επιτυχία του fit είναι εμφανής στο Σχήμα 0.0.5, όπου οι ανακατασκευασμένοι παλμοί τοποθετούνται πάνω στα αρχικά δεδομένα του ROOT (η μέση τιμή του θορύβου προστίθεται στους παλμούς για σύγκριση).

Με τις προηγούμενες παραμέτρους βαθμονόμησης, η ενεργοποίηση γίνεται στα 5,5 p.e., συχνά πριν το σήμα φτάσει στην ακμή του και το κέντρο του παραθύρου ανάγνωσης δεν βρίσκεται στην κορυφή του σήματος, καθώς βλέπουμε ότι βρίσκεται γύρω στα 7 ns. Στο Σχήμα 0.0.6 φαίνεται η προτεινόμενη μετατόπιση στο παράθυρο ανάγνωσης, δηλαδή η διαφορά μεταξύ των δύο χρονοσφραγίδων (στα 7 ns και στη στιγμή εμφάνισης της ενεργοποίησης).

Αποτελέσματα

Το Σχήμα 0.0.7 δείχνει τα ιστογράμματα της προτεινόμενης μετατόπισης στη θέση του παραθύρου ανάγνωσης για όλα τα pixel για τα CT1-4. Αυτά εφαρμόστηκαν πειραματικά στο τηλεσκόπιο, με αποτέλεσμα καλύτερη χρονική ομοιομορφία μεταξύ των τηλεσκοπίων στα δεδομένα, καθώς μετά την προσαρμογή υπήρχε παρόμοιος μέσος χρόνος pixel για όλα τα τηλεσκόπια. Είναι φανερό ότι το CT3 χρειάζεται μεγαλύτερες προσαρμογές από τα άλλα τρία τηλεσκόπια, καθώς επηρεάστηκε περισσότερο από τις προηγούμενες παραμέτρους βαθμονόμησης

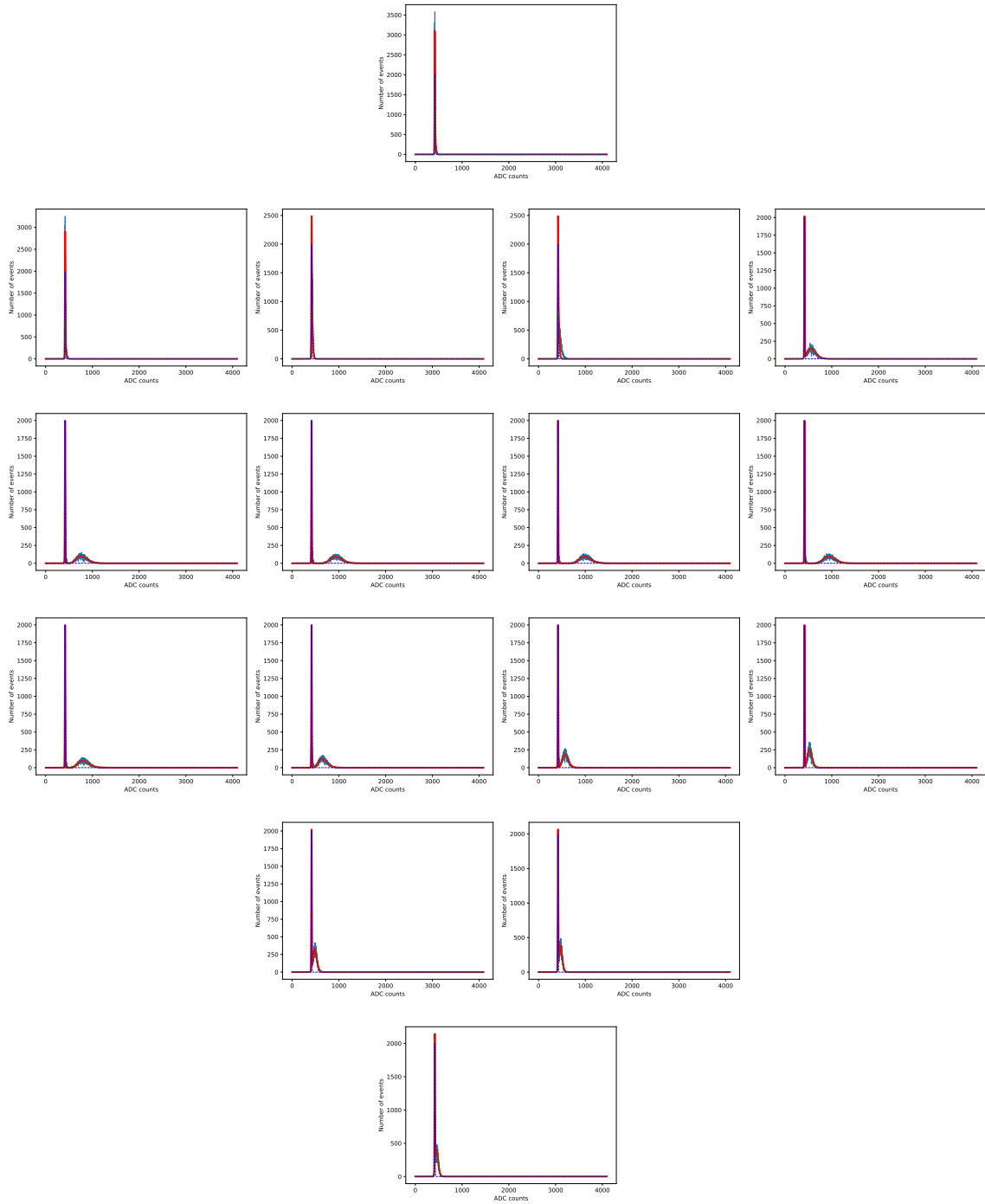


Figure 0.0.4: Ακολουθία δειγμάτων fitted με το άθροισμα μία κανονικής (pedestal) και μιας γάμμα κατανομής (χρήσιμο σήμα). Το αρχικό σήμα φαίνεται με τη μπλε συνεχή γραμμή, η κανονική και οι γάμμα κατανομές φαίνονται με διακεκομμένη μπλε και πράσινη γραμμή αντίστοιχα, ενώ η συνολική συνάρτηση μοντελοποίησης με κόκκινη συνεχή γραμμή.

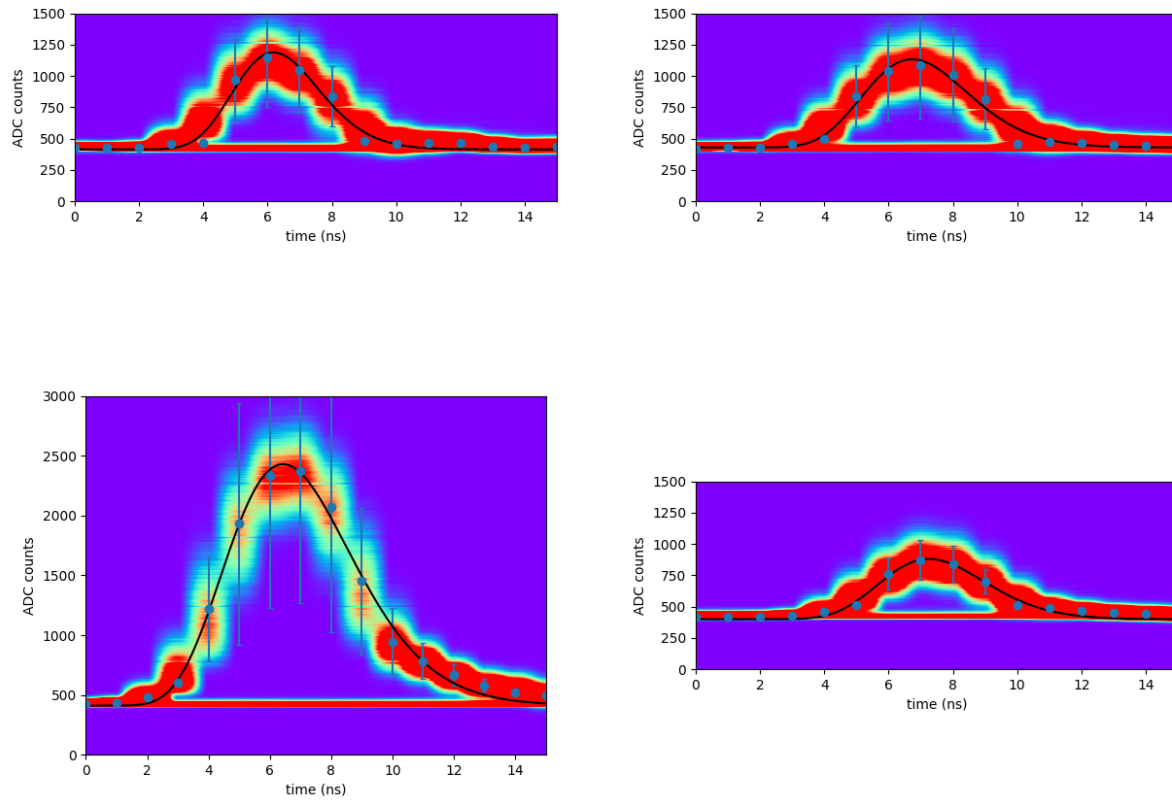


Figure 0.0.5: Ανακατασκευασμένοι παλμοί πάνω σε ιστογράμματα τύπου ROOT. Πάνω αριστερά: CT1 pixel 255, Πάνω δεξιά: CT2 pixel 7, Κάτω αριστερά: CT3 pixel 684, Κάτω δεξιά: CT4 pixel 778

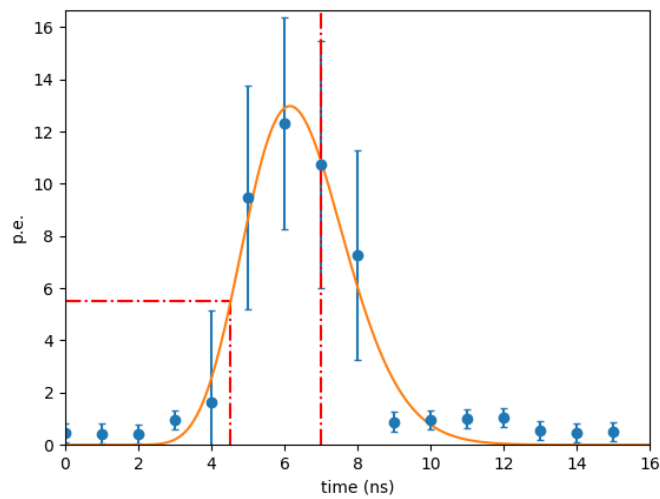


Figure 0.0.6: Παλμός για το CT1 pixel 255, με το κατώφλι των 5,5 p.e. και χρονοσφραγίδα στα 7 ns.

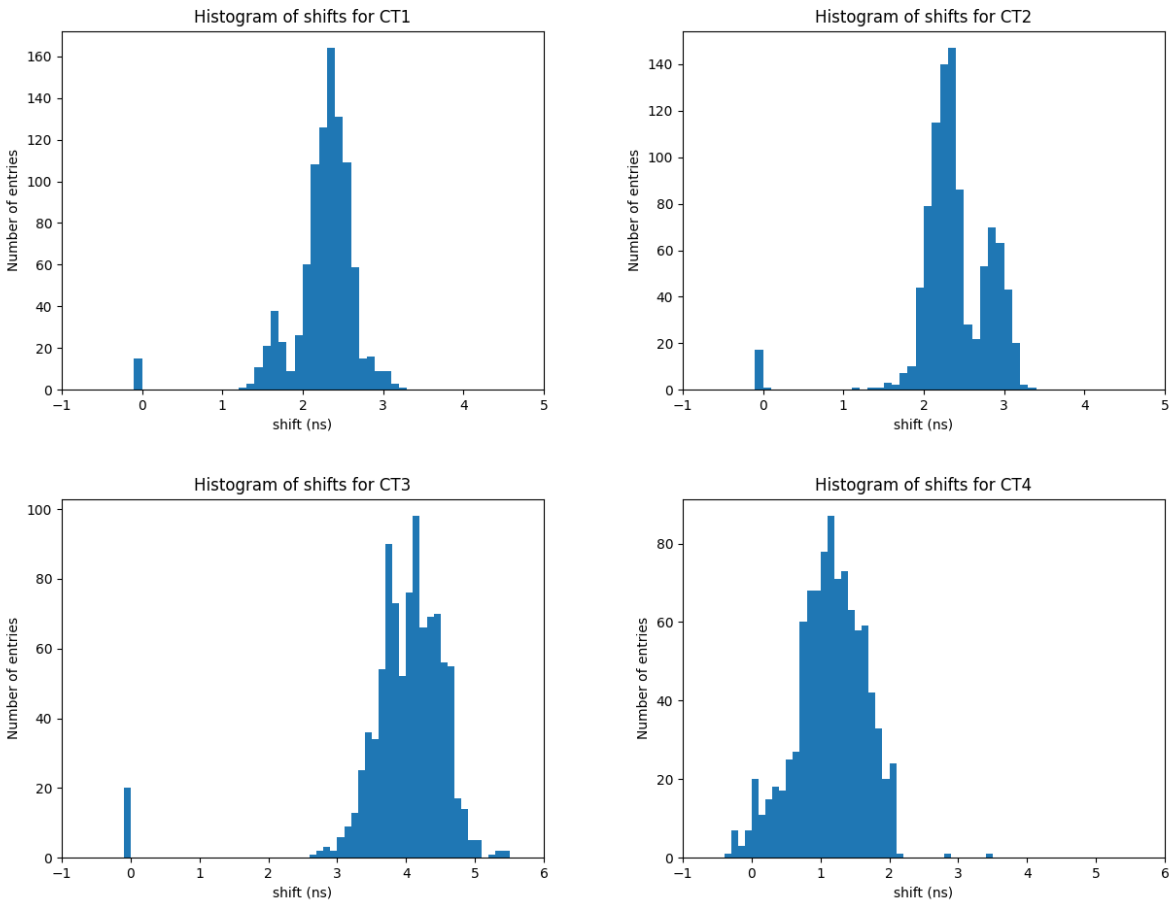


Figure 0.0.7: Ιστογράμματα προτεινόμενων μετατοπίσεων του παραθύρου ανάγνωσης.

και είχε βαθμονομηθεί υπέρ σημάτων υψηλότερης τιμής φωτοηλεκτρονίων. Οι τιμές μηδέν αντιστοιχούν σε ανενεργά pixel.

Βαθμονόμηση κέρδους μεμονωμένου φωτοηλεκτρονίου (SPE calibration) με ένα global fit

Η μέθοδος βαθμονόμησης ενός φωτοηλεκτρονίου (single photoelectron - SPE) που χρησιμοποιείται στα τηλεσκόπια H.E.S.S. περιγράφεται στο [9]. Χρησιμοποιείται για να εκτιμηθεί το κέρδος κάθε μεμονωμένου pixel. Παρόλο που η επιθυμητή τιμή για το κέρδος των PMT που χρησιμοποιείται για την ανάλυση είναι σταθερή στις 60 μονάδες ADC κατά την κανονική λειτουργία της κάμερας, το κέρδος των PMT αλλάζει στην πράξη με την πάροδο του χρόνου λόγω της γήρανσής τους και αποκλίνει από αυτήν την τιμή κάτω από τη σταθερά εφαρμοζόμενη τάση στα PMT. Έτσι, δεδομένου ότι εξαρτάται από την τάση του PMT, πρέπει να βρούμε κατά πόσο πρέπει να αλλάξει η τάση για να φτάσει στην επιθυμητή τιμή 60 μονάδων ADC. Προσαρμόζουμε τον προηγούμενο αλγόριθμο, υποθέτοντας ότι το κέρδος εξαρτάται γραμμικά από την εφαρμοζόμενη τάση και εκτελούμε ένα global fit στις παραμέτρους της γραμμικής σχέσης για όλα τα δείγματα.

Μετατροπή μονάδων ADC σε φωτοηλεκτρόνια

Όπως και με τη βαθμονόμηση FF, εκτελούνται ειδικά SPE runs μια φορά περίπου κάθε δύο ημέρες. Στη βαθμονόμηση SPE, η απόκριση σε διάφορες υψηλές τάσεις συνδυάζεται προκειμένου να προκύψει το κέρδος των PMT. Το κέρδος κάθε pixel ορίζεται ως ο παράγοντας μετατροπής από μονάδες ADC σε φορτίο (ολοκλήρωμα) σήματος. Αρχικά, η τάση εξόδου του PMT V_{PM} μετρείται σε μονάδες ADC σε έναν αντιστάτη 16 φορές, κάθε $\tau = 1$ ns, και ενισχύεται σε ένα κανάλι υψηλής και ένα κανάλι χαμηλής ενίσχυσης, με ενίσχυση G^{HG} και

G^{LG} αντίστοιχα. Τα αποτελέσματα καταγράφονται ως ψηφιακό σήμα, το οποίο ολοκληρώνεται σε διάστημα 16 ns. Προκειμένου να μετατραπούν οι μονάδες ADC σε Volt, το σήμα αυτό πολλαπλασιάζεται με τον παράγοντα $V_{ADC} = 1.22 \text{ mV/Count}$. Αν το σήμα είναι στη μορφή ενός παλμού SPE, με μορφή $V_{PM,s.p.e.}(t)$, τότε η αντιστροφή της τελευταίας πράξης δίνει το κέρδος του pixel:

$$\gamma_{e,i}^{ADC} = \frac{G^i}{\tau V_{ADC}} \int V_{PM,s.p.e.}(t) dt, \quad i = HG, LG \quad (0.0.7)$$

κόμη και όταν δεν υπάρχουν παλμοί από LED, μπορούν επίσης να μοντελοποιηθούν με μια κανονική κατανομή με ανεξάρτητη μικρότερη μέση τιμή και διακύμανση.

Βαθμονόμηση SPE

Στην αντίθεση με τα FF runs, τα SPE runs διεξάγονται με τις κάμερες στο "καταφύγιο" τους, με αποτέλεσμα να μην υπάρχει μία φαριδιά κατανομή pedestal που προκαλείται από το φως του νυχτερινού ουρανού, αλλά μόνο ένα offset από το ηλεκτρονικό pedestal σε κάθε δείγμα. Αυτά τα runs χρησιμοποιούν έναν LED pulser, που βρίσκεται δύο μέτρα μακριά από τις κάμερες. Ο pulser εκπέμπει φως το οποίο φωτίζει κάθε pixel με ένταση που αντιστοιχεί σε περίπου 1 φωτοηλεκτρόνιο, με συχνότητα 70 Hz. Τα runs είναι προγραμματισμένα με μια μικρή καθυστέρηση σε κάθε γεγονός πριν την ενεργοποίηση, έτσι ώστε ο SPE παλμός να βρίσκεται στο κέντρο του παραθύρου ανάγνωσης 16 ns. Αν και ο pulser εκπέμπει ένα φωτοηλεκτρόνιο, το pixel θα παρατηρήσει πιθανότατα περισσότερα από ένα φωτοηλεκτρόνια, λόγω δευτερεύουσας εκπομπής. Ο ακριβής υπολογισμός της κατανομής του φορτίου SPE σε ADC counts προέρχεται από το ολοκλήρωμα των αποκτηθεισών κατανομών ADC counts για όλα τα δείγματα στην περιοχή ενδιαφέροντος. Η κατανομή φορτίου που προκύπτει θα έχει με διαφορετικά μέρη που αντιστοιχούν στο ολοκλήρωμα του pedestal και σε μεμονωμένες τιμές των φωτοηλεκτρονίων που συλλέγονται από την άνοδο του PMT.

Για τον υπολογισμό της κατανομής του φορτίου SPE, γίνονται οι εξής τρεις υποθέσεις: Ο αριθμός των φωτοηλεκτρονίων ακολουθεί μια κατανομή Poisson, ο ηλεκτρονικός θόρυβος (pedestal) είναι πολύ μικρότερος σε πλάτος από την κατανομή SPE και ένα φωτοηλεκτρόνιο περιγράφεται από μια κανονική κατανομή. Η συναρτηση που προκύπτει από αυτές τις υποθέσεις είναι η εξής:

$$\begin{aligned} SPE(q) = & N \frac{e^{\langle k \rangle}}{\sqrt{2\pi}\sigma_P} \left[-\frac{(q - \mu_P)^2}{2\sigma_P^2} \right] \\ & + N_s \sum_{k=1}^{k \gg 1} \frac{e^{\langle k \rangle}}{\sqrt{2\pi k}\sigma_G} \frac{k^k}{k!} \exp \left[-\frac{(q - (\mu_P + kG))^2}{2k\sigma_G} \right] \end{aligned} \quad (0.0.8)$$

όπου μ_P, σ_P είναι η μέση τιμή και η τυπική απόκλιση της κατανομής του pedestal, G, σ_G η μέση τιμή και η τυπική απόκλιση της κατανομής του κέρδους, $\langle k \rangle$ ο μέσος όρος της έντασης του φωτός. N και N_s είναι παράγοντες κανονικοποίησης που αντιστοιχούν στον αριθμό των γεγονότων σε ένα run. Σύμφωνα με αυτήν τη συνάρτηση, η κατανομή SPE είναι μια υπέρθεση των κανονικών κατανομών, όπου η πρώτη στενότερη κατανομή αντιστοιχεί στο pedestal, η δεύτερη κατανομή αντιστοιχεί σε γεγονότα με ένα φωτοηλεκτρόνιο, η τρίτη κατανομή αντιστοιχεί σε γεγονότα με δύο φωτοηλεκτρόνια, κ.ο.κ. Η μέση τιμή της κάθε κανονικής κατανομής είναι ανάλογη με τον αριθμό των φωτοηλεκτρονίων.

Ο στόχος αυτής της ανάλυσης είναι να προσδιορίσει το κέρδος G του καναλιού υψηλής ενίσχυσης, επομένως ο δείκτης HG στο εξής εννοείται. Όπως και πριν, χρησιμοποιούνται μόνο τα δεδομένα από το κανάλι υψηλής ενίσχυσης, διότι το κέρδος στο κανάλι χαμηλής ενίσχυσης μπορεί να προσδιοριστεί πολλαπλασιάζοντας το G με τον παράγοντα μετατροπής μεταξύ των δύο καναλιών. Αυτός ο παράγοντας μπορεί να βρεθεί διαιρώντας το πλάτος του pedestal που μετρήθηκε στο χαμηλό κανάλι με αυτό που μετρήθηκε στο υψηλό κανάλι.

Για τον σκοπό της ακριβούς προσδιορισμού του κέρδους, διάφορες υψηλές τάσεις εφαρμόζονται στο PMT κατά τη διάρκεια των SPE runs, και οι προκύπτουσες κατανομές σε κάθε PMT γίνονται fitted στην παραπάνω υπέρθεση των κανονικών κατανομών. Οι άγνωστες μεταβλητές στην είναι 4 για κάθε run: μ_P, σ_P και G, σ_G . Στη συνέχεια, η τελική τιμή του κέρδους προσδιορίζεται συνδυάζοντας το αποτέλεσμα από όλα τα runs.

Εμείς θα χρησιμοποιήσουμε $max(k) = 10$, αφού για μεγαλύτερες τιμές οι κατανομές που προκύπτουν είναι σε σχέση με τα δεδομένα. Ο προηγούμενος αλγόριθμος κάνει fit κάθε run σειριακά, θεωρώντας τις μεταβλητές

κάθε run ανεξάρτητες μεταξύ τους, δίνοντας έτσι 36 άγνωστες μεταβλητές. Ωστόσο, όσο αυξάνεται η τάση, αυξάνεται και η ουρά του σήματος, υπονοώντας ότι το κέρδος του εικονοστοιχείου είναι περίπου γραμμικό ως προς την εφαρμοζόμενη τάση. Αυτό σημαίνει ότι, αν το κέρδος οριστεί ως γραμμική συνάρτηση:

$$G = \alpha dV + \beta, \quad \alpha, \beta : \text{σταθερές} \quad (0.0.9)$$

οι άγνωστες μεταβλητές μειώνονται σε μόνο 20.

Και πάλι, τα αρχικά δεδομένα SPE για κάθε pixel βρίσκονται σε μορφή ROOT5 και αποτελούνται από ιστογράμματα των ολοκληρωμένων μετρήσεων ADC για κάθε ένα από τα 9 διαφορετικά runs, κάθε ένα για μια διαφορετική υψηλή τάση dV , που ποικίλλει από -20 έως 20 V με βήμα 5V, σε σχέση με την πραγματική τάση του PMT. Ο αλγόριθμος κάνει τα ακόλουθα:

1. Κάνει ομαλοποίηση του σήματος χρησιμοποιώντας ένα φίλτρο Savitzky-Golay
2. Υπολογίζει αρχικές τιμές για το μ_P και το G λαμβάνοντας υπόψη τις δύο πρώτες κορυφές του ομαλού σήματος μ_{P0} , G_0 για $dV = 0$
3. Εκτελεί ένα global fit για την κατανομή SPE συνδυάζοντας όλα τα runs και προβλέπει τα α , β
4. Προσδιορίζει την απαιτούμενη διαφορά τάσης dV για να έχουμε $G = 60$

Τα αποτελέσματα του fit φαίνονται στα Σχήματα 0.0.8, όπου εμφανίζονται οι fitted κανονικές κατανομές του κέρδους για μερικά από τα διάφορα τρεξίματα, και 0.0.9, όπου εμφανίζεται η προκύπτουσα γραμμή κέρδους-τάσης.

Αποτελέσματα και σύγκριση με τον προηγούμενο αλγόριθμο

Τα ιστογράμματα των προτεινόμενων αλλαγών στα PMTs για τα τηλεσκόπια σε σύγκριση με τα αποτελέσματα από την προηγούμενη μέθοδο φαίνονται στο Σχήμα 0.0.10. Οι μικρές διαφορές από το αντίστοιχο cross-check βρίσκονται εντός των ορίων αβεβαιότητας. Έτσι, το global fit που υποθέτει γραμμική αύξηση του κέρδους επιταχύνει τη διαδικασία προσδιορισμού του κέρδους χρησιμοποιώντας λιγότερες παραμέτρους, ενώ παράλληλα παράγει συνεπή αποτελέσματα.

Μετατροπή από sample mode σε charge mode

Κατά τη διάρκεια των παρατηρήσεων, οι πληροφορίες που χρησιμοποιούνται για την ανακατασκευή εικόνων της εκπομπής ακτινοβολίας γάμμα από πηγές και για την εκτέλεση της ανάλυσης έχουν τη μορφή φορτίου, δηλαδή το ολοκλήρωμα σε μονάδες p.e. πάνω στα 16 δείγματα της περιοχής ενδιαφέροντος κάθε παλμού ενός PMT. Η ανάλυση του σήματος με 16 δείγματα αναφέρεται ως λειτουργία δείγματος (sample mode), ενώ η ανάλυση του τελικού ολοκληρώματος ως λειτουργία φορτίου (charge mode). Το φορτίο υπολογίζεται αρχικά σε μονάδες ADC και στη συνέχεια μετατρέπεται σε μονάδες p.e.

Είναι προφανές ότι το τελικό πλάτος που μετράμε εξαρτάται σε μεγάλο βαθμό από τη θέση του παραθύρου ανάγνωσης και μπορεί να επηρεαστεί αν το παράθυρο ανάγνωσης δεν έχει βαθμονομηθεί σωστά. Ένα παράδειγμα αυτού του προβλήματος προέκυψε μετά από πρόσφατη αντικατάσταση της πλακέτας τροφοδοσίας της κάμερας, προκαλώντας bias στα πλάτη που χρησιμοποιήθηκαν στην ανακατασκευή της εικόνας. Συγκεκριμένα, η αλλαγή του υλικού επηρέασε τη χρονική στιγμή του σήματος L0 trigger, προκαλώντας μια μετατόπιση του παραθύρου ανάγνωσης προς τα δεξιά. Το σήμα L0 trigger ενεργοποιούνταν όταν η φθίνουσα ακμή του σήματος λειτουργίας δείγματος έφτανε το κατώφλι ενεργοποίησης, πράγμα που σημαίνει ότι οι περισσότεροι καταγεγραμμένοι παλμοί αποθηκεύονταν χωρίς τμήμα της ανόδου τους. Οι παλμοί αποθηκεύονταν με αυτόν τον τρόπο για μερικές εβδομάδες, επηρεάζοντας σημαντικά τα δεδομένα που χρησιμοποιήθηκαν για την ανακατασκευή και την ανάλυση των γεγονότων. Σε αυτή την ενότητα, θα προτείνουμε έναν τρόπο για τη μερική ανάκτηση των επηρεασμένων δεδομένων. Η ανάλυση πραγματοποιείται χρησιμοποιώντας το HTCondor[14].

Ανάκτηση του φορτίου και μερικά ολοκληρώματα

Προκειμένου να μετατρέψουμε τα δεδομένα sample mode σε δεδομένα charge mode, εκμεταλλευόμαστε το γεγονός ότι τα περισσότερα σήματα έχουν παρόμοια μορφή, που προσεγγίζεται από την αναλυτική συνάρτηση από την Εξίσωση 4.2.6, και μπορούν να διαφέρουν μόνο στο πλάτος στον χρόνο, το πλάτος τους και το χρόνο

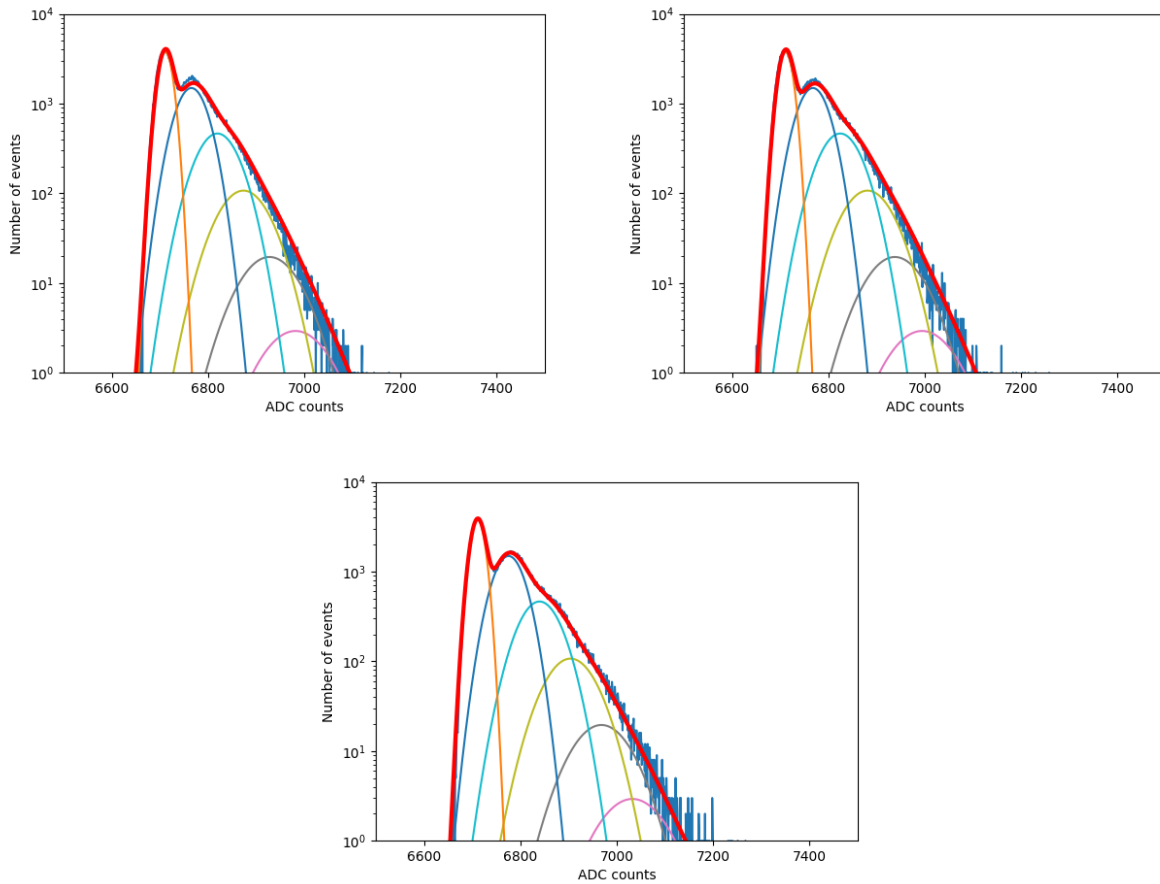


Figure 0.0.8: Global fit στο κέρδος του CT2 pixel 0, σε λογαριθμική κλίμακα. Το αρχικό σήμα φαίνεται με τη σκούρα μπλε γραμμή, ενώ οι διαφορετικές κανονικές κατανομές που αντιστοιχούν σε διαφορετικές τιμές φωτοηλεκτρονίων (p.e.) φαίνονται με διαφορετικό χρώμα η κάθε μία. Η τελική κατανομή φαίνεται με κόκκινο. Πάνω αριστερά: run 0 ($dV = -20$); Πάνω δεξιά: run 2 ($dV = -10$); Κάτω: run 8 $dV = +15$.

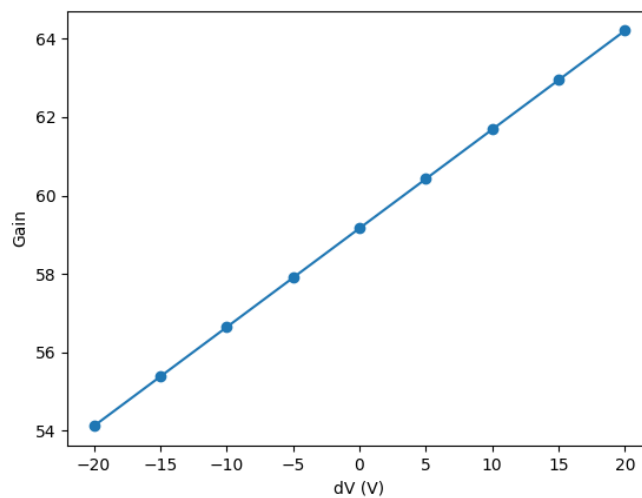


Figure 0.0.9: Ευθεία κέρδους μετά το global fit για CT2 pixel 0. Για μηδενική προσαρμογή στην τάση, το κέρδος είναι μερικά ADC counts κάτω από το 60.

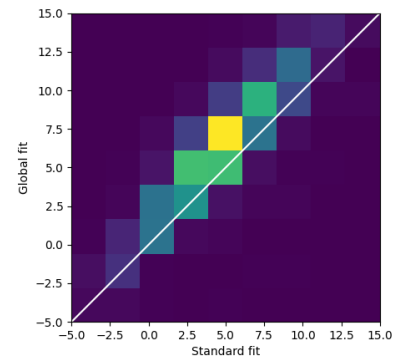
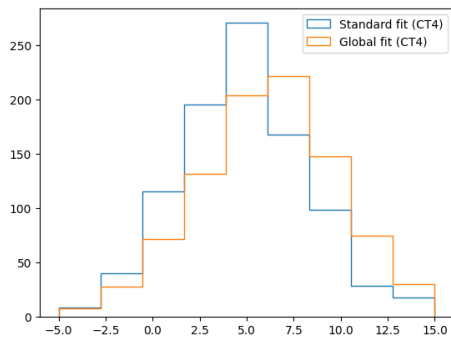
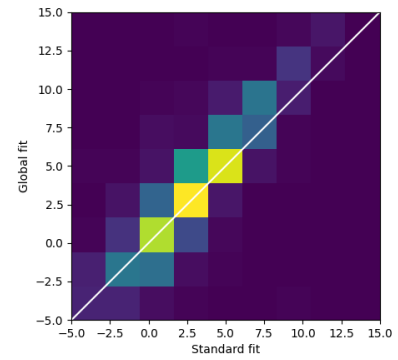
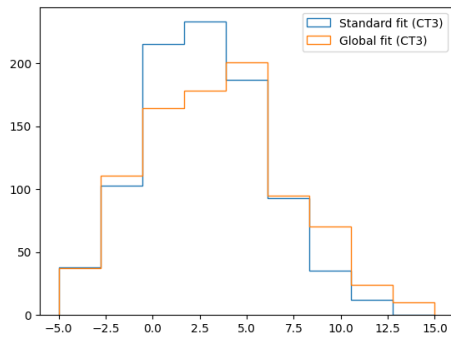
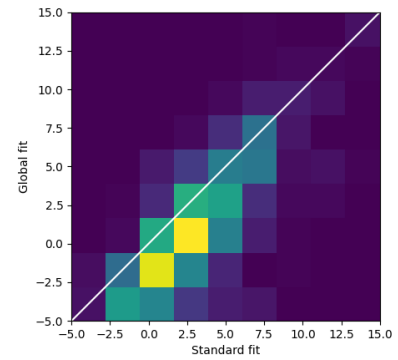
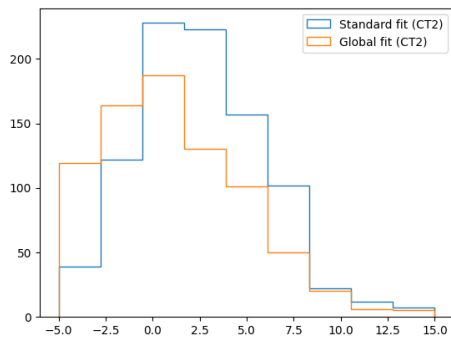
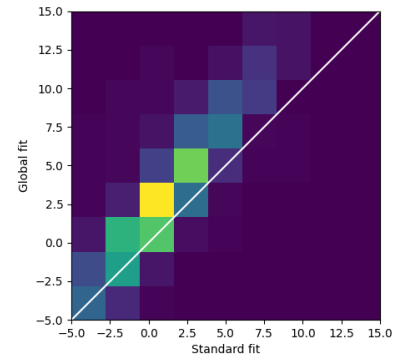
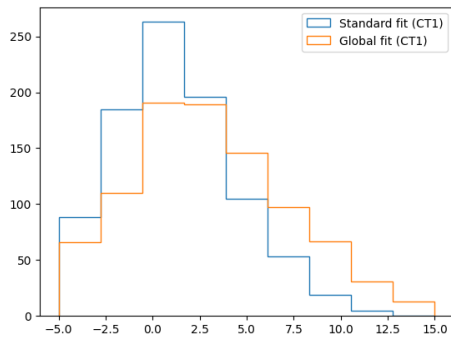


Figure 0.0.10: 1D και 2D ιστογράμματα των προτεινόμενων αλλαγών σε τάση για τα CT1-4 σύμφωνα με τον καινούργιο και τον παλιό αλγόριθμο.

της κορυφής τους. Έτσι, αν κατά τη διάρκεια του παραθύρου ανάγνωσης μας με n δείγματα έχουμε καταγράψει μια επαρκή ποσότητα του σήματος σε sample mode, που αποτελείται από τουλάχιστον m δείγματα, μπορούμε να πολλαπλασιάσουμε το ολοκλήρωμά του με έναν συντελεστή C για να ανακτήσουμε το ολοκλήρωμα του πλήρους σήματος. Στην περίπτωση μας, θεωρούμε ότι η ανάκτηση του ολοκληρώματος του σήματος 16 δειγμάτων είναι δυνατή με τουλάχιστον $m = 9$ δείγματα. Ταυτόχρονα, θεωρούμε ότι το παράθυρο ανάγνωσης έχει μετατοπιστεί για ένα συγκεκριμένο χρονικό offset λίγα ns προς τα δεξιά, όπως συνέβη με την αντικατάσταση της πλακέτας τροφοδοσίας.

Ορίζουμε τις παρακάτω ποσότητες, οι οποίες αντιστοιχούν στο φορτίο ενός σήματος γύρω από την κορυφή του σε μονάδες ADC:

$$q_9 = \int_{t_0-4.5}^{t_0+4.5} f(x) dx \quad (0.0.1)$$

$$q_{16}(t') = \int_{t_0-8}^{t_0-8+t'} f(x+t') dx \quad (0.0.2)$$

Η πρώτη ποσότητα αντιστοιχεί στο ολοκλήρωμα 9 δειγμάτων γύρω από τον χρόνο t_0 όπου βρίσκεται η κορυφή του σήματος σε ένα παράθυρο ανάγνωσης που είναι κανονικά βαθμονομημένο, ενώ η δεύτερη ποσότητα αντιστοιχεί στο ολοκλήρωμα 16 δειγμάτων όλου του σήματος γύρω από την αρχική του κορυφή όταν το σήμα μετατοπίζεται t' ns προς τα αριστερά (ή το παράθυρο ανάγνωσης μετατοπίζεται προς τα δεξιά).

Το ολοκλήρωμα 16 ns είναι το φορτίο που πρέπει να ανακτηθεί για να διεξαχθεί σωστά η ανάλυση των παρατηρήσεων. Για αυτόν τον λόγο, θα χρησιμοποιήσουμε το q_9 και θα παραμετροποιήσουμε την ανάκτηση του q_{16} .

Βαθμονόμηση και συντελεστές ανακατασκευής

Για να αντιμετωπίσουμε το πρόβλημα, χρησιμοποιούμε δεδομένα από 10 διαφορετικά runs βαθμονόμησης χρησιμοποιώντας τη μονάδα SPE και φωτίζοντας τις κάμερες HESS-IU με μεταβαλλόμενη φωτεινότητα. Στη συνέχεια, αυτά τα σήματα παραμετροποιούνται χρησιμοποιώντας την ίδια μέθοδο που περιγράψαμε για τα FF runs, με τη μοναδική διαφορά ότι δε χρειάζεται να γίνεται fit στην κατανομή της βάσης, καθώς αυτά τα runs εκτελούνται με κλειστό καπάκι της κάμερας και δεν επηρεάζονται από το φως του νυχτερινού ουρανού. Αυτό γίνεται για όλα τα pixels όλων των 4 καμερών για κάθε run. Ένα παράδειγμα ενός τέτοιου σήματος φαίνεται στο Σχήμα ??.

Δεδομένου ότι η μορφή των σημάτων βαθμονόμησης είναι παρόμοια με τη μορφή των σημάτων παρατήρησης, μπορούμε να χρησιμοποιήσουμε αυτά τα runs βαθμονόμησης για να υπολογίσουμε τους συντελεστές διόρθωσης, με τους οποίους μπορούμε να πολλαπλασιάσουμε το ολοκλήρωμα q_9 των σημάτων παρατήρησης, υποθέτοντας ότι έχουμε την προσεγγιστική του τιμή, προκειμένου να ανακτήσουμε το φορτίο. Αυτό γίνεται υπολογίζοντας το q_9 και μετατοπίζοντας το σήμα προς τα αριστερά κατά t' ns, προτού υπολογίσουμε το $q_{16}(t')$. Αυτή η διαδικασία εκτελείται για $t' = 0, \dots, 15$. Στη συνέχεια, οι συντελεστές διόρθωσης θα είναι:

$$C(t') = \frac{q_{16}(t')}{q_9} \quad (0.0.3)$$

Οι συντελεστές για όλα τα runs, τηλεσκόπια και pixels τοποθετούνται σε ένα ιστόγραμμα, για χρονική στιγμή κορυφής του σήματος (ισοδύναμο με t_0+t'). Αυτά τα ιστογράμματα παρουσιάζονται στο Σχήμα 0.0.11, για χρόνο κορυφής έως 15 ns. Αξίζει να σημειωθεί ότι οι συντελεστές είναι ανεξάρτητοι από την ένταση του φωτισμού και το πλάτος των sample mode σημάτων, όπως φαίνεται στο Σχήμα 0.0.13. Τα πρώτα δύο runs μπορούν να εξαιρεθούν για τον υπολογισμό των τελικών συντελεστών, καθώς η χαμηλή έντασή τους αντιστοιχεί σε σχεδόν μηδενικά γεγονότα και το fit είναι πιο ασταθές. Η μέση τιμή και η τυπική απόκλιση των τελικών συντελεστών, που προκύπτουν από τα ιστογράμματα του Σχήματος 0.0.11, φαίνονται στο Σχήμα 0.0.12. Η τυπική απόκλιση είναι αρκετά μικρή, καθιστώντας αυτούς τους συντελεστές αποδεκτούς. Είναι επίσης σημαντικό να σημειωθεί ότι οι συντελεστές ξεκινούν από μια τιμή ελαφρώς υψηλότερη από το 1, για ένα μικρό τμήμα από τα αριστερά του σήματος που λείπει, και πέφτουν απότομα στο 0 όσο περισσότερο μετατοπίζεται το σήμα προς τα αριστερά. Άρα για μικρή μετατόπιση του παραθύρου ανάγνωσης, το q_9 είναι περίπου ισοδύναμο με το q_{16} , ενώ για πιο μεγάλες μετατοπίσεις μπορούμε να το πολλαπλασιάσουμε με τους συντελεστές που υπολογίσαμε. Για πολύ μεγάλες μετατοπίσεις οι συντελεστές είναι 0. Τέλος, το Σχήμα 0.0.14 δείχνει τα αποτελέσματα του ελέγχου ανάμεσα

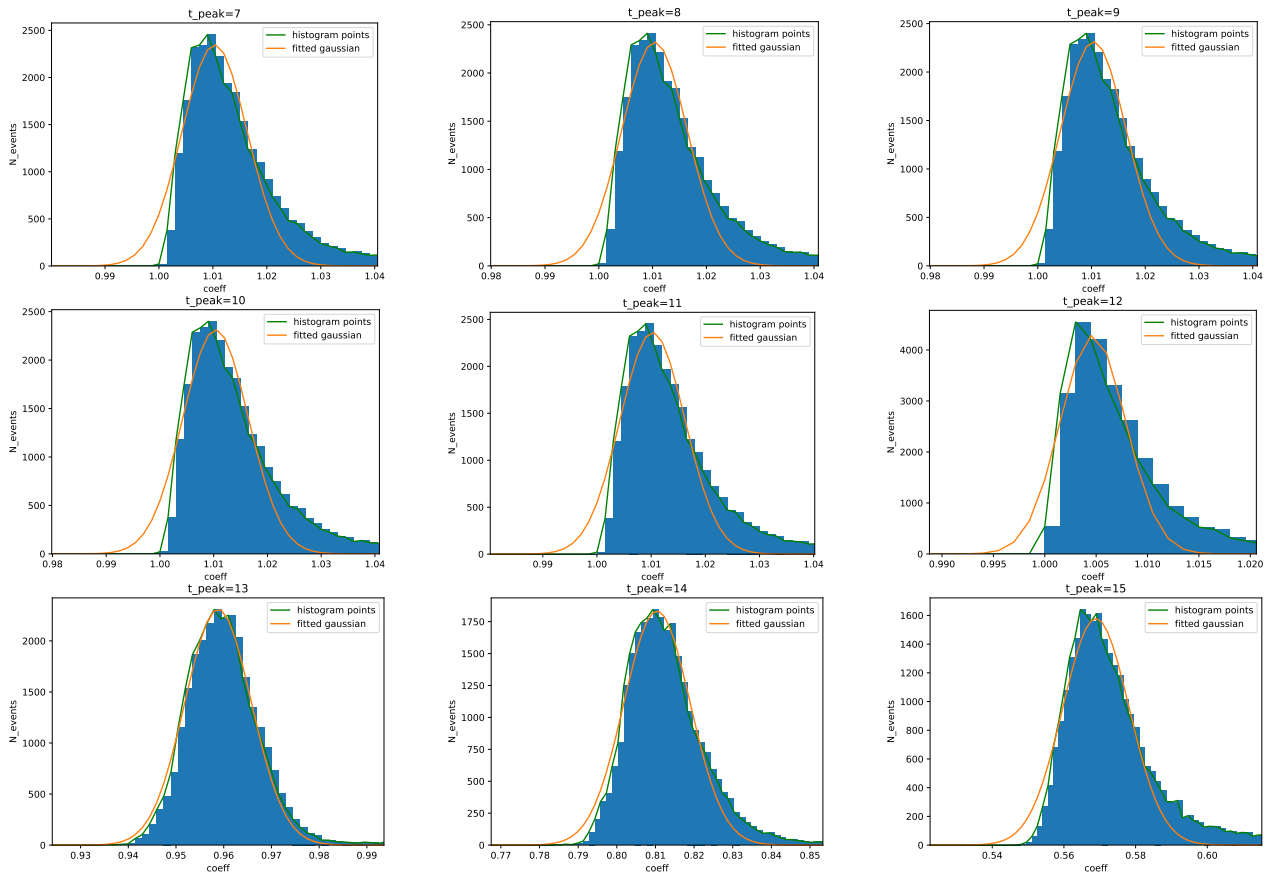


Figure 0.0.11: Ιστογράμματα των συντελεστών διόρθωσης.

στο πραγματικό q_{16} των δεδομένων βαθμονόμησης και το ανακτημένο q_{16} , που υπολογίζεται αν πολλαπλασιαστεί το q_9 με τον συντελεστή διόρθωσης. Η αβεβαιότητα είναι αρκετά χαμηλή, υποδηλώνοντας ότι το ανακτηθέν φορτίο είναι αρκετά κοντά στο πραγματικό.

Σύγκριση με δεδομένα από παρατηρήσεις

Χρησιμοποιήσαμε την παραμετροποίησή μας για να δούμε εάν μπορεί να χρησιμοποιηθεί με επιτυχία για δεδομένα από πραγματικές παρατηρήσεις, δεδομένου ότι οι συντελεστές μας υπολογίστηκαν χρησιμοποιώντας δεδομένα από calibration runs χωρίς επιρροή του νυχτερινού ουρανού. Το σύνολο δεδομένων αποτελείται από περίπου 10^9 συμβάντα από όλα τα τηλεσκόπια. Ορισμένα παραδείγματα αποτελεσμάτων φαίνονται στα Σχήματα 0.0.15, 0.0.16 και 0.0.17. Φαίνεται ότι η ανακατασκευή χρησιμοποιώντας τους συντελεστές ανάκτησής μας είναι εφικτή. Ωστόσο, εμφανίζει ένα bias με την αύξηση του χρόνου της κορυφής, διότι για μεγαλύτερη απόκλιση στη θέση του παραθύρου ανάγνωσης, το φορτίο (q_{16}) θα έπρεπε να είναι μηδέν σύμφωνα με την παραμετροποίησή μας. Βλέπουμε ότι αυτό δεν ισχύει για το σύνολο δεδομένων μας, όπου υπάρχουν υψηλές τιμές για το q_{16} καθώς ο χρόνος αυξάνεται, υπονοώντας ότι το σήμα έχει μια μακρά ουρά. Υποθέτουμε ότι αυτό συμβαίνει λόγω διαφορετικών μεθόδων αφαίρεσης του θορύβου που χρησιμοποιούνται για τη βαθμονόμηση και την παρατήρηση. Είναι πιθανό κάποιο night sky background να επιβίωσε τη διαδικασία καθαρισμού της εικόνας, ένα ζήτημα που δεν προβλεπόταν από την μέθοδό μας καθώς χρησιμοποιήθηκαν ειδικά runs με τη μονάδα SPE και κλειστό καπάκι κάμερας. Παρ' όλα αυτά, η μέθοδός μας έχει αρκετές προοπτικές, εάν λάβουμε υπόψη πραγματικές συνθήκες παρατήρησης.

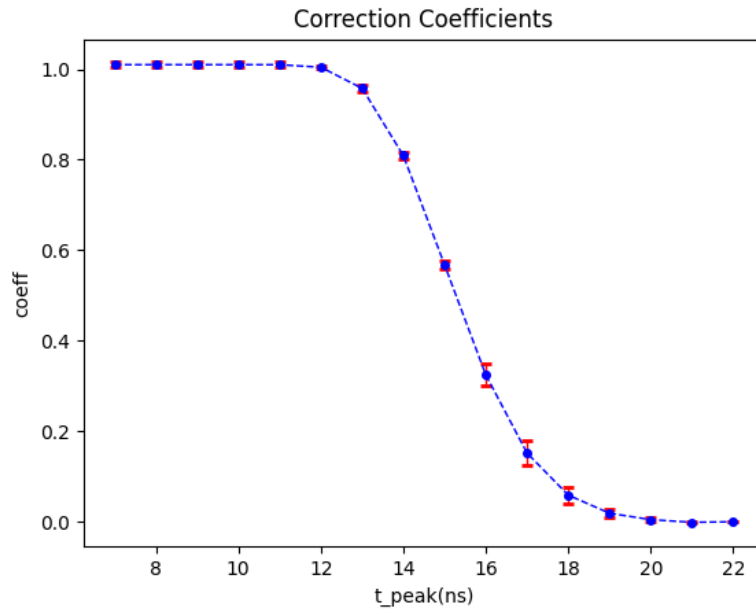


Figure 0.0.12: Μέση τιμή και τυπική απόκλιση των συντελεστών.

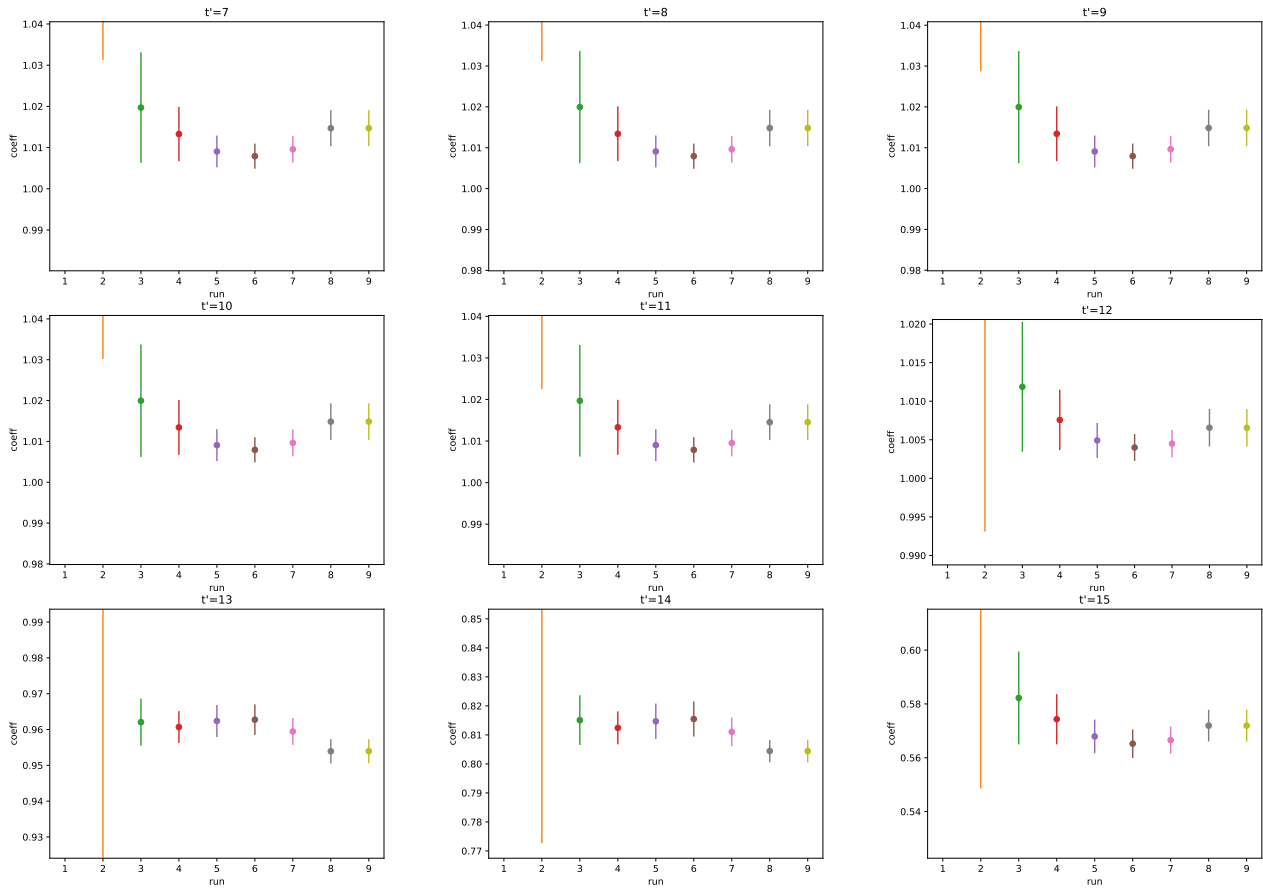


Figure 0.0.13: Συντελεστές σε σχέση με ένταση του φωτός. Υπάρχει μεγαλύτερη αβεβαιότητα για τα πρώτα 2 runs, αλλά ελαχιστοποιείται στις μεγαλύτερες εντάσεις.

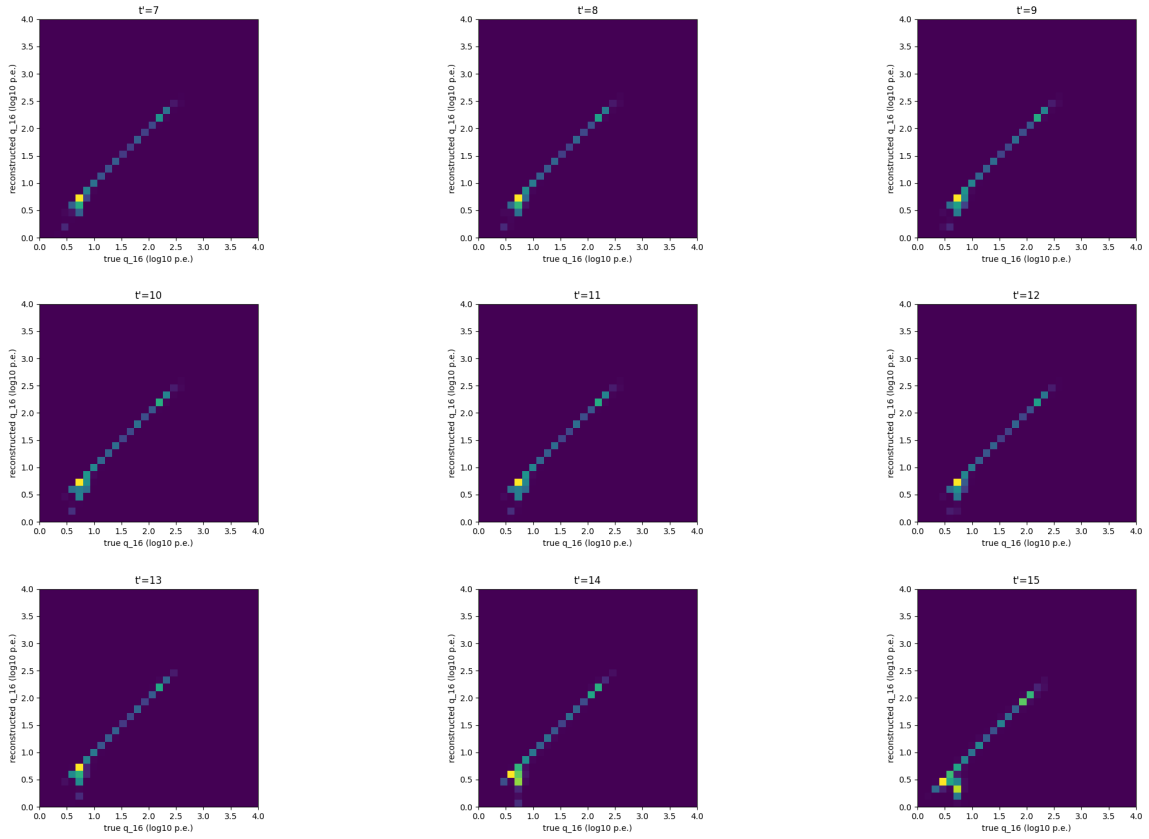


Figure 0.0.14: Cross-check ανάμεσα στο πραγματικό q_{16} των δεδομένων βαθμονόμησης και στο ανακατασκευασμένο q_{16} για τιμές χρόνου κορυφής από 7 ως 15 ns.

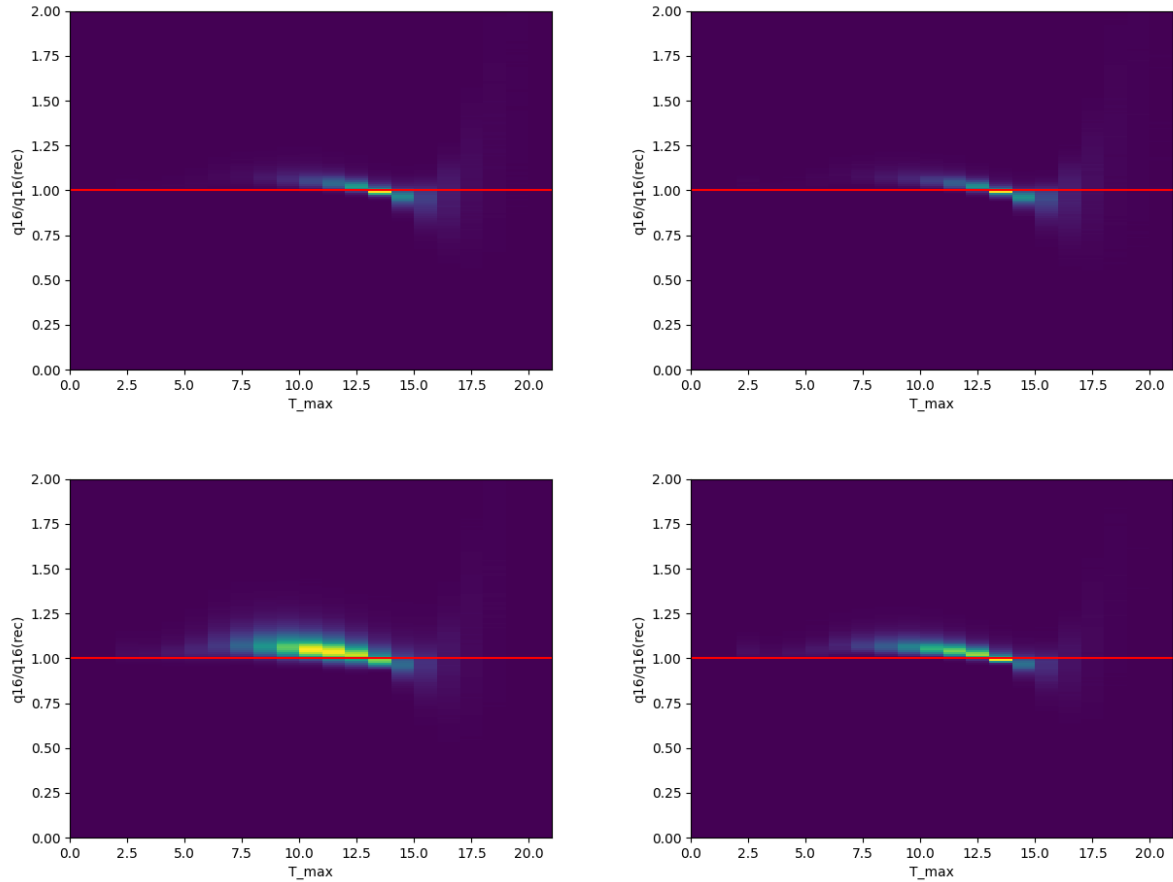


Figure 0.0.15: Αναλογία μεταξύ της πραγματικής τιμής q_{16} από τα δεδομένα παρατήρησης έναντι της ανακατασκευασμένης τιμής του χρησιμοποιώντας το q_9 και τους συντελεστές μας, σε σχέση με τον χρόνο της κορυφής. Τα διαγράμματα αντιστοιχούν σε διάφορα pixel των τεσσάρων τηλεσκοπίων. Τιμές διάφορες από το 1 για μεγαλύτερη απόκλιση στη θέση της κορυφής υπονοούν την ύπαρξη θορύβου. Επάνω αριστερά: CT1, Επάνω δεξιά: CT2, Κάτω αριστερά: CT3, Κάτω δεξιά: CT4.

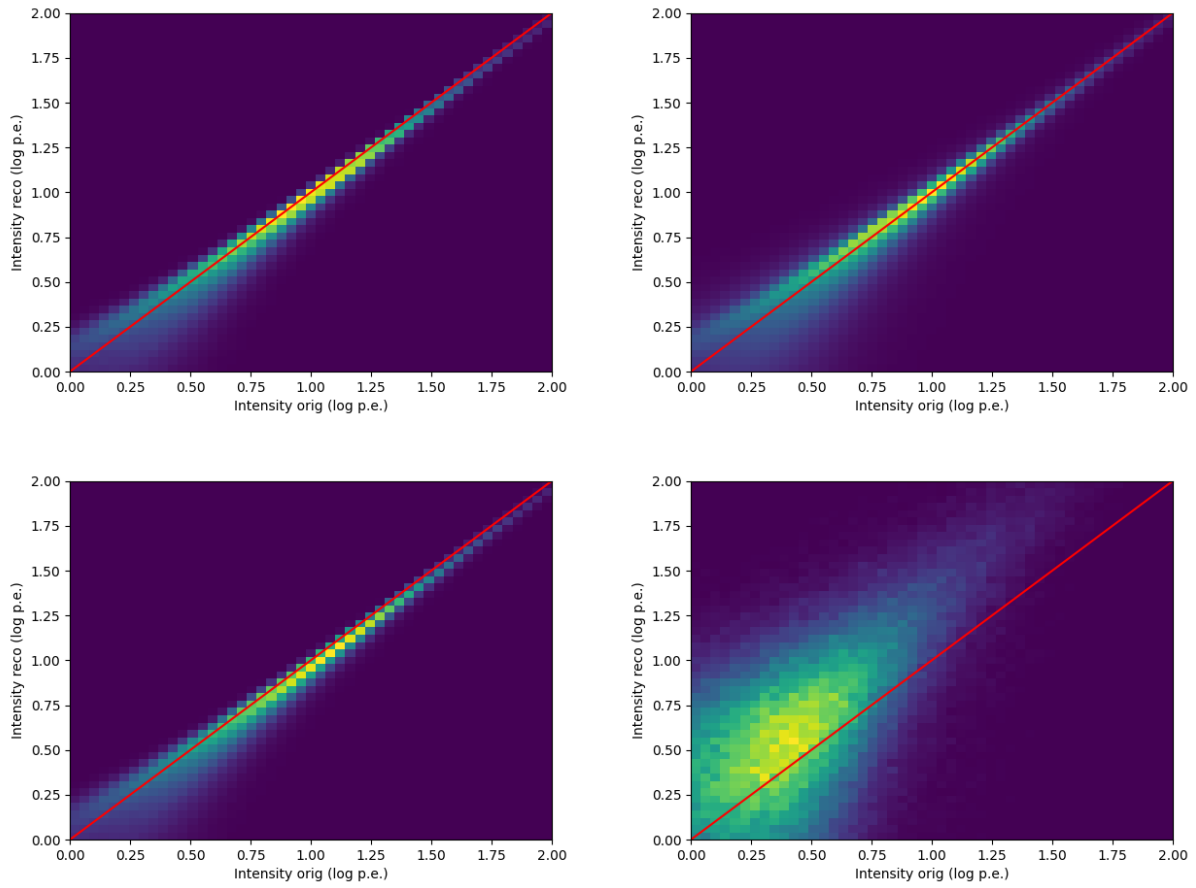


Figure 0.0.16: Σύγκριση μεταξύ της πραγματικής και της ανακατασκευασμένης έντασης από τα δεδομένα παρατήρησης. Καθώς ο χρόνος της μέγιστης έντασης αυξάνεται, υπάρχει μεγαλύτερη αβεβαιότητα. Επάνω αριστερά: CT1, $t=11$, Επάνω δεξιά: CT2, $t=9$, Κάτω αριστερά: CT4, $t=9$, Κάτω δεξιά: CT4, $t=19$.

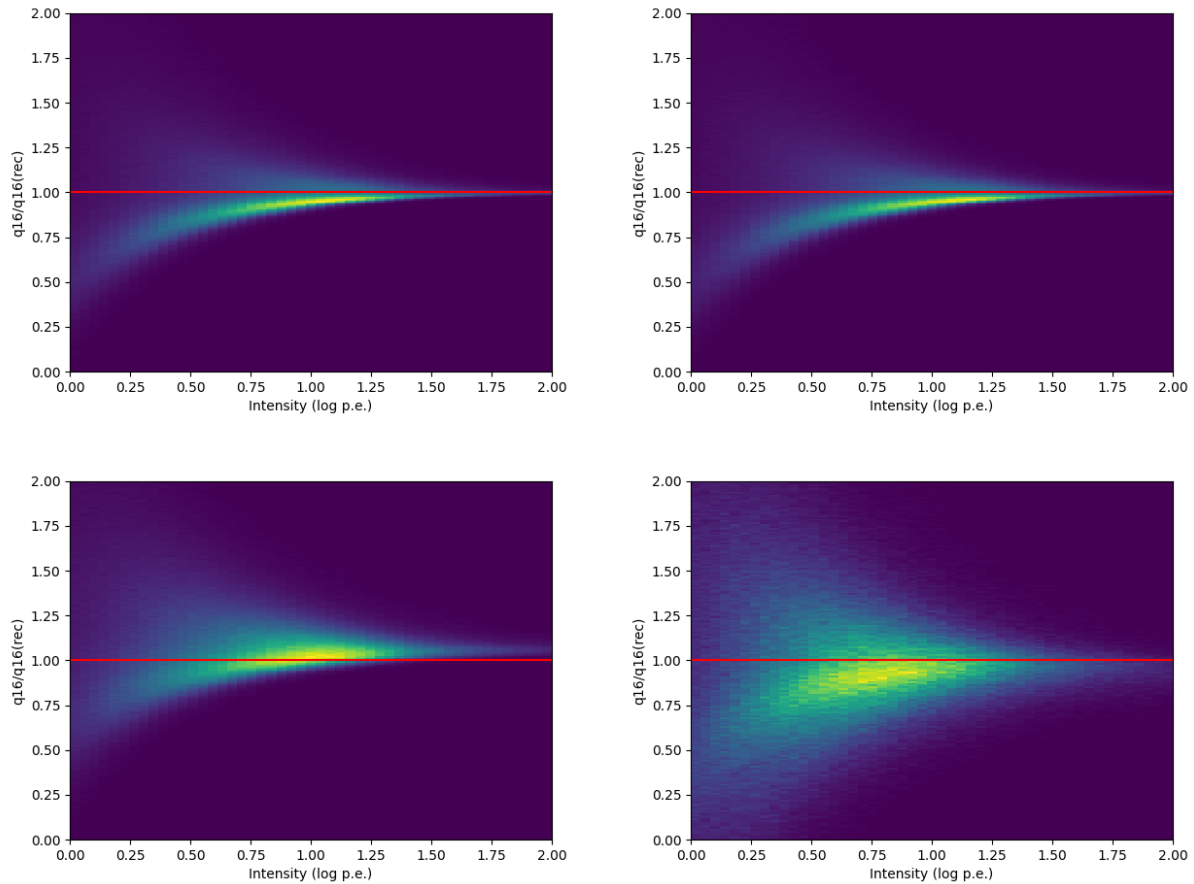


Figure 0.0.17: Αναλογία μεταξύ της πραγματικής και της ανακατασκευασμένης τιμής q_{16} από τα δεδομένα παρατήρησης σε σχέση με την ένταση. Βλέπουμε ότι για χαμηλότερη ένταση υπάρχει μεγαλύτερη αβεβαιότητα, όπως ήταν και στην περίπτωση του ελέγχου μας χρησιμοποιώντας μόνο δεδομένα βαθμονόμησης. Επίσης, καθώς ο χρόνος της κορυφής αυξάνεται, υπάρχει μεγαλύτερη αβεβαιότητα, πιθανώς λόγω θορύβου. Επάνω αριστερά: CT1, $t=13$, Επάνω δεξιά: CT2, $t=3$, Κάτω αριστερά: CT3, $t=10$, Κάτω δεξιά: CT3, $t=15$.

Συμπεράσματα

Λαμβάνοντας υπόψη όλα τα στοιχεία που έχουμε εξάγει από τα δεδομένα βαθμονόμησης, η παραπάνω εργασία οδήγησε σε σημαντικά αποτελέσματα. Πρώτον, η επαναρρύθμιση του παραθύρου ανάγνωσης θα οδηγήσει το σύστημα triggering να λειτουργεί στην κορυφή των σημάτων χαμηλότερης έντασης, καθιστώντας τα πιο κεντραρισμένα στα καταγεγραμμένα δεδομένα. Θα αντιμετωπίσει επίσης τον λανθασμένα βαθμονομημένο χρονισμό trigger του CT3, με αποτέλεσμα τη μεγαλύτερη ομοιομορφία στο χρόνο μεταξύ των τηλεσκοπίων. Επιπλέον, η χρήση global προσέγγισης για την περιγραφή της κερδούς των pixel με γραμμική εξίσωση φαίνεται να αντιπροσωπεύει επιτυχώς την κατανομή των δεδομένων βαθμονόμησης της κάμερας. Η σύγκριση με την παλιά μέθοδο δείχνει ένα μικρό αλλά αποδεκτό bias, ενώ ο νέος αλγόριθμος οδηγεί σε ένα πιο αξιόπιστο fit απαιτώντας λιγότερες επαναλήψεις. Τέλος, έχουμε επιτυχώς παραμετροποιήσει την ανάκτηση των δεδομένων charge mode χρησιμοποιώντας το ολοκλήρωμα εννέα δειγμάτων γύρω από την κορυφή του σήματος. Διενεργήσαμε ένα cross-check χρησιμοποιώντας τους παραγόμενους συντελεστές, με τις ανακατασκευασμένες τιμές από τις δεδομένες βαθμονόμησης να δίνουν μια πολύ κοντινή προσέγγιση των πραγματικών τιμών, ενώ το cross-check με δεδομένα παρατηρήσεων έδωσε ικανοποιητικά αποτελέσματα, υποδεικνύοντας όμως την ανάγκη να προσαρμόσουμε τη μέθοδό μας για τις συνθήκες υπό τις οποίες γίνονται οι πραγματικές παρατηρήσεις.

Συνολικά, η βαθμονόμηση της HESS-IU έχει επανεξεταστεί και βελτιωθεί. Επιπλέον, ο μετασχηματισμός από C++ σε python3 έχει σχεδόν εξαλείψει την εξάρτηση από το ROOT5, εξασφαλίζοντας πιο αποτελεσματική επεξεργασία δεδομένων. Η προσαρμογή της βαθμονόμησης τώρα μπορεί να γίνει χρησιμοποιώντας το HTCondor ή το σύστημα grid του DESY στο Zeuthen αντί του on-site server και απαιτεί μόνο περίπου 10 λεπτά αντί για περίπου 2 ώρες που χρειαζόταν προηγουμένως. Οι προτεινόμενες αλλαγές έχουν παρουσιαστεί σε collaboration meetings του H.E.S.S. και πρόκειται να εφαρμοστούν. Τέλος, σχεδιάζουμε να δημοσιεύσουμε μια εργασία σχετικά με τη global fitting μέθοδο για τη βαθμονόμηση του κέρδους ανά pixel.

Μελλοντικές εφαρμογές των τεχνικών και αντίκτυπο στο CTA

Οι έννοιες και ιδέες που παρουσιάζονται σε αυτή την εργασία έχουν την προοπτική όχι μόνο να επηρεάσουν τη βαθμονόμηση των καμερών HESS-IU και να βελτιώσουν την ποιότητα των δεδομένων που συλλέγουν από παρατηρήσεις, αλλά μπορούν επίσης να βρουν εφαρμογή και στις κάμερες του επόμενης γενιάς παρατηρητηρίου, CTA. Το Cherenkov Telescope Array (CTA) βρίσκεται αυτή τη στιγμή υπό κατασκευή και θα είναι το μεγαλύτερο και πρώτο παρατηρητήριο ακτίνων γάμμα με τοποθεσίες τόσο στο βόρειο όσο και στο νότιο ημισφαίριο. Οι κάμερες των μεσαίου μεγέθους τηλεσκοπίων (MST) του CTA που θα βρίσκονται στη La Palma, στην Ισπανία, θα χρησιμοποιούν επίσης το NeCTAr chip για το readout. Αυτό σημαίνει ότι και σε εκείνες τις κάμερες οι μέθοδοι βαθμονόμησης που σχετίζονται με το χρονισμό του παραθύρου ανάγνωσης και τον προσδιορισμό των κερδών των pixel μπορεί να επωφεληθούν από τις προτεινόμενες προσεγγίσεις σε αυτή την εργασία. Επίσης, η μέθοδος μετατροπής από sample mode σε charge mode μπορεί να υλοποιηθεί σε περίπτωση μελλοντικής λανθασμένης τοποθέτησης του παραθύρου ανάγνωσης λόγω αλλαγών στο υλικό.

Chapter 1

Introduction

1.1	Gamma-Ray Astronomy	44
1.1.1	Cosmic accelerators	44
1.1.2	Why Gamma Rays?	44
1.1.3	Generation mechanisms of γ -rays	45
1.1.4	Sources of VHE γ -rays	46
1.2	But how can we detect these photons?	48
1.3	Goals and organisation of the thesis	49

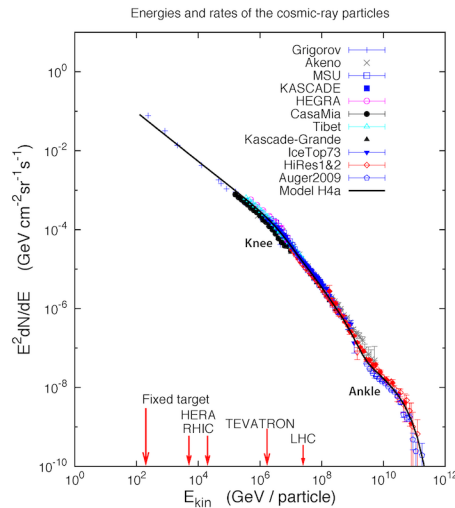


Figure 1.1.1: Energy spectrum of cosmic rays. The vertical axis indicates cosmic ray flux, which decreases with increasing particle energy. On the horizontal axis we see a comparison with the particle center of mass energy of colliders. Very high energy cosmic rays have a significantly higher energy than that of LHC (Large Hadron Collider). From [17].

1.1 Gamma-Ray Astronomy

Over the last thirty years, γ -ray astronomy has experienced many theoretical and technical advancements, allowing it to become a powerful means to investigate some of the deepest mysteries of the universe. This field consists of observing and analysing γ -rays of cosmic origin, such as those emitted by pulsars, supernovae and active galactic nuclei.

1.1.1 Cosmic accelerators

Cosmic rays were first discovered by V. Hess in 1912. They consist of high-energy particles (10^9 - 10^{20} eV, see Figure 1.1.1), mainly protons and nuclei, accompanied by a small percentage of electrons and positrons, which originate from astronomical sources [15]. Even though the origin of cosmic rays with energies less than 1 PeV is our Galaxy, the origin (galactic or extra-galactic) of higher energy cosmic rays (pevatrons) has not been identified [16]. Thus, the task of finding the cosmic accelerators which can accelerate particles up to such energies has not been completed yet. A challenge which is posed by the charged particles which cosmic rays mostly consist of is that they are constantly deviated by magnetic fields on their course to Earth. As a result, their original direction cannot be defined.

1.1.2 Why Gamma Rays?

The particles which can solve the above problem are photons. Since they have no charge, they travel through space in a straight line, allowing us to trace their origin. High-energy γ -rays are produced as secondary products of high-energy cosmic rays, as their components interact with their surrounding matter or radiation fields.

γ -rays are high energy electromagnetic radiation which corresponds to photons with energies greater than 0.5 MeV, while the highest energy γ photons detected so far reach 1.4 PeV [1]. They are situated at the shorter-wavelength end of the electromagnetic spectrum (Figure 1.1.2), beyond visible light and X-rays. In this work we will focus on very high energy (VHE) γ -ray astronomy, with photon energies in the TeV range, as they are tracers of high energy cosmic rays.

Other than identifying cosmic accelerators, VHE γ -ray astronomy can help scientists answer cosmological questions, along with advancing our knowledge in astrophysics and fundamental physics. For example, it can

The Electromagnetic Spectrum

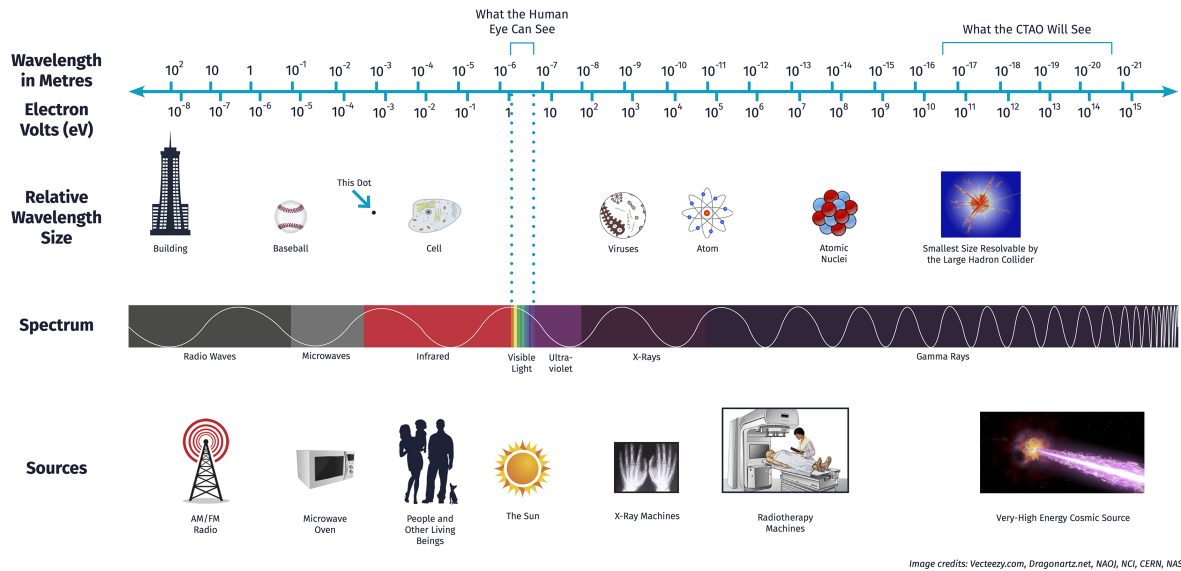


Figure 1.1.2: Electromagnetic spectrum, relative wavelength size and sources. Gamma rays are at the higher energy part of the spectrum. Cherenkov telescopes are able to detect very high energy cosmic sources from the ground. Image from the website of the Cherenkov Telescope Array (CTA) observatory[7].

be a very helpful tool in estimating the extragalactic background light and in the search for dark matter, which will give meaningful information about the history of the universe.

1.1.3 Generation mechanisms of γ -rays

Since cosmic rays consist of protons, nuclei, electrons and positrons, their origin can either be leptonic (caused by electrons and positrons) or hadronic (caused by protons and other nuclei) [2].

Gamma rays of leptonic origin

When an electron or positron enters a radiation field in a sparse interstellar medium, it can produce a high energy photon through two main processes: Inverse Compton (IC) scattering and synchrotron radiation [18]. The Inverse Compton effect occurs when a high-energy electron or positron interacts with a low-energy photon, reducing its own energy and increasing the photon's energy in the process. A special case of Inverse Compton scattering is bremsstrahlung, where a photon is emitted during the interaction of the electron or positron with the ions or atoms of the surrounding medium. On the other hand, synchrotron radiation photons are emitted when the electron or positron enters a magnetic field.

Gamma rays of hadronic origin

A different process occurs when cosmic rays go through regions of higher density medium. The interaction of high energy protons and nuclei with matter produces secondary particles, predominantly charged and neutral pions [2]. Subsequently, a considerable portion of the initial energy of the cosmic rays is carried by the γ -rays produced in the π^0 decays¹.

¹Neutral pion decay: $\pi^0 \rightarrow \gamma\gamma$.

1.1.4 Sources of VHE γ -rays

There are multiple types of sources in the universe emit very high-energy γ -rays. When using ground-based detectors, we focus on detecting emission in the TeV range, as emission in the GeV range or lower is more diffuse in the night sky and thus it does not help us distinguish between sources. Many of the studied sources, as seen in Figure 1.1.3 are situated within the plane of our galaxy. Though, there are also extragalactic ones that exist outside of it, which are planned to be studied with the newer generation observatories (Fig. 1.1.4). We briefly discuss the main source classes below.

Supernova remnants

The explosion which follows the death of a massive star causes the outer layers of the star to be propagated into the interstellar medium. This blast forms a supernova remnant (SNR). Depending on their morphology, supernova remnants are categorised into shell type SNRs, which display a bright shell in the X-ray domain and less intense emission in their interior, and composite SNRs, which have a shell-like structure and also contain a pulsar within them [20].

Supernova remnants are believed to be the sources of galactic cosmic rays with up to 1000 TeV energies, as only 10% of the explosion's energy needs to be converted to cosmic rays in order to reach this quantity[2]. The detection and analysis of VHE γ -rays from SNRs can give us meaningful insight into their composition and whether they indeed accelerate mostly hadrons, the main components of cosmic rays, as the origin of the photons can be either hadronic or leptonic. Different approaches and models are being used in order to answer this question.

Pulsars and pulsar wind nebulae

A supernova explosion can lead to the formation of a pulsar, a neutron star whose magnetic field is misaligned with its rotation axis, creating a fast spinning magnetic dipole. Since the rotating field causes a steep voltage drop, they act as cosmic accelerators, sending electrons and positrons into the interstellar medium along the lines of the magnetic field. The areas of emission are considered to be located at the polar caps and the "outer gap". The outer gap is believed to be the region in the magnetosphere near the light cylinder, where the rotating lines of the magnetic field rotate with the speed of light[21]. This wind of electron-positron pairs reaches a shock, where its pressure is equal to the pressure of the encompassing nebula, with its kinetic energy causing the random motion of the electrons and positrons and resulting into the formation of a pulsar wind nebula (PWN), which can be detected through inverse Compton γ -rays. The first and most studied PWN ever detected is the Crab Nebula[22], leading to the establishment of PWNs as a significant group of VHE γ -ray sources.

Binary systems

Binary systems consist of a compact object, usually a black hole or pulsar and an accompanying star. Matter from the star accretes to the compact object, creating jets where particles are accelerated to very high energies, causing very strong radiation and magnetic fields. These fields can generate γ -rays via different mechanisms, depending on the type of the compact object and its companion. For example, a pulsar accompanied by a massive star with an intense photon field, can create γ -rays through IC scattering, as the photons interact with the relativistic particles in the pulsar wind[20].

Stellar clusters and stellar winds

Stellar clusters consist of stars concentrated in a relatively small volume. They can contain stars in all stages of their life, including SNRs and pulsars, as well as massive stars with compact companions. The interaction between the dense stellar winds of massive stars is believed to generate a shock, accelerating particles and producing TeV γ -rays [2].

Active Galactic Nuclei

A large number of identified extragalactic sources belong in the class of Active Galactic Nuclei. Active Galactic Nuclei (AGN) are remote galaxies which exhibit a very bright nucleus. They comprise of a supermassive

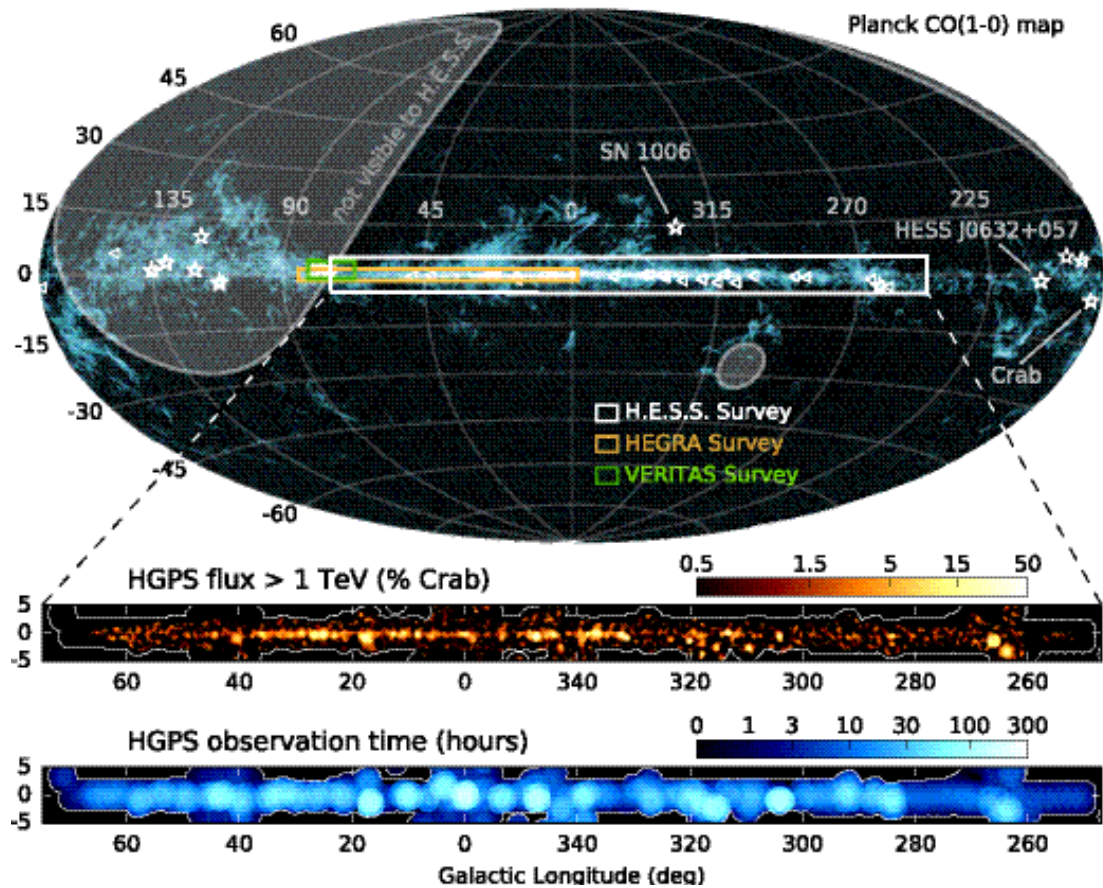


Figure 1.1.3: The H.E.S.S. Galactic Plane Survey (HGPS), with data from H.E.S.S. observations until 2016 superimposed with the data from previous surveys by HEGRA and VERITAS experiments, as well as data from FermiLAT, of which galactic sources are marked with triangles, while extragalactic sources are marked with stars. Figure from [3]

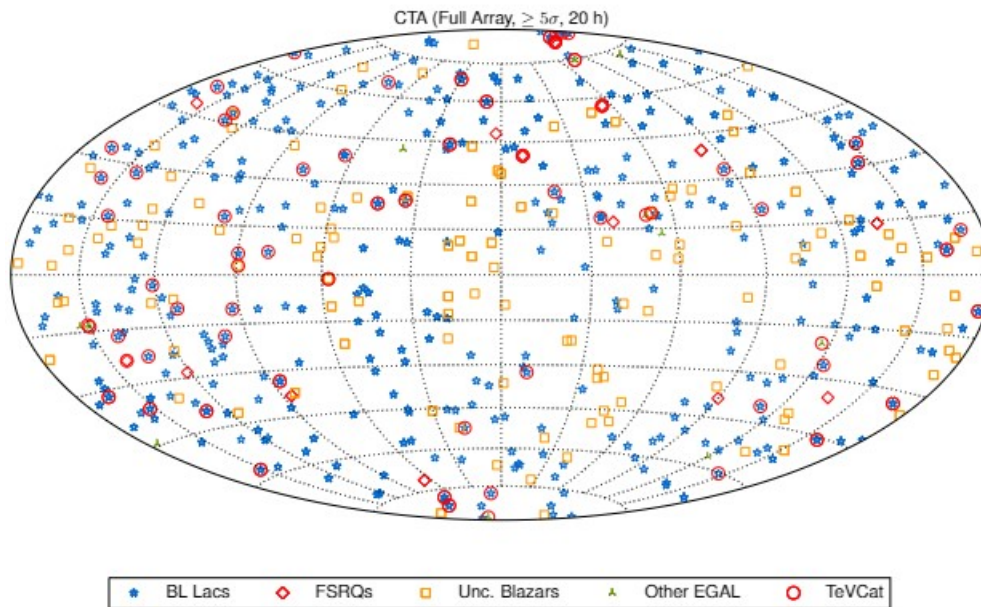


Figure 1.1.4: Predicted extragalactic sources to be detected by the CTA Observatory. From [19].

black hole which accretes matter from the host galaxy, forming a large accretion disk. They appear point-like in existing observations, due to the resolution of the current detection instruments.

Nearby galaxies, starburst galaxies and galaxy clusters

Other extragalactic sources include nearby galaxies, starburst galaxies and galaxy clusters. Nearby galaxies exhibit diffuse γ -ray production during the interaction of their cosmic rays with the interstellar medium. Starburst galaxies are galaxies with a high rate of supernova production along with a high gas density, creating a perfect environment for particle acceleration and VHE γ -ray production. Galaxy clusters are very large gravitationally bound systems, containing a high number of cosmic-ray sources. The accelerated particles lead to emission of VHE γ -rays, through their interaction with the interstellar medium.

Gamma Ray Bursts

Gamma Ray Bursts (GRBs) are violent explosions characterised by an intense release of energy in very short time (ranging from milliseconds to a few seconds). This energy, oftentimes exceeding the amount of energy released by the Sun throughout its lifespan, is released in the form of lower energy γ -rays. The light from a GRB is diffused uniformly across the sky, suggesting it originates from stellar sources[2]. Typically, it is followed by an afterglow which can have a duration of up to a few months.

1.2 But how can we detect these photons?

Since γ -ray photons do not penetrate the Earth's atmosphere, directly detecting γ -rays of celestial origin is possible only in space. There have been various detectors which have been sent to space, attached to satellites or balloons. One of these is FermiLAT, the Large Area Telescope on the Fermi Gamma-ray Space Telescope, which was sent to space in 2008[23]. Though, space-borne detectors cannot detect VHE γ -rays, as higher energy photons are statistically rarer and need higher detection surface area and exposure time, which is not feasible in space[24]. The most popular way to detect photons at very high energies is through the secondary products they produce when interacting with the Earth's atmosphere, creating extensive air showers. This practice has become very successful in the last thirty years with the development of the Cherenkov technique.

The Cherenkov technique allows scientists to research the γ -ray flux entering the Earth, through telescopes equipped with special fast cameras able to record the Cherenkov light caused by photons entering the at-

mosphere. The air shower images can then be reconstructed based on the light distribution on the camera. Experiments using this technique, like the High Energy Stereoscopic System (H.E.S.S.) have been essential for the detection of numerous, now known, sources.

As a means to avoid unreliable or false results, it is necessary to ensure the proper operation of these systems. The Cherenkov technique heavily relies on the accuracy of the telescope cameras. To guarantee correct observations and the longevity of the cameras, we need to minimise the effects of external factors on the cameras' sensitivity. Thus, all the camera components need to be calibrated frequently, in order to minimise the effects of environmental changes, as well as their aging.

1.3 Goals and organisation of the thesis

This thesis aims to revisit the calibration of the HESS-IU cameras of the H.E.S.S. telescope array, introducing three improvements in the readout window positioning, gain adjustment and retrieval of partially missing data. These improvements will lead to sped up calibration and more robust results.

It consists of 6 chapters. The content of each chapter is presented briefly below²:

- In chapter 1 we make a brief introduction about gamma-ray astronomy and its importance. We also mention the goals and discuss about the organisation of this thesis.
- In chapter 2 we talk about ground-based gamma-ray detection, Imaging Atmospheric Cherenkov Telescopes and the High Energy Stereoscopic System.
- In chapter 3 we discuss more in detail about the HESS-IU camera, its architecture and calibration techniques.
- In chapter 4 we introduce our two proposed calibration changes regarding readout window adjustment and a new approach for determining the pixel gain.
- In chapter 5 we present a parametrisation which allows to reconstruct incomplete data using their recorded part.
- Finally, in chapter 6 we conclude the thesis and talk about future prospects.

²The template used for this thesis is adapted from [25].

Chapter 2

Very High Energy γ -ray ground-based detection

2.1	Introduction	52
2.2	Atmospheric showers	52
2.2.1	Processes involved in the development of showers	52
2.2.2	Cherenkov radiation	53
2.3	Detection techniques	55
2.3.1	Photomultiplier tubes	57
2.3.2	Sampling experiments	58
2.3.3	Imaging Atmospheric Cherenkov Telescopes	58
2.4	The H.E.S.S. experiment	59
2.4.1	The H.E.S.S. telescopes	61
2.4.2	H.E.S.S. Phase I	61
2.4.3	H.E.S.S. Phase II	63
2.4.4	Camera upgrades	65
2.4.5	Central trigger system, data acquisition and monitoring	66
2.4.6	Event selection	67
2.5	The next generation observatory: CTA	67

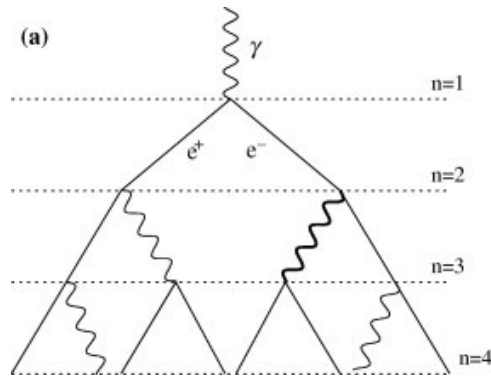


Figure 2.2.1: Schematic representation of an electromagnetic air shower. From [26]

2.1 Introduction

Gamma ray emission is tightly connected to cosmic rays, as the very high energy (VHE) cosmic ray particles interact with the interstellar medium, producing VHE photons. Even though cosmic rays were first discovered by Victor Hess in 1912, it took more than 70 years for the first detection of a VHE γ -ray source in 1989. Since then, there have been numerous advancements in the field of detection, taking advantage of the secondary products of the entrance of VHE photons in the atmosphere: charged particles and Cherenkov photons. In this chapter we will discuss about the atmospheric cascades caused by γ -rays and how they can be detected, mainly focusing on the Cherenkov technique and the H.E.S.S. telescopes.

2.2 Atmospheric showers

Upon entering the atmosphere, a high energy photon will interact with its atoms, producing a cascade of events: the photon will interact with the Coulomb field of the atmospheric nuclei, leading to an electron-positron production; the electron and positron, upon interaction with the Coulomb field will lead to the production of new lower (high) energy gamma rays; these gamma rays will produce new electron-positron pairs and so on. These type of events is an Extensive Air Shower (EAS)[5].

2.2.1 Processes involved in the development of showers

There are two main processes which participate in the development of atmospheric showers initiated by high energy photons:

- Conversion of the photon to an e^\pm pair (pair production) in the Coulomb field of atmospheric nuclei
- Bremsstrahlung of the e^\pm pair in the Coulomb field, producing new high energy γ -photons

A simplified scheme of this process can be seen in Figure 2.2.1 According to the Heitler model for extensive air showers [26], these two dominant processes are determined using the same characteristic length, referred to as the electromagnetic radiation length:

$$X_0 = \left[4\alpha r_e^2 \frac{N_A}{A} Z^2 \ln \left(183 Z^{-\frac{1}{3}} \right) \right] \quad (g/cm^{-2}) \quad (2.2.1)$$

where Z and A are the mass and atomic numbers of a nucleus, α is the fine structure constant, r_e the electron radius and N_A the Avogadro number.

Meanwhile, if we define a density-integrated depth $X(z) = \int_z^\infty \rho dz$, the bremsstrahlung process during traversing this depth will cause an energy loss of

$$E(X) = E_0 \exp \left(-\frac{X}{X_0} (1 + b) \right) \quad (2.2.2)$$

where E_0 is the initial energy of the incident photon and $b = \frac{1}{18 \ln(183Z^{-\frac{1}{3}})}$. In air, $b = 0.0122$. According to this equation, an electron (or positron) will have lost on average half of its energy in air at a depth $R = X_0 \ln 2$. This energy is considered to be transferred to a single γ -ray, while the pair-production probability in relation to the depth X is equal to:

$$\mu(X) = 1 - \exp\left(-\frac{X}{X_0} \left(\frac{7}{9} - \frac{b}{3}\right)\right) \quad (2.2.3)$$

In the atmosphere, the radiation length is equal to 36.7 g cm^{-2} , meaning that the atmosphere (under the assumption that the maximum altitude of development of showers is roughly 10 km) acts as a calorimeter of ~ 27 radiation lengths. Though, the atmosphere is not an ideal calorimeter, as it has inhomogenous density depending on the altitude, with increasing density as the altitude drops. This results in a faster evolution of the electromagnetic shower at higher depth, as there are more atmospheric nuclei for the photons or electrons to interact with.

If the atmosphere functioned as a homogenous calorimeter, then the depth of the shower maximum would have a logarithmic relationship with the energy of the initial particle. Though, in reality the depth of the shower maximum evolves slower, as can be shown with a simplified model of a hydrostatic atmosphere [27] where pressure P and density ρ are exponential functions of the altitude z : $P(z) = P_0 \exp(-z/z_0)$ $\rho(z) = \rho_0 \exp(-z/z_0)$, where $z_0 = RT/gM$ (R the perfect gas constant, T absolute temperature, M equivalent molar mass of air, g gravity acceleration) and $\rho_0 = 1.2 \text{ kg/m}^3$. It is proven that the altitude of maximum shower development is:

$$z_{max} = z_0 \ln\left(\frac{r_0 z_0}{X_0 \ln \frac{E_0}{E_c}}\right) \quad (2.2.4)$$

where E_c is the critical energy where ionization losses become important, equal to 83 MeV in the air. The above relationship indicates that the altitude does not evolve logarithmically with E_0 . For $E_0 = 1 \text{ TeV}$, $z_{max} \approx 9 \text{ km}$.

In addition to the two processes mentioned above, some other processes affect the development of a shower at lower energies, namely scattering of charged particles, ionization and atomic excitation losses (leading to energies below the critical energy), positron annihilation and the unisotropy of the Earth's magnetic field.

At high energies, the interaction of nuclei with photons and electrons sometimes leads to the initiation of hadronic showers, but with a much smaller rate ($\sim 10^{-3}$). These showers comprise of hadronic components (protons, neutrons, nuclear fragments, pions, K mesons), electromagnetic components due to the decay of neutral pions, muons from the decay of charged mesons, as well as neutrinos from the decay of charged mesons and muons. These showers are more irregular and exhibit greater variability than electromagnetic showers. A comparison of simulation results of electromagnetic and hadronic showers can be seen in Figure 2.2.2.

2.2.2 Cherenkov radiation

Even though a charged particle, such as an electron, moving in a straight line with constant speed in vacuum does not emit radiation, an electron moving uniformly through a dielectric medium with a speed greater than the phase velocity of light in that medium can induce radiation[4]. This type of radiation is called Cherenkov radiation. When a charged particle moves through the medium, it polarizes the molecules of the medium, which will then emit the energy they were given in the form of radiation. If the charged particle is moving with a lower velocity than light, the radiation will be emitted along a spherical wavefront, moving with the speed of light in the medium. Though, in the case of Cherenkov light, where the velocity of the charged particle is greater than the velocity of light in the dielectric medium, the photons will be emitted along a conical wavefront with an opening angle θ_c , referred to as the Cherenkov angle:

$$\theta_c = \arccos\left(\frac{c}{nv}\right) \quad (2.2.5)$$

where n is the refractive index of the dielectric medium, v the speed of the charged particle and c the speed of light in vacuum. An illustration of this phenomenon can be seen in Figure 2.2.3.

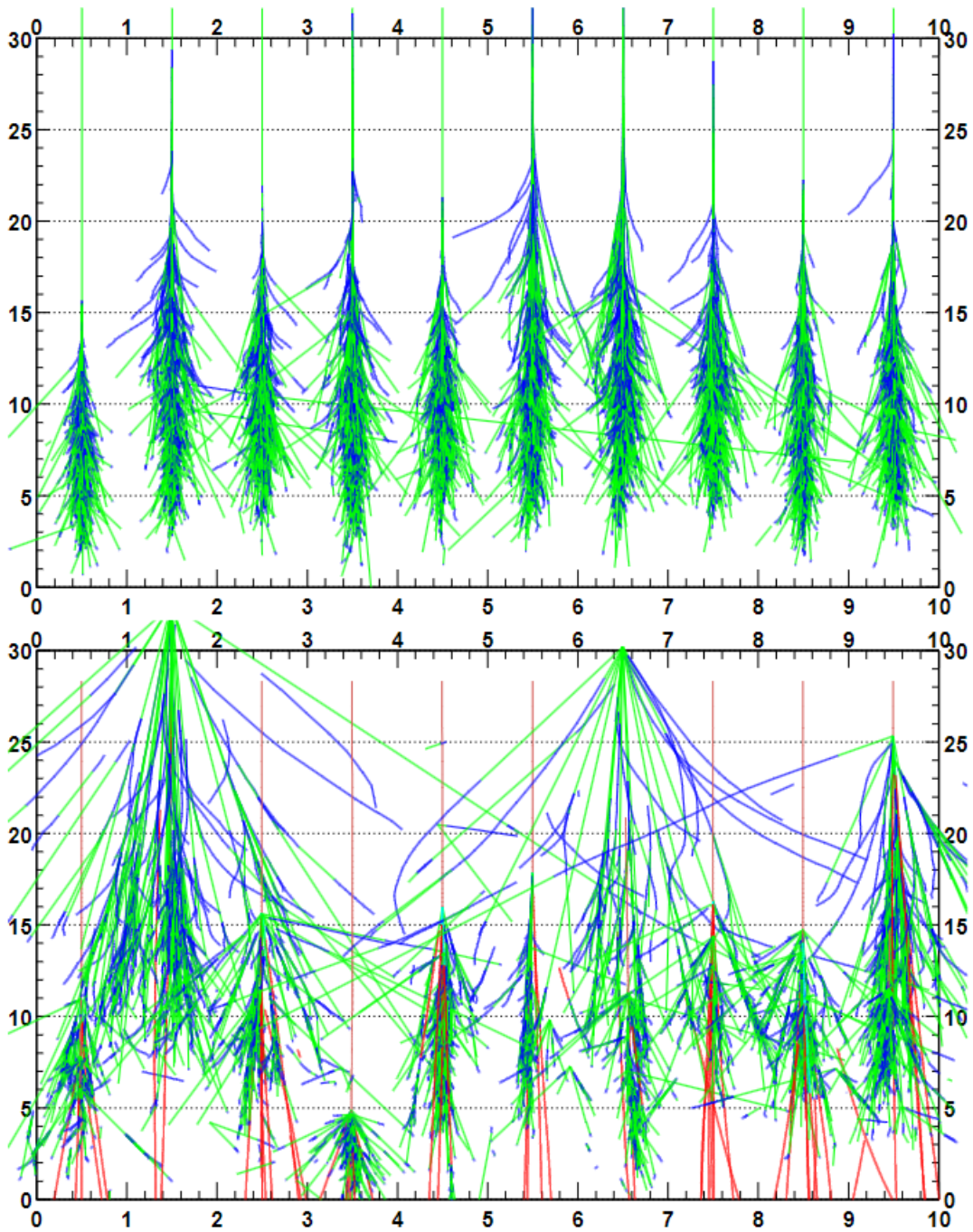


Figure 2.2.2: Top: Simulation of 10 electromagnetic showers initiated each by a γ -ray of 300 GeV. Bottom: Simulation of 10 electromagnetic showers initiated each by a proton of 300 GeV, showing larger fluctuations. From [28].

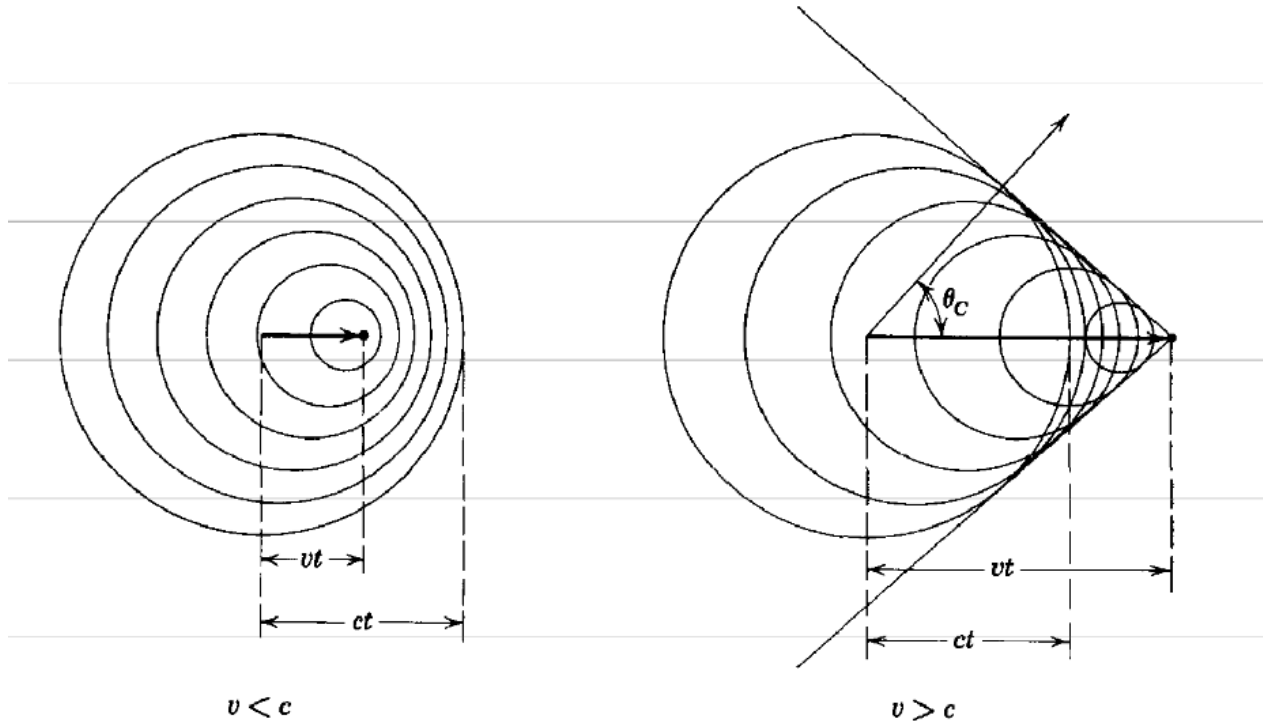


Figure 2.2.3: Illustration of Cherenkov radiation. Left: spherical wavefronts of radiation from a charged particle moving with a velocity less than the velocity of light through the dielectric medium. Right: conical wavefronts of radiation from a charged particle moving with a higher velocity than that of light. From [4].

It is proven that the amount of Cherenkov photons above a wavelength λ_0 emitted in an air shower [27] does not depend on the local density, and is also proportional to the primary energy E_0 :

$$N(\lambda > \lambda_0) = \frac{2X_0 A}{\rho_0 \lambda_0} \times \frac{E_0}{E_c} \quad (2.2.6)$$

where $A = 2.68 \times 10^{-5}$ photons. It is noteworthy that Cherenkov emission below $\lambda_0 = 300nm$ is almost fully absorbed in the atmosphere.

The radius of Cherenkov emission from a shower produced by a particle at an altitude z is:

$$r = 2.4 \times 10^{-2} \times z e^{-\frac{z}{2z_0}} \quad (2.2.7)$$

The varying density of the atmosphere causes an increase of the Cherenkov angle closer to the ground, compensating the effect of the varying distance from the ground and creating an annulus on the ground of a maximum radius (for $z = 2z_0$) $r_{max} \approx 150m$, for the range of altitudes where most electromagnetic showers are initiated. An illustration of the generation of the light pool is shown in Fig. 2.2.4.

2.3 Detection techniques

Indirect ground-based detection of γ -rays has an advantage over direct space-borne detectors in the VHE regime, as the gamma-ray flux decreases with increasing energy, thus needing a large collection area, which cannot be achieved in space. There are plenty of large scale VHE γ -ray detectors, which either detect some of the secondary particles produced in air showers or detect Cherenkov light emission. One of the largest challenges these techniques faced over the years of their development, was the huge night sky and cosmic ray background, not allowing them to discriminate between sources. With the development of technology, the newer generation of instruments has been able to tackle these problems and detect a numerous galactic and extragalactic VHE sources.

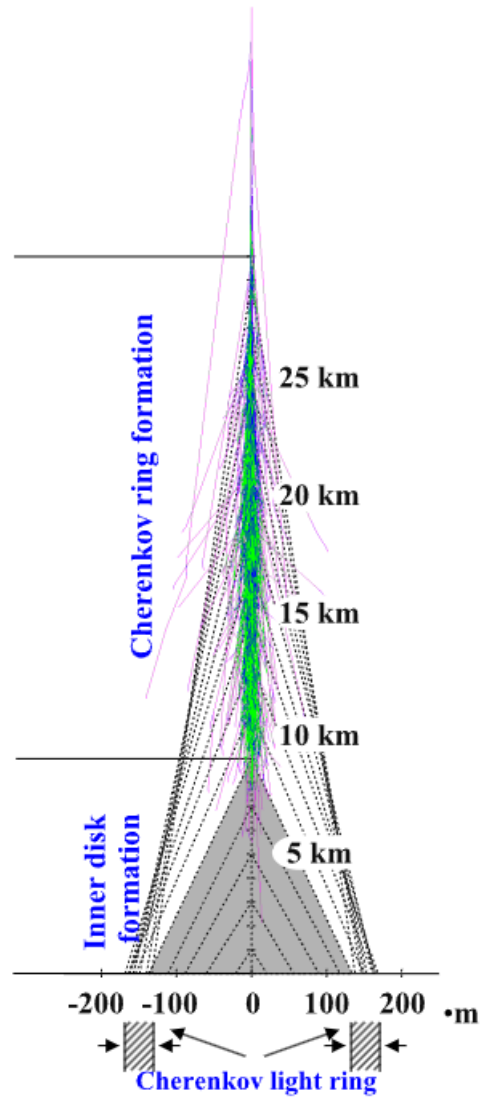
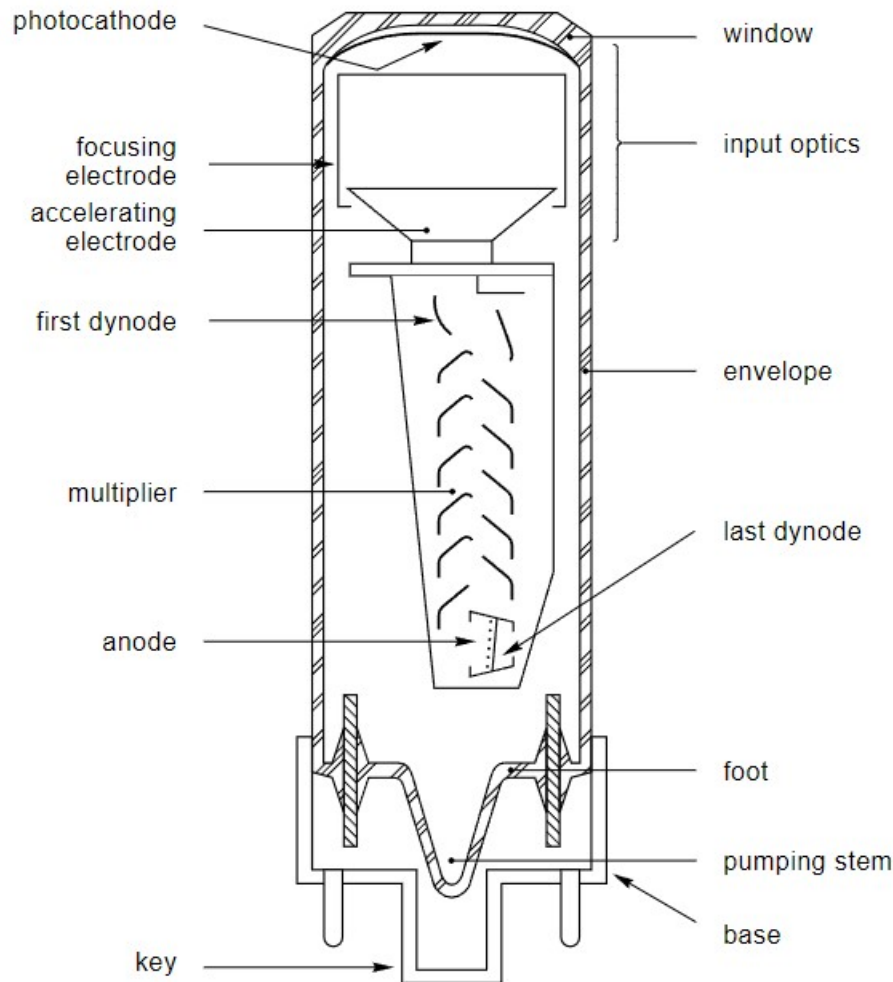


Figure 2.2.4: Shower development and generation of Cherenkov light pool. From [27]



MRB100

Figure 2.3.1: Elements of a photomultiplier tube (PMT). From [29].

2.3.1 Photomultiplier tubes

Photomultiplier tubes (PMTs) are highly sensitive detection devices which convert low-intensity light to an electronic signal, and subsequently amplify it via emission of secondary electrons, so that it can be used in various analyses[29]. These two main processes are called photoemission and secondary emission.

The fundamental elements of a PMT can be seen in Figure 2.3.1. When a photon of sufficient energy is absorbed by the PMT's photocathode, it is converted to an electron (photoelectron or p.e.) via photoemission due to the photoelectric effect. The energy of the photoelectron is equivalent to the energy of the incident photon. The electron flux is then focused and accelerated by an electron-optical system, consisting of an electric field created by a focusing and an accelerating electrode. It is then directed to a series of secondary emission electrodes with increasing voltage, dynodes, where it is multiplied by the process of secondary emission. Specifically, when the photoelectron hits the first dynode, it causes the emission of more electrons, which then hit the second dynode, each repeating the first process and resulting into a significantly higher number of electrons. Finally, an anode, a charged electrode at a higher voltage than the dynodes, collects the electrons from the multiplier, creating an output signal in the form of electric current. The amplitude of the signal is proportional to the intensity of the initial light and can be measured to determine its properties.

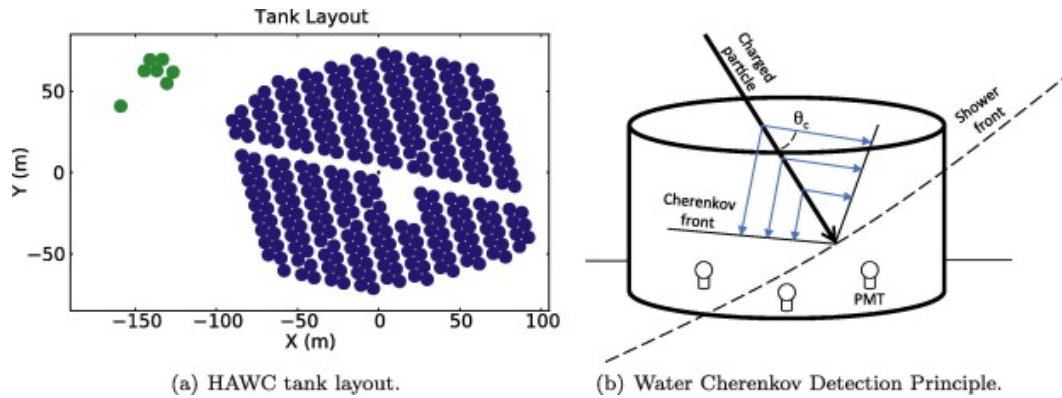


Figure 2.3.2: Left: Layout of the HAWC tanks. The green tanks correspond to its VAMOS (Verification And Measuring of Observatory System) array. Right: Operating principle of the Water Cherenkov Technique: relativistic charged particles constituting an air shower front emit Cherenkov radiation with an angle θ_c as they travel through the water. PMTs at the bottom of the tank detect this Cherenkov radiation. From [31].

2.3.2 Sampling experiments

Instead of detecting the Cherenkov light, the particle sampler technique is based on sampling the charged particles at the shower tail, the moment it reaches the ground, creating a "snapshot" of the shower front [5]. The advantage of these detectors is that they have a 100% duty cycle, as they can detect charged particles regardless of weather conditions or time of the day and they have a large ~ 2 sr field of view. They have a higher energy threshold, as only higher energy photons induce showers that keep developing until reaching the ground.

In the Water Cherenkov Technique (WCT), photomultiplier tubes (PMTs) are placed in a water tank in the form of an array. These PMTs detect the Cherenkov light emitted when the secondary air shower particles enter the water. The working principle of such detectors can be seen in Figure 2.3.2, right. The Cherenkov angle is quite large in water, approximately 41° degrees, meaning that the PMTs can be placed with a large distance between them, thus covering a big area of detection. Notable experiments in this category include The Multiple Institution Los Alamos Gamma-Ray Observatory (MILAGRO) [30] and the High-Altitude Water Cherenkov (HAWC) experiment [31].

Another type of sampling experiments are extensive air shower arrays, which employ particle detectors, such as resistive plate counters, over a wide area, in order to directly detect the particles at the shower wavefront. This technique is used by the Astrophysical Radiation with Ground-based Observatory at YangBaJing (ARGO-YBJ) [32] in Tibet, and the Large High Altitude Air Shower Observatory (LHAASO) [33] in China.

2.3.3 Imaging Atmospheric Cherenkov Telescopes

The Imaging Atmospheric Cherenkov Telescope (IACT) technique, introduced by the Whipple collaboration [34], employs optical telescopes which measure the Cherenkov radiation induced by electromagnetic showers. Since most showers, initiated by a γ -ray and following its same direction, create a light pool with an effective angle of $\sim 1^\circ$ with a diameter in the order of 250m, they can be detected by one or more telescopes located in the light pool. The telescopes can measure the incident Cherenkov photons and indirectly determine the arrival direction of γ -rays in the Earth's atmosphere. Their working principle can be seen in Figure 2.3.3.

In IACTs, a large reflective area (mirror) collects Cherenkov photons and reflects them on a focal plane where the camera is located. It consists of PMTs, which function as camera pixels. PMTs are preferred as detectors in such observatories, as they can amplify the quite weak Cherenkov signals with minimal noise and a rapid response in the nanosecond range, while their spectral response aligns with the spectrum of Cherenkov light at 300-400nm, in the ultraviolet and blue wavelengths [20]. The telescopes employ high speed front-end electronics which allow them to efficiently process the electrical signals generated by the PMTs.

These signals are then used to reconstruct an image of the shower.

An IACT structure consists of numerous aluminium reflectors in spherical, hexagonal or square mirror facets with a size of 0.5-1 m. The number of reflectors in telescopes can vary, giving current Cherenkov telescopes different diameters, from 4 to 28m. The difference in diameter accounts for sensitivity to different γ -ray energy ranges. A medium size telescope (10-12m) typically has a few hundreds of mirror facets. These mirror facets are usually arranged in a Davies-Cotton[35] or in a paraboloid design. The Davies-Cotton design employs identical mirror facets in shape and orientation, arranged to form a spherical surface, while the alignment procedure is quite straightforward. Nevertheless, even though it has a good on-axis performance, the quality of the image deteriorates further from the center of the focal plane. On the other hand, paraboloid design requires mirror facets of different sizes, making the alignment process more difficult, but providing a better off-axis performance with the drawback of worse on-axis performance. Another difference in performance between the two designs is that Davies-Cotton requires longer charge integration times, since the light from the reflectors reaches the cameras at different times, in contrast to the paraboloid arrangement, where the light from all reflectors arrives to the camera simultaneously. Thus, the choice between the two designs depends on the diameter of the telescope, with Davies-Cotton usually used for small to medium sized telescopes (≤ 12 m).

Additionally, the camera at the focal plane of the mirror typically has a field of view of $\sim 3^\circ - 5^\circ$, ensuring it can capture the Cherenkov image of a whole shower, as the latter usually has a $\sim 1^\circ$ angle size. Typically, a camera of a medium-size telescope consists of 500-1000 PMTs acting as pixels, with a field of view of $\sim 0.1^\circ - \sim 0.3^\circ$ each. As a result, the effective detection area of such a telescope is equal to the surface of the Cherenkov light pool, at around $50000m^2$, much larger than that of space-based γ -ray direct detectors which is in less than $1m^2$. Light concentrators are generally placed in front of the pixels, in order to eliminate dead space between them and cut off any stray light. The telescope camera records an image of the shower, showing its track and pointing back to the source from which the initial γ -ray was emitted. From the intensity and shape of the image, one can determine the energy of the γ -ray and orientation of the shower, as well as reject unwanted background. Though, with just one telescope observing the shower, it is challenging to reconstruct its direction. For this reason, newer generation observatories use multiple telescopes, which view the shower from different angles, allowing it to be reconstructed stereoscopically[6], as seen in Figure 2.3.4.

This technique faces two challenges: distinguishing between Cherenkov light produced by electromagnetic showers, and Cherenkov light produced by hadronic showers; and discriminating between actual Cherenkov photons and night sky background (NSB). The first problem can be tackled by examining the Cherenkov light pattern, as it tends to be more irregular with hadronic showers. Meanwhile the second one requires the telescopes to be operated with as little surrounding light as possible: they are located at dark sites higher than sea level, with minimal light pollution and are operated at conditions of no moonlight and clear sky. This is necessary because the Cherenkov radiation induced by air showers is quite faint compared to NSB photons: Cherenkov photons from a 1 TeV γ -ray induced shower are a few hundred per m^2 at a 2 km from sea level, in contrast to 10^{12} photons/ $m^2/s/sr$ of NSB. Though, the special circumstances needed for observation give IACTs a quite small duty cycle compared to other detectors. Furthermore, since the flow of NSB photons is maximum at higher wavelengths, its detection can be reduced by using PMTs with maximum quantum efficiency in the range of 300-400nm. Another means to suppress it are using small time windows of a few tens of ns to integrate the charge induced by the Cherenkov photons and permitting coincident detection between multiple PMTs and telescopes.

2.4 The H.E.S.S. experiment

The High Energy Stereoscopic System (H.E.S.S.) is a system of five Imaging Atmospheric Cherenkov Telescopes located in the Namibian savannah (Figure 2.4.2). The observatory's name also serves as a tribute to Victor Hess, who first discovered cosmic rays. Operating fully since 2004, its purpose is to investigate the γ -rays arriving to Earth from cosmic sources with energies ranging from 30 GeV to 30 TeV. Situated in near the Gamsberg mountain, an area renowned for its optical conditions, it allows scientists to observe sources with a γ -ray flux equal to a small fraction of the flux of the most radiant source in the sky, the Crab Nebula. The H.E.S.S. telescope array is split in two phases: Phase I consists of four 12-meter telescopes, of which the first one began operating in 2002, while the other three were in full operation by 2004; Phase II introduced a larger fifth 28-meter telescope in 2012, aiming to increase sensitivity to lower energy ranges. A timeline of

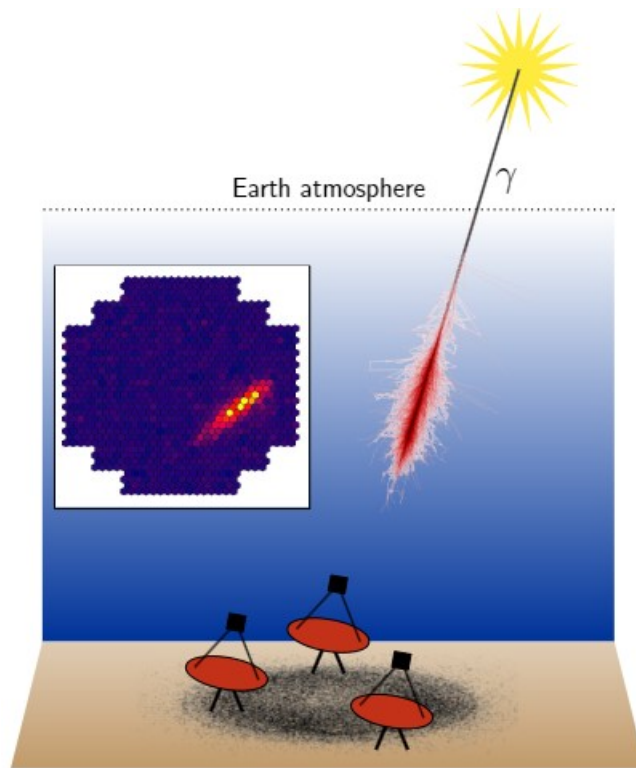


Figure 2.3.3: Schematic illustration of the IACT technique. Telescopes detect an extensive air shower induced by a high energy gamma-ray. The source is depicted with a yellow star, while the red tracks denote the paths of the secondary particles. The Cherenkov light pool on the ground is depicted with black. From [36].

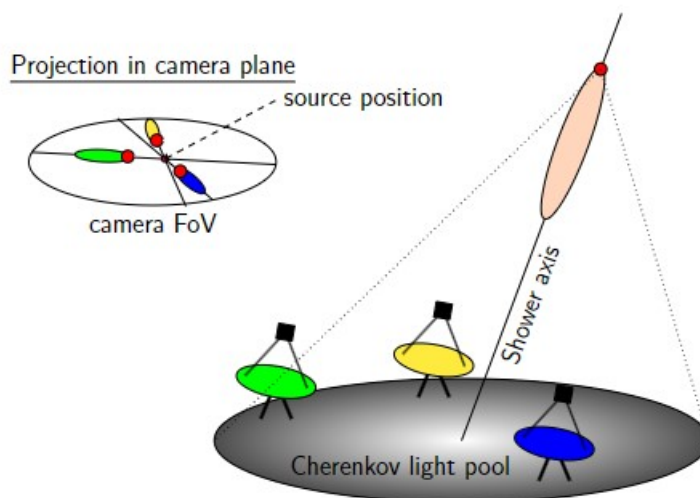


Figure 2.3.4: The stereoscopic technique, where different telescopes view the same shower from different angles, allows more reliable geometric reconstruction of the shower and its properties. The images of all telescopes are superimposed in order to find the actual impact point. From [36].

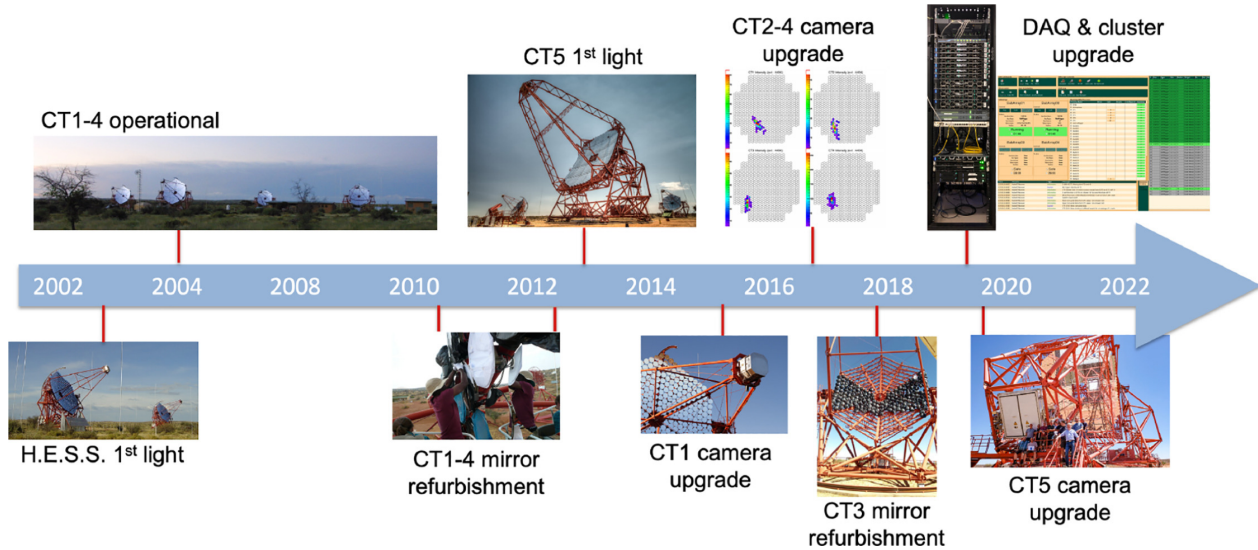


Figure 2.4.1: A timeline illustrating the major hardware updates of H.E.S.S. From [37].

the major upgrades during the operation of H.E.S.S. can be seen in Figure 2.4.1.

The H.E.S.S. collaboration involves over 260 scientists from 40 institutions representing 13 different countries, while its research has resulted in the discovery of new, both steady and transient, γ -ray sources and the publishing of numerous articles in prolific scientific journals. It has also earned various distinctions, including the Descartes and Rossi prizes, as well as recognition as the 10th most influential observatory on a global scale, among the Hubble Space telescope and the European Southern Observatory (ESO)[38].

2.4.1 The H.E.S.S. telescopes

The H.E.S.S. telescopes use the Imaging Atmospheric Cherenkov technique to view γ -induced atmospheric showers from different angles and stereoscopically reconstruct their spatial properties. The 4 Phase-I 12 m telescopes, referred to as CT1-4, are arranged in the form of a square with 120m sides, while the large 28 m Phase-II telescope, CT5, is located in the middle of the square[6] (see Fig. 2.4.2). The square's diagonal is aligned with the north-south orientation. The spacing between CT1-4 was chosen in such way to offer balance between two major requirements: more than one telescope should be able to "see" a shower and a better stereoscopic view requires a significant distance between telescopes. If the telescopes were much further away from each other, it would not be possible for showers to be recorded by more than one telescope, as the Cherenkov light pool has a maximum diameter of 250m. On the other hand, the smaller the distance between telescopes, there is a smaller difference in the viewing angle, as showers are initiated at a height of 9-10 km. Phase II brought a significant advancement to the system, as CT5, with a 600 m^2 mirror dish was added to the center of the square, considerably extended the observatory's energy coverage, sensitivity and angular resolution.

2.4.2 H.E.S.S. Phase I

The optical system of CT1-4 is described in [6], [39] and [40]. The telescopes employ an alt-azimuth mount configuration, which allows them to be directed at any celestial object in the night sky. The mount mechanism, constructed as steel space frames, employs a base frame, which enables rotation around the vertical axis supporting the dish that in turn rotates around the elevation axis. One of the telescopes and technical drawings can be seen in Figures 2.4.4 and 2.4.5. The rotation control is performed by a computer, with the drive system for each axis consisting of a servo-controlled AC motor and a battery-driven DC motor for backup, with the servo controllers and batteries situated within a small hut at the base frame. These motors exert rotation forces on 7 m radius circular rails, mitigating the required drive forces. The drive systems operate at a maximum speed of 100 degrees per minute, to facilitate swift transitions between different celestial sources. Ensuring pointing accuracy, both axes are connected to angular-resolution encoders consisting of



Figure 2.4.2: An overview of the H.E.S.S. array, with CT1-4 arranged in a square and CT5 in the middle. From [36].

a 17-bit digital readout accompanied by supplementary analog tracking, and yielding a resolution in the order of a few arc-seconds. For the same monitoring purpose, the observatory also employs an optical guide telescope with a focal length of 800 mm and equipped with a CCD camera. This auxiliary system is used to make up for deviations from optimal pointing. In terms of weight, a complete H.E.S.S. I telescope, including the camera, mirrors and drive system, weighs roughly 60 tons.

As mentioned above, Cherenkov telescope observations depend on a mirror which focuses Cherenkov photons from an air shower on the camera. Thus the area of the mirror and the quality of the reflected image (commonly assessed through point spread function) highly impact the performance of the telescope. CT1-4 mirrors consist of 382 round mirror facets of 30 cm radius (Figure 2.4.6), crafted from aluminized glass with a quartz coating, contributing to a total 108 m^2 mirror area. Since the mirror of each of these telescopes has a diameter of $d = 12 \text{ m}$, the mirror arrangement follows a Davis Cotton design, covering part of a sphere with a radius equal to the mirror's focal point $f = 15 \text{ m}$. This means that the d/f ratio is equal to 0.8, providing good imaging also for off-axis Cherenkov light rays. Before installation, each mirror facet undergoes tests for reflectivity and image quality, in order to ensure that the mirror reflectivity for Cherenkov wavelengths is higher than 80%.

The alignment of the mirror facets is checked regularly so that the light from a source is reflected on a single point on the camera. This process is done using a CCD camera located on each telescope, which points to a star. Then, the orientation of each facet is adjusted automatically by two remote-controlled motors, so that the image of the star is reflected only on one point at the focal area of the camera. The initial alignment is done over the course of a few nights, while it gets frequently tested for deviations, which can be corrected over a few hours. The mirrors are calibrated to focus on objects approximately 10 km away, corresponding to the typical air shower initiation distance. The point spread function used to determine the quality of an image equals 0.03° on-axis and 0.06° for rays that are 2° off-axis. The width of a spot increases with distance to the optical axis, while slight the elevation-dependent variation is uncritical.

The cameras of the H.E.S.S. I array consist of 960 PMTs acting as pixels, organised in 60 modules, called "drawers", with 16 PMTs each, containing the electronics responsible for amplification, digitisation and discrimination of signals. Each camera triggers with a coincidence of a specified number of pixels in overlapping sectors of the camera, while if more than one camera has triggered for an event, the signals of the corre-

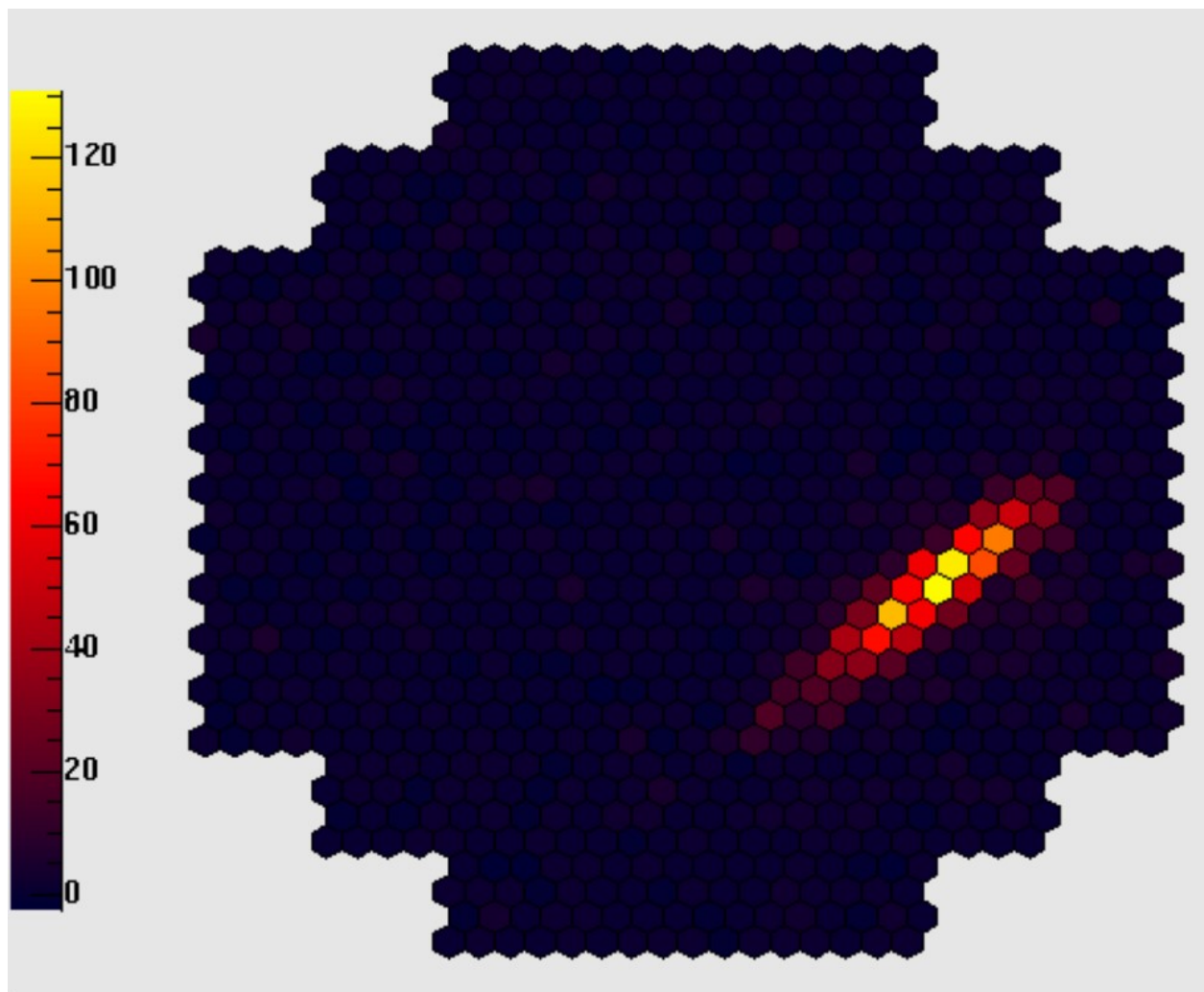


Figure 2.4.3: One of the first Cherenkov images recorded by CT1 in 2002, illustrating a typical elongated view of an air shower. From [6].

sponding telescopes are stored, in order to stereoscopically reconstruct the shower image. A Cherenkov image recorded by one camera from an air shower can be seen in Figure 2.4.3.

2.4.3 H.E.S.S. Phase II

The structure of the 28 m H.E.S.S. Phase II telescope (Fig. 2.4.7), CT5 is designed following the same principles as the 12 m telescopes. It also features an alt-azimuth dish mount configuration with a notable intrinsic rigidity. Its azimuth drive system consists of 12 wheels in 6 bogies running on a 36 m diameter rail, with 4 of these wheels being controlled by motors. Its maximum pointing speed is $200^\circ/\text{min}$, while its range of motion is $\pm 280^\circ$ from park position. Meanwhile, its elevation drive system, acting on an elevation axis of 24 m, consists of a rack and pinion on each side of the dish, while it employs 2 drive units of 2 motors each. Its maximum pointing speed is $100^\circ/\text{min}$, with a range of motion equal to $-125^\circ - +90^\circ$ from the vertical axis. The dimensions of the dish are $32.6 \times 23.4\text{m}$, which is equivalent to a dish with a diameter of 28 meters. The camera is upheld by a quadrupod structure, with connections extending to the dish. Finally, the complete CT5 telescope weighs 580 tons.

The CT5 mirror is arranged in a parabolic configuration, in order to minimise the time dispersion for its larger mirror dish. The 875 mirror facets of 90cm size, supported by a 5×5 planar mirror support grid, are hexagonal to optimise coverage and aligned in a shape approximating a parabola. They are roughly 2.5 times

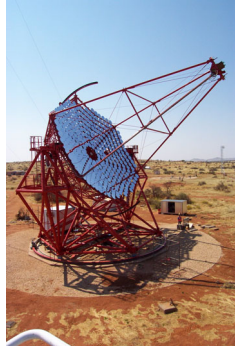


Figure 2.4.4: A 12 meter H.E.S.S. Phase I telescope. From [6].

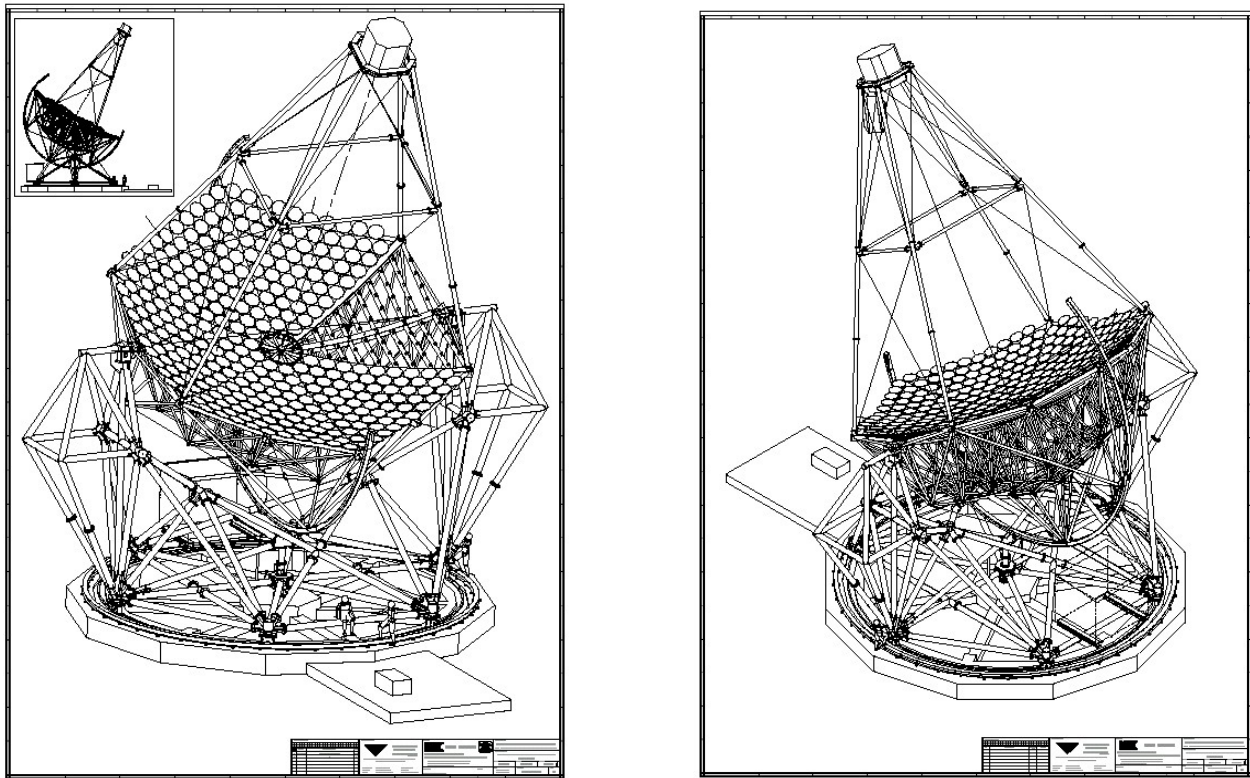


Figure 2.4.5: Technical designs of H.E.S.S. Phase I telescopes. From [6].

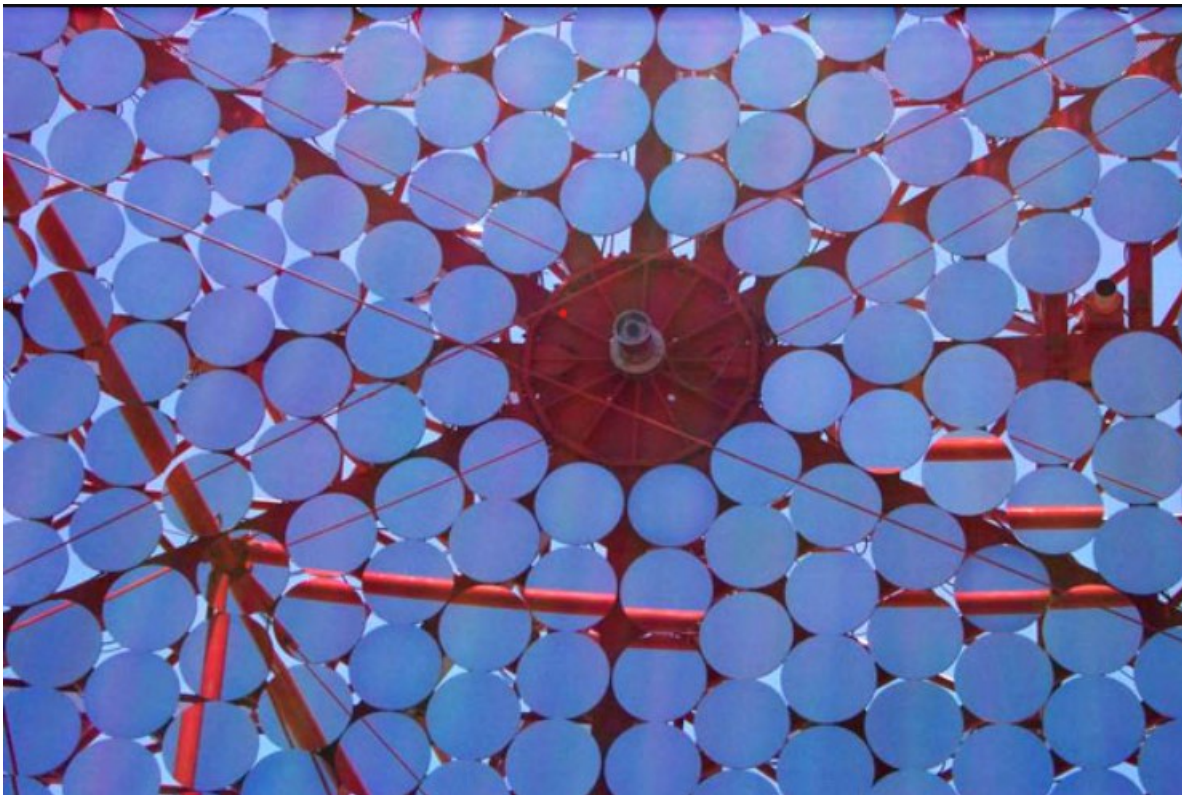


Figure 2.4.6: Mirror facets of a H.E.S.S. I telescope. From [6].

the area of the mirror facets of H.E.S.S. I telescopes, weighing 25 kg. each and made out of quartz-coated aluminized glass. The total mirror area amounts 614 m², while the mirror's focal length is equal to 36 m. The mirror facets are aligned using the same technique as the one for CT1-4, with the aid of 2 actuators with 2 μm positioning step size for each facet, corresponding to a facet tilt step of 1 arc second.

Additionally, the H.E.S.S. II camera is designed with the same principles as the H.E.S.S. I cameras, employing PMTs grouped in drawers of 16 PMTs each with similar electronics. Though, it is much larger, containing 2048 PMTs arranged in 128 drawers. This, along with the larger focal length, corresponds to a much higher resolution compared to the cameras of the smaller telescopes, allowing it to detect showers of lower energies. The camera also has a 10 times higher image recording rate.

2.4.4 Camera upgrades

The cameras of all five telescopes have gone through upgrades, during which newer electronics developed for the next generation observatory, CTA (Cherenkov Telescope Array), were used in order to assess their performance.

Starting in 2015, the cameras of the smaller H.E.S.S. I telescopes were upgraded (HESS-IU). The main goal of this upgrade was to lower the energy threshold of CT1-4, so that they could record more events along with CT5. Additionally, the aging electronics were difficult to maintain after 14 years of operation. Every component of the camera was replaced, except for the PMTs. The most important part of the upgrade was the use of the NECTAR (New electronics for the Cherenkov Telescope Array) readout chip, which acts as a cyclical analogue memory buffer which can store input PMT signals with a sampling frequency of 1 ns, and has a significantly small readout dead-time.

In 2020, the camera of CT5 was also replaced with a FlashCam, which was also developed for the medium sized telescopes of CTA[41]. FlashCam has a fully digital design, enabling operation at very high event rates and precise trigger adjustment. At the same time, its novel design allows it to record events of very high intensity, with a dynamic range of up to 3000 photoelectrons.

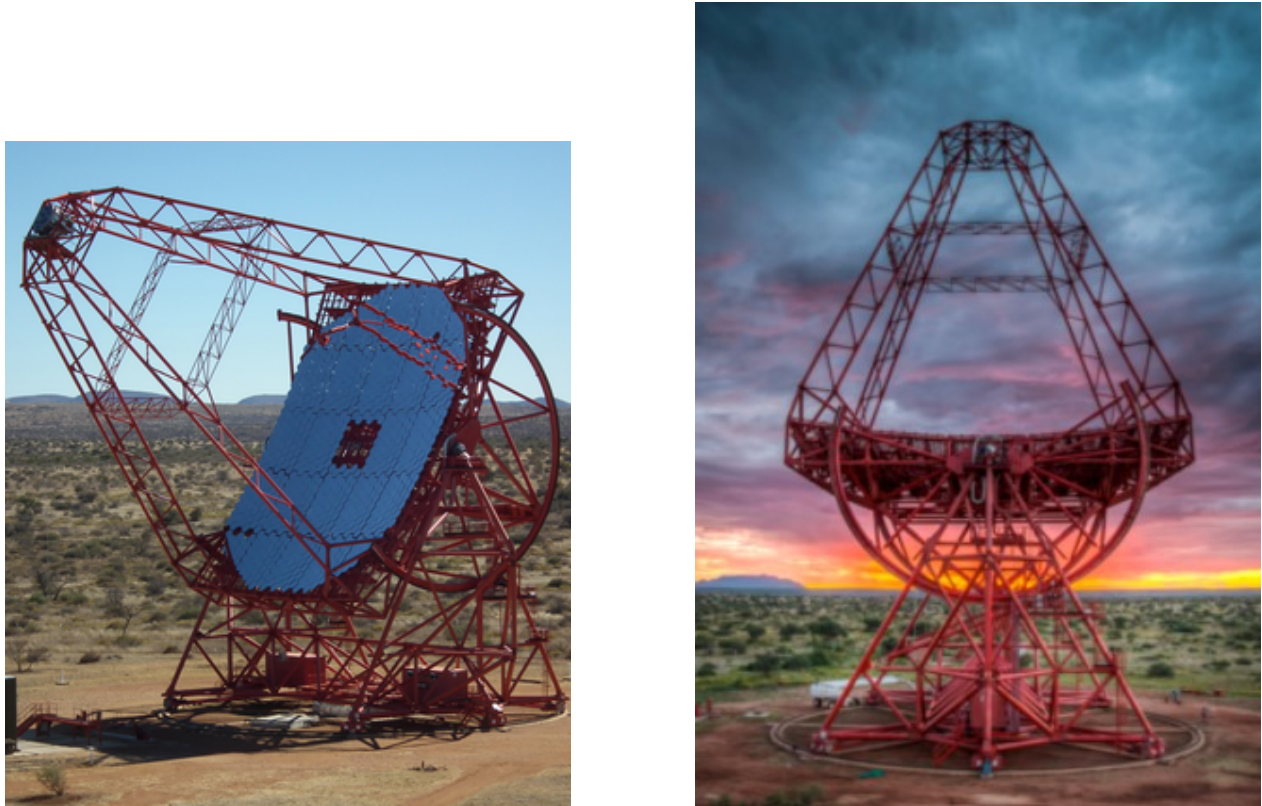


Figure 2.4.7: The 28 m H.E.S.S. Phase II telescope. From [6].

2.4.5 Central trigger system, data acquisition and monitoring

H.E.S.S. uses the stereoscopic reconstruction technique in order to deduce information about air showers, including their direction and the type and energy of the primary particle from which they were induced. Consequently, only events detected by two telescopes simultaneously are recorded, as information from just one telescope is not enough for stereoscopic reconstruction. This is done automatically before any data processing, serving as a means of lightening the load on the Data Acquisition (DAQ) system, decreasing readout dead-time, and facilitating the lowering of triggering and energy thresholds. Upon receiving a trigger signal from a telescope, the central trigger system scans for trigger signals from other telescopes, correctly taking into account varying delays between triggering signals from individual telescopes due to different pointing angles. When more than two telescopes have a coincident observation over the required thresholds, the data are read out. Alternatively, if triggers do not coincide, the telescope's readout electronics are quickly reset, so that they are ready for the next event. The trigger system permits triggering on all combinations involving more than one of the 5 telescopes. Though, for the purpose of keeping a lower energy threshold, after the installation of CT5, all events over the necessary threshold seen by it are recorded, regardless of coincidences with other telescopes.

The DAQ system gathers the data from the different telescopes and the site's monitoring instruments, subsequently processing and analysing them in real time. The data is then stored locally in RAID servers and sent to Europe via Internet.

The optimal quality of data collected by the system is ensured by continuous monitoring of its performance. This includes recording currents and counting rates of the camera PMTs, the camera temperatures, as well as calibration techniques and instruments, discussed more in detail in Chapter 3. Two CCD cameras are also included in the monitoring system, one mounted parallel to the optical axis of each telescope and looking at the sky, serving to correct the telescope pointing using stars, and the other placed in the centre of the dish and looking at the telescope's camera, used to align mirror facets.

Finally, atmospheric monitoring provides the correct relationship between the incident Cherenkov light and

the energy of the primary particle, as it varies depending on the atmosphere's optical transmission. H.E.S.S. is equipped with instruments such as infrared radiometers to measure the sky temperature, an active cloud sensor which scans the sky for clouds by means of a laser beam, an optical telescope which is used to measure atmospheric transmission with the help of stars, and, lastly, a meteorological station.

2.4.6 Event selection

For each observation run, the data that is used for event reconstruction undergoes an image cleaning process, where the noise is cut off, with the goal of leaving only the pixels that have observed Cherenkov light and rejecting those that contain only night sky background. H.E.S.S. uses a two-level filter, which selects pixels satisfying the following two conditions: their measured amplitude should be above a threshold of 5 photoelectrons, and they should have at least one neighbour with an amplitude of more than 10 p.e.[3]. This approach identifies spatially correlated features within the image, which are indicative of the Cherenkov light from air showers. This technique is a way to minimise variations in the shower pattern in a consistent manner, while maintaining a low complexity.

Following the process of image cleaning, a γ -ray shower typically exhibits a narrow elliptical shape, whereas images of background hadronic events exhibit a broader and more irregular appearance. Subsequently, the Hillas parameters (a set of geometric features used in the analysis) are computed for each cleaned image, serving as the foundation for event selection. Furthermore, the total amplitude of the image after cleaning is determined, alongside the calculation of the image's mean position within the camera, which corresponds to the center of the ellipse. These parameters can subsequently be used for stereoscopic event reconstruction.

2.5 The next generation observatory: CTA

Cherenkov Telescope Array (CTA)[7] is going to be the biggest gamma-ray observatory ever built, with sites both in the northern and southern hemispheres, providing coverage over the entire sky. It will combine information from telescopes of different sizes, allowing to precisely detect the direction of gamma-ray emission, giving scientists a new view of the high energy sky. Three different telescope classes will be used: Small Size Telescopes (SST, ~ 4 m), Medium Size Telescopes (MST, ~ 12 m), and Large Size Telescopes (LST, ~ 23 m). The northern hemisphere array, located in La Palma, Spain, will focus on low to mid energy ranges of 20 GeV to 5 TeV, employing 4 LSTs and 9 MSTs. At the same time, the southern hemisphere array, located in the Atacama desert in Chile, will use observations from 14 MSTs and 37 SSTs.

Chapter 3

The HESS-IU Camera

3.1	Introduction	70
3.2	Architecture of the HESS-IU Camera	70
3.2.1	Front-end electronics	70
3.2.2	Back-end electronics	74
3.2.3	Sensors and calibration devices	76
3.2.4	Camera network and software	77
3.3	Camera calibration	77
3.3.1	Readout	77
3.3.2	Pixel calibration parameters	78
3.3.3	Trigger	80

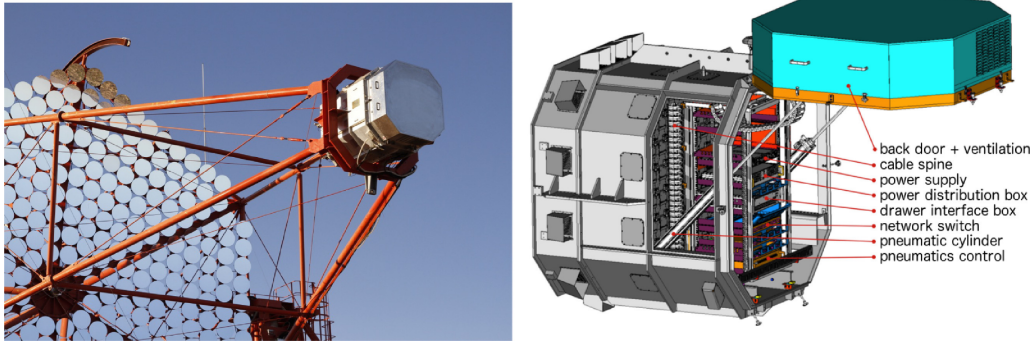


Figure 3.2.1: Left: The first upgraded H.E.S.S. I camera, on CT1. Right: Rear view of the camera, with open back door. Figure from [10].

3.1 Introduction

The first telescopes of the H.E.S.S. telescope array, CT1-4 were installed between 2002-2004 and are also referred to as the H.E.S.S. I array. They each have a 12-meter diameter and during the first phase of operation could detect photons with energies over $\sim 100\text{GeV}$. With the purpose of lowering that threshold down to $\sim 30\text{GeV}$, a fifth telescope, CT5, with a diameter of 28 meters was installed at the center of the H.E.S.S. I array in 2012. Its larger mirror area, higher quantum efficiency photosensors and lower camera dead-time allow it to trigger on lower energy events at a much higher rate (~ 10 times higher).

As a result of the introduction of the new telescope, the cameras of CT1-4 had to be updated, decreasing their readout dead-time (which was at $\sim 450\mu\text{s}$) in order to be able to also trigger at lower energies and record more events stereoscopically with CT5. Additionally, an upgrade was necessitated by the inevitable rise in malfunctions caused by the aging of electronics, connectors, and other crucial components that had endured the harsh conditions of the Namibian site for 14 years. Moreover, the cameras were becoming progressively more difficult to upkeep, as many electronic parts were becoming outdated and no longer available for purchase.

Thus, the readout scheme was replaced with a faster Ethernet-based readout system, using the NECTAR analogue chip (developed for the CTA Observatory) alongside more modern front-end boards. The design and performance of the new camera are described in [8] and [10].

3.2 Architecture of the HESS-IU Camera

The upgraded cameras consist of replaced electronic and mechanical parts, compared to the old H.E.S.S. I cameras. The only parts which were kept were the photomultiplier tubes and their bases which generate the high voltage. The majority of the cameras' development, production, and testing took place at the DESY site in Zeuthen. Figure 3.2.1 left displays an image of one of the upgraded cameras mounted on the telescope, while Figure 3.2.2 illustrates the electronics and mechanical subsystems inside the upgraded cameras and their interactions. In the following subsections, we will follow the path of the signal, from right to left.

3.2.1 Front-end electronics

The front-end of the camera, where the Cherenkov light from particle showers is detected and digitised, consists of 960 PMTs. These are organised in 60 "drawers" (Figure 3.2.3) in a 9×8 matrix with each corner missing 3 drawers. Each drawer consists of 16 PMT pixels in a 4×4 matrix, two analogue boards with 8 channels each and a slow-control board. The analogue boards (Fig. 3.2.4) contain the integrated circuits responsible for amplifying, discriminating and digitizing the PMT signals. The slow-control board, on the other hand contains an FPGA (Altera Cyclone IV) which controls the entire drawer, an ARM9-based single-board computer (TaskIt Stamp9G45), power regulators, and sockets for the PMT high voltage bases, as seen in Figure 3.2.3 left. The front-end of the camera is separated from the back-end by a mechanical structure

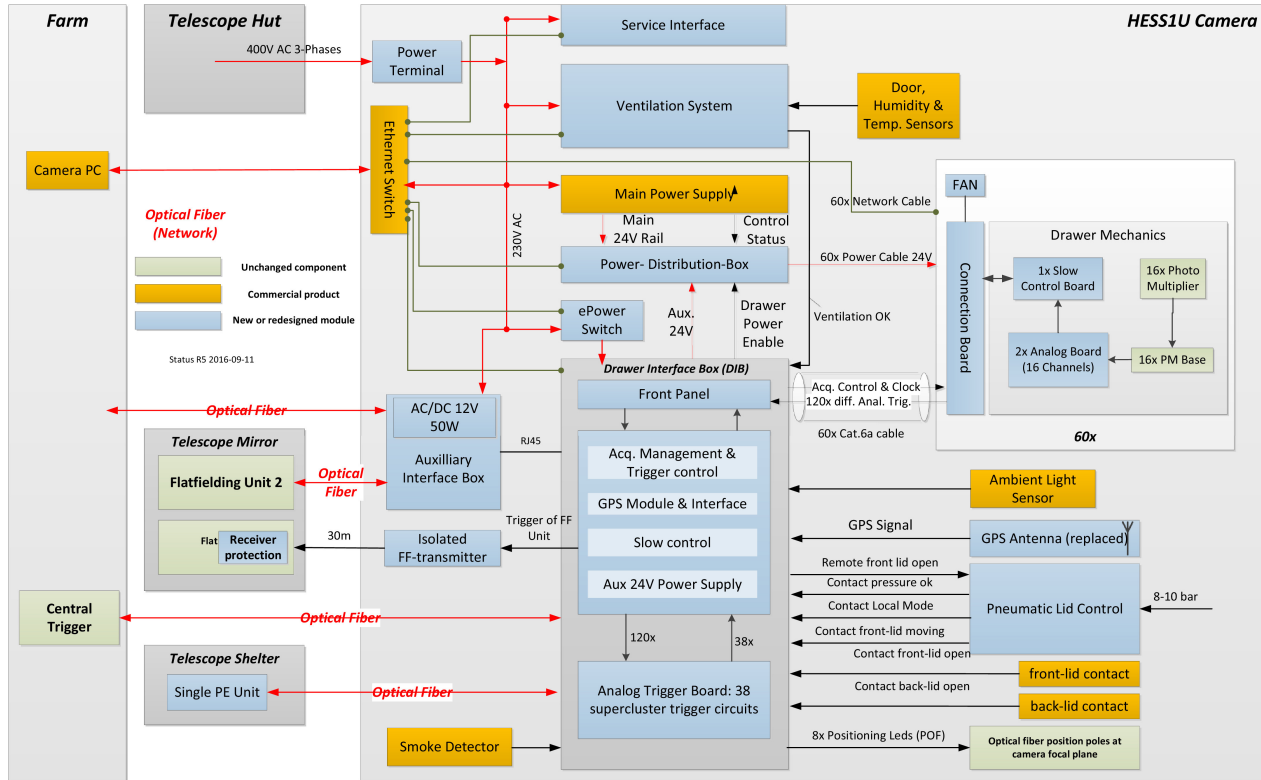


Figure 3.2.2: Illustration of the H.E.S.S. I Upgrade architecture. Green-colored lines indicate original components, blue-colored lines represent commercial custom-made components, and orange-colored lines denote commercially available off-the-shelf components. The red lines correspond to power distribution, and the arrows indicate the direction of power flow. If labeled as "Optical Fiber," the arrows represent bidirectional optical fiber links. Additionally, green lines with circle terminations signify copper Ethernet links, and black lines with arrows represent electrical signals. To mark the physical locations of subsystems, light grey boxes are used: "HESS1U Camera" refers to the camera body, the "Telescope Shelter" represents the camera daytime parking shelter, the "Telescope Hut" is a service container linked to the telescope structure, and the "Farm" denotes the server room within the array control building. Figure from [10].

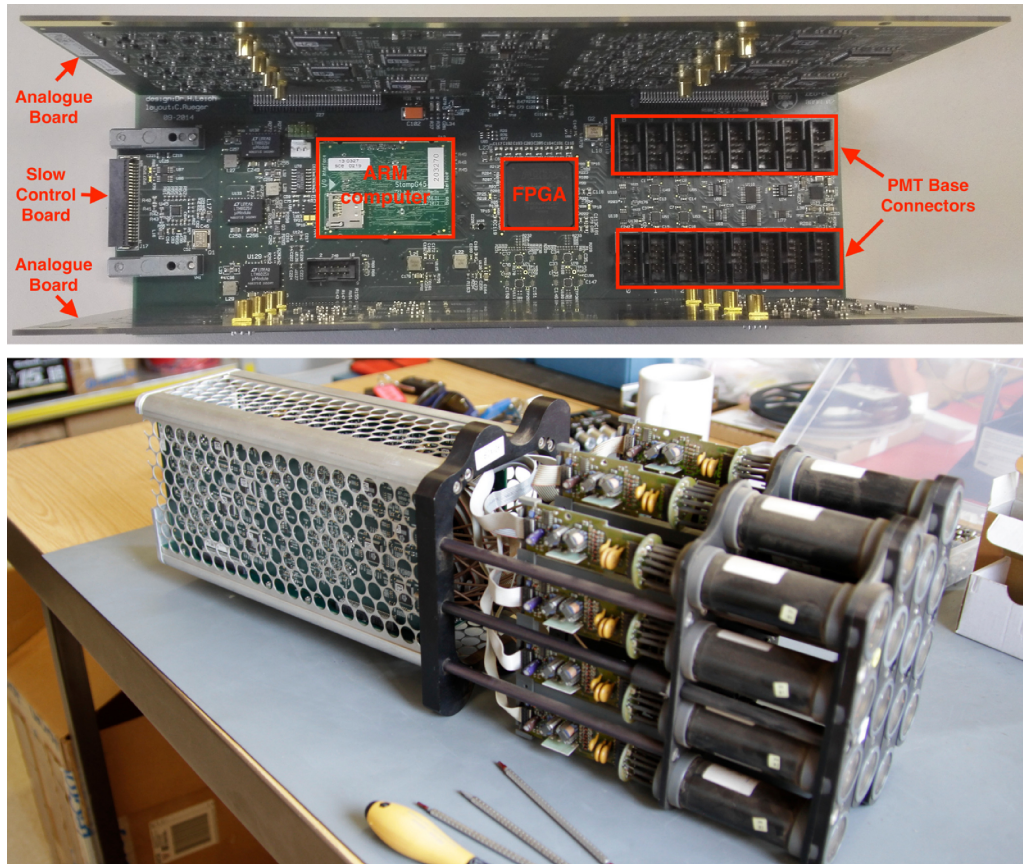


Figure 3.2.3: Top: Partially assembled drawer and important components. Bottom: Fully assembled drawer. From [10].

which supports the above drawers. The connection board at the back of this structure hosts network, trigger and power sockets (Fig. 3.2.5). The front-end electronics are discussed with more detail below:

Analogue Boards

The analogue signal detected from the PMTs is sent to the analogue boards via 15 cm long coaxial cables, in the form of short negative polarity, single-ended 2-3 ns FWHM pulses. Their amplitude is within the range $1\text{mV} - \sim 1\text{V}$, depending on the amount of detected photons. After reaching the board, they are AC coupled, pre-amplified by 9.8, divided into three branches, and amplified by low noise single-ended to differential amplifiers, where their polarity is also inverted.

Consequently, the NECTAR chip (discussed below) receives two of the three branches for sampling and digitization, with amplification factors for two channels, high gain (HG) and low gain (LG), which are equal to 15.1 and 0.68 respectively. For the purpose of minimising its effect on the LG signals, the HG signals are clipped to 3.3 V, which lies within the chip's tolerance rate as its nominal input voltage is in the 2 V range. To ensure that the signal remains within the input range even in the case of undershoot, a constant pedestal offset of around 0.2 V (~ 420 ADC counts) is added to it. It is then sent to a NECTAR chip for readout.

Meanwhile, in the third branch, the signal undergoes amplification by a factor of 45 and is routed to a high-speed comparator. The comparator's digital output is then directly sent to the slow-control board's FPGA, where it is referred to as the level 0 (L0) trigger signal.

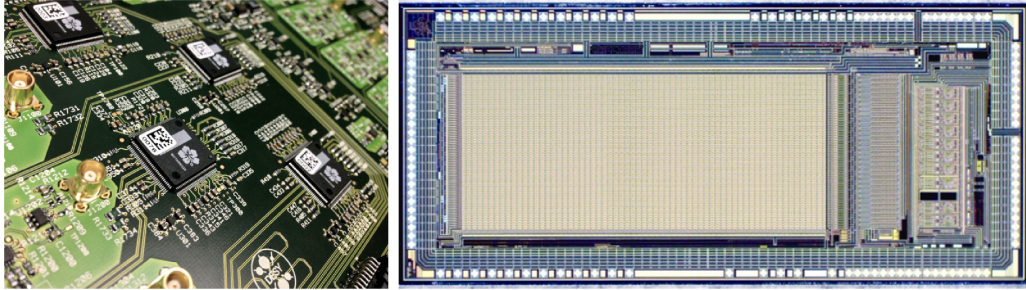


Figure 3.2.4: Left: Partial view of an analogue board. The signal amplification components are marked with light green, while the NECTAR chips appear in black colour. Right: detailed view of the NECTAR chip. From [10].

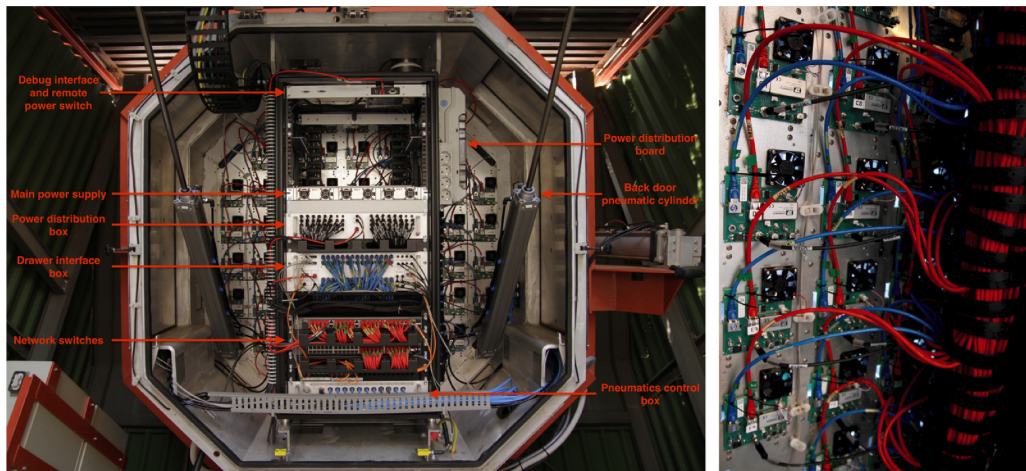


Figure 3.2.5: Left: rear view of the inside of HESS-IU. Right: Camera cabling; the Ethernet cables are red, the trigger and clock cables are blue, while the power cables are black. All of the above are connected to the drawer connection boards. From [10].

Readout

The readout is performed using the analogue memory NECTAr chip (Figure 3.2.4 right), designed by CEA/IRFU in France for the CTA Observatory [42]. This is the component mostly responsible for the improved performance of HESS-IU. It has a channel for each gain (LG, HG), which hosts a 1024 cell capacitor array that functions as an analogue ring memory buffer. The chip has two functions; during the writing phase, the input signal amplitude is stored on the capacitor array with a switching frequency of 1 GHz. The amplitude values are written circularly on the buffer, meaning that they are overwritten every 1024 ns. The writing process stops when the NECTAr chip receives a trigger signal, initiating the reading phase. During the reading process, the values of a small region of interest (ROI) of the cells are read out and digitised by the 12-bit 21 Msamples/s analogue to digital converter (ADC) hosted on the chip, and the resulting digital signal is directed to the FPGA through a serializer. For regular observations, the ROI presently corresponds to 16 cells (16 ns). These values are summed by the FPGA and then transmitted to the camera server as an integrated value per pixel per gain. The 16 ns ROI is chosen for compatibility with H.E.S.S. analyses and frameworks, and is an acceptable time window, as typical air showers reaching the camera last less than 10 ns. Though, the width of the ROI can be modified to higher values, up to 48 ns, increasing the camera's sensitivity to lower energy showers.

Slow control and connection boards

The slow control board hosts the FPGA and the ARM computer of each drawer. The FPGA directly controls all the electronics inside the drawer and is used to read out the PMT sampling data coming from the NECTAr chip, while also collecting monitoring information such as as PMT currents and L0 trigger counters. The FPGA is connected to the ARM computer via a 100 Mbit/s memory bus, utilizing a 16-bit word width. The latter reads out all the FPGA data and sends them to the central camera server through its 100 Mbit/s Ethernet interface via TCP/IP, using the ØMQ library. The central camera server is responsible for controlling the drawer via remote procedure calls, using the Apache Thrift library.

There are also several point-of-load regulators and DC line filters located on the slow control board, in order to provide the necessary voltage for the proper function of the drawer's electronic component. The front-facing end of the board hosts the sockets for the PMT HV bases along with the corresponding control and readout electronics.

3.2.2 Back-end electronics

The back-end electronics are hosted at the 19-inch rack at the back of the camera, as seen in Figure 3.2.5. The different components are mentioned below:

Drawer interface box

The drawer interface box (DIB), seen in Fig. 3.2.6 acts as the central hub of the camera. It supports various functions, like managing the trigger and readout control interface, distributing clocks to the drawers, generating camera-level triggers, managing the interface for the array central trigger and auxiliary camera components such as front position LEDs, pneumatics control, the ambient light sensor, GPS timestamping and a safety interlock logic, for the protection of people and electronics.

The DIB consists of three boards: the front panel board, which hosts drawer trigger connectors, clock and control signals, the interface for the central trigger fiber, the front position LEDs lightguides and as well as all the other sensors and actuators of the camera; the main board, which houses the the FPGA and ARM computer and to which all signals sent from the other components are directed; lastly, the analogue board where the level-1 (L1) camera trigger is produced.

Another component of the DIB is a GPS module, with two different uses: it generates a pulse-per-second (PPS) signal, which is used to discipline the main 10 MHz clock, which is then distributed to the drawers; at the same time it uses a serial interface to send a timestamp to the DIB, making timestamping of individual camera events possible with a precision of the order of a few μs (the time of camera - central trigger communication).

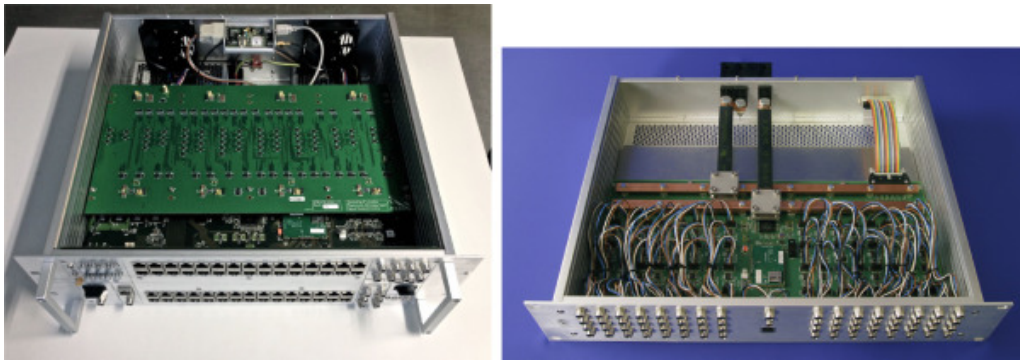


Figure 3.2.6: Left: Drawer interface box with open top lid, showing the analogue board, which is on top of the main and front panel boards, while the GPS module is located at the back. Right: Power distribution box. From [10].

Camera trigger and array trigger

The camera trigger follows an N-fold architecture over 38 sectors of 64 PMT pixels, with N usually set to 3. This means that a N-fold coincidence of pixels within a sector will cause the triggering of the camera. The 38 trigger sectors of the camera are arranged geometrically in such way that they overlap vertically by one full drawer and horizontally by half a drawer. The camera trigger architecture is implemented in the following manner: the PMT signal arriving at the analogue board undergoes amplification and comparison with a threshold P (currently equivalent to around 5.5 p.e.) to generate the L0 signal. This signal is sent to the slow control board's FPGA, where it is sampled with an 800 MHz sampling rate, which means that the sampled signal can be stretched out in time or delayed with a rate of 1.25 ns. Afterwards, the FPGA calculates the number of pixels with a live L0 signal in each half of the drawer separately and constantly sends the two values to the DIB as Low Voltage Differential Signaling (LVDS) pulse-amplitude modulated (with 8 discrete levels of 33 mV) trigger signals.

In the DIB, the LVDS signals are transformed into single-ended signals, which in turn are isochronically transmitted to 38 analogue summatoms, each corresponding to a different sector. The overlapping geometry of the trigger sector means that each signal can be sent to up to 4 different sectors. The summed signal of each sector is then sent to the drawer's FPGA, where it is compared with a threshold Q, corresponding to a number N of active pixels. The comparator outputs are then directed to the DIB's FPGA, which combines them with an OR operation, producing the L1 trigger. Whenever there is an active L1 signal, the DIB broadcasts a length-encoded "stop" signal to all the drawers via the LVDS control lines, which leads to the drawer FPGA stopping the NECTAR chip writing phase and initiating the reading phase, where the values in the ROI around the trigger position get read out, digitised and stored in a front-end buffer. At the same time with the "stop" signal, an "active" signal is transmitted via optical fibre to the central array trigger, located in the control building.

During standard H.E.S.S. observations, the central array trigger sends an "accept" signal back to the cameras of CT1-4 only in case of coincidence of at least 2 telescopes with "active" signals within an 80 ns time window, which starts after correction for their pointing-dependent light propagation delay. Once the DIB of each camera receives the "accept" signal, it broadcasts it to the drawers, which then start storing the front-end buffer data. If an "accept" signal does not arrive within a time period t_b , which is slightly longer than the readout dead-time and the maximum central trigger response latency, the front-end buffer data is discarded. In case the camera transmits another L1 signal during this hold-off time, the DIB sends a "busy" signal to the central array trigger, without sending a signal to the drawers. The signals "active", "accepted" and "busy" are pulse-length coded in order to be distinguishable, as they are transmitted through the same optical fibre connection.

The synchronous nature of the H.E.S.S. camera trigger allows the implementation of some alternative L1 trigger logic architectures only by modifying the FPGA firmware, such as a compact nearest neighbor (NN) logic and a pseudo-analogue sum trigger logic. According to the first logic, the DIB issues an L1 signal only if there is cluster of neighbouring pixels active at the same time. For this purpose, the FPGA uses a

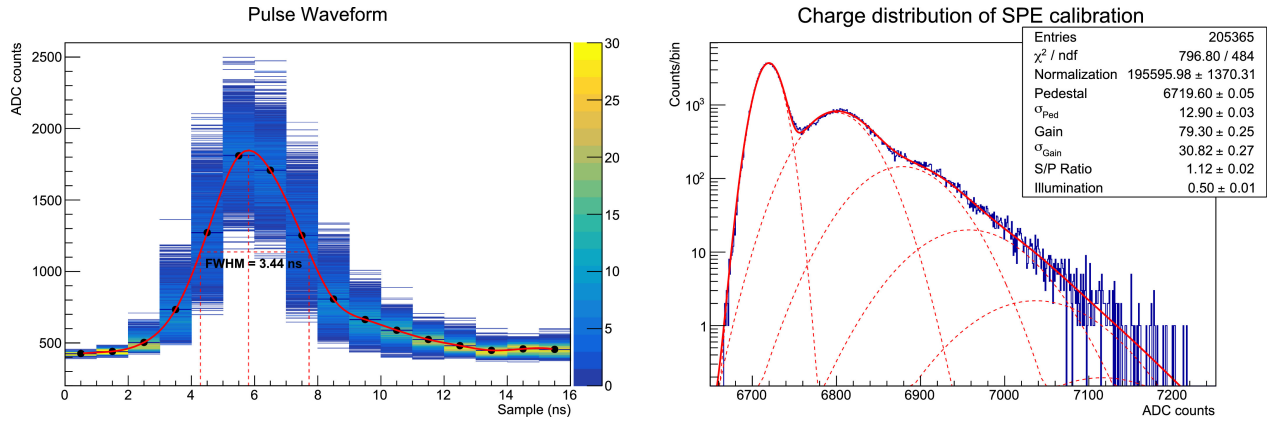


Figure 3.2.7: Left: Digitised PMT pulse from a flat-field run, showing the distribution of around 2000 light pulses. The red line corresponds to a spline interpolation of the mean value for every sample, with the FWHM shown with dashed lines. Right: Charge distribution from an SPE run, fitted to a linear combination of Gaussians. From [10].

look-up table to confirm whether the pixels are neighbouring. On the other hand, the pseudo-analogue sum algorithm operates by measuring the duration of the L0 trigger signals, instead of only counting the number of pixels with active L0 signals. The underlying concept is that above a certain threshold, the length of a PMT pulse is proportional to its charge, as PMT pulses can be considered roughly triangular (for example see Figure 3.2.7). The FPGA conducts the measurement of the duration of the L0 signals for each half-drawer separately in a 5 ns window and quantizes it in 1.25 ns steps, to ensure that each signal has at most 4 counts, preventing PMT after-pulsing issues similar to amplitude-clipping. The FPGA then sends the sum of the above durations to the analogue trigger board, causing the output of every summator to be proportional to the total charge deposited within the relevant sector.

Ventilation, pneumatic and power systems, cabling

The camera's ventilation system, consisting of a 250 mm Helios KVW 250/4/50/30 centrifugal fan, two filters in series (coarse and fine) and a 6 kW air heater, ensures an airflow of $\sim 360\text{l/s}$ from the back to the front of the camera, filtered to minimise dust. An air heater is used to prevent condensation and to maintain the drawer temperature at $\sim 32^\circ\text{C}$ with a gradient of $\pm 5^\circ\text{C}$ along the top-bottom direction. Additionally, the pneumatic system employs two cylinders for the back door, one cylinder and five clamps for the front lid, so that they can open and close with condensed air, as well as monitoring sensors. The camera is powered by standard industrial 400 V three-phase AC mains, while the drawer 24V DC is produced by a front-end power supply and distributed using a custom-built Power Distribution Box (PDB). Lastly, M8 connectors for power distribution along with standard Ethernet and electrical cables are used for cabling, with Ethernet used for data transmission and electrical cables for the connection of auxiliary sensors and actuators, with the exception of the GPS antenna which uses a coaxial cable with an SMA connector.

3.2.3 Sensors and calibration devices

Inside and outside the camera, numerous sensors are used to monitor temperature, humidity, door position, ambient light and smoke presence. These sensors send their signal to a safety interlock system, implemented in the DIB FPGA, to protect people and hardware.

Meanwhile, there are two calibration devices: the single photoelectron unit and the flat-fielding unit. The single photoelectron (SPE) unit is used to adjust the gain of the individual PMTs and is positioned in the shelter, facing the front of the camera, and thus used only when the telescope is fully parked. It employs an LED to emit blue light pulses (with a wavelength of 370 nm) with pulse frequencies between 38 Hz and 156 kHz. The pulses have a duration less than a nanosecond and a variable intensity of ~ 0.1 to ~ 200 photoelectrons. A plastic diffuser in front of the SPE unit is deployed to guarantee complete camera illumination, with a uniformity of around 50%. The camera server controls the intensity and duration of the pulses via

UDP, while an adapter board on the SPE unit sends its trigger signal, which is synchronous to the light pulses, to the camera via optical fibre connection.

The flat-fielding (FF) unit is employed to calibrate the pixel-wise light collection efficiencies of the PMT photo-cathode and funnels. Positioned at the centre of the telescope mirror dish, it also features an LED which emits short (< 3 ns FWHM), blue (390–420 nm) light pulses of fixed intensity (~ 100 p.e. at the PMTs) in contrast to the SPE unit. A holographic high quality diffuser placed in front of the FF unit, as well as the small angle subtended by the camera, ensure uniform illumination, causing the stability of the flat-fielding intensity and its non-uniformity throughout the camera to be less than 5% RMS.

3.2.4 Camera network and software

All major components (drawers, DIB, PDB, and ventilation system) in the camera are connected by 100 Mbit/s Ethernet links using two 48-port switches inside the camera. The camera server, a commercial 1-unit rack server with a 4-core Intel Xeon E3-1246v3 processor clocked at 3.5 GHz and 16 GB of DDR3 RAM housed in the "farm" connects to the cameras via a 10 Gbit/s optical fibre connection. The internal camera network has a star-like topology, where each device of the network operates independently from other devices and they can be accessed only through the central camera server. Only the central server can issue slow-control commands, while at the same time acting as the endpoint of the monitoring, logging and event data streams. This distributed scheme enhances the camera's flexibility and resilience, preventing data loss with the use of separate memory blocks in the ARM computer to buffer the data for each module.

Regarding the camera software, it was also developed with a distributed, multi-architecture nature to fit the HESS-IU camera design. It includes event acquisition and slow control functions, text-based and web-based user interfaces, extensive unit and integration tests, validation routines for mass production, as well as a comprehensive commissioning and calibration suite used for taking runs, analyzing them and adjusting camera parameters independently of the main H.E.S.S. data acquisition system. The 100,000 lines long codebase is mostly (82%) written in C++, along with smaller portions of ANSI-C and Python (11% and 7% respectively).

Aiming to enhance the codebase's extensibility, maintainability and efficiency, the code was developed using well-tested open-source solutions. Both ARM and x86_64 architectures came from a single source tree, while the CMake build system was used for cross-compilation. The ARM computers run the Yocto embedded Linux OS, utilising a custom-built DMA-enabled driver for FPGA communication. At the same time, camera control uses the Apache Thrift library, along with the H.E.S.S. data acquisition software using the CORBA protocol. Data transfer is achieved with the help of the ØMQ smart socket library, while a custom raw data serialization protocol, optimized for speed, is utilised. Finally, monitoring and logging, are achieved with the Google Protocol Buffers library.

3.3 Camera calibration

To accomplish deduction of air shower images using the raw PMT data, we need to calibrate the PMTs and their electronic response. Below, based on [9] and [10], we describe the methods and parameters used for this purpose.

3.3.1 Readout

As mentioned in the previous section, readout is accomplished through the NECTAr chip. For this reason, parameters regarding readout line correction and the ROI need to be adjusted regularly.

NECTAr line correction

The 1024 cell analogue memory buffer of the NECTAr chip consists of capacitors placed in a 16×64 matrix, where each of the 16 lines has its own input buffer and readout amplifier. Thus, there is a constant dispersion of the DC baselines between the NECTAr lines, which is balanced by adding an offset to the DC lines, via 16 integrated digital to analogue converters (DACs). The DAC values are calibrated by performing sample-wise pedestal runs of at least 16 samples, where we determine the average difference between the sample baselines

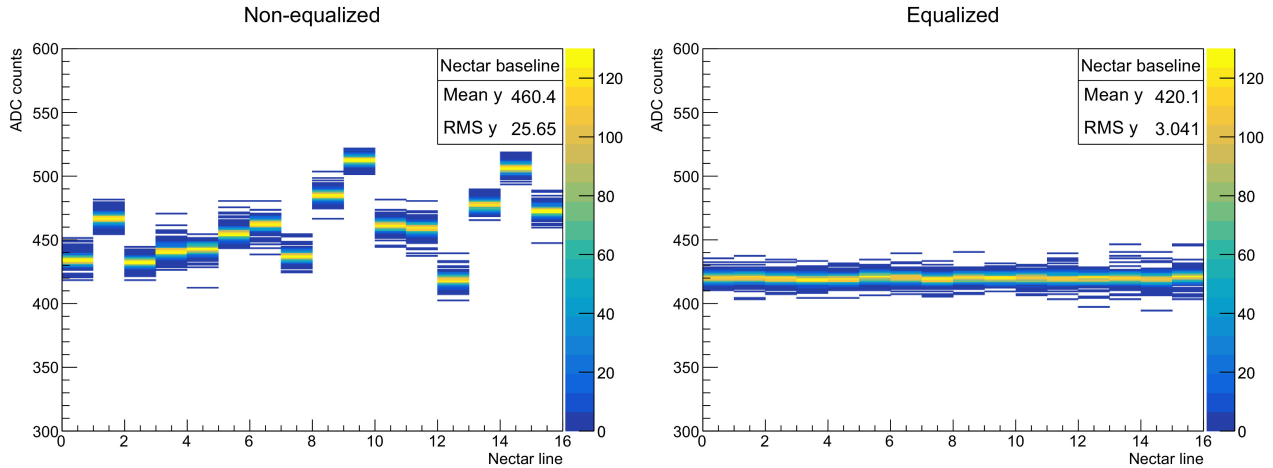


Figure 3.3.1: Left: Sample baseline of NECTAR capacitor array line before calibration. Right: Baseline after 5 iterations of calibration process. There is an evident decrease in the baseline RMS value. From [10].

and a reference value of 420 ADC counts (equal to around 0.1 of the dynamic range, to enable the detection of pulse undershoots). The DAC conversion factor of each line can then be adjusted in order to make up for this difference. This procedure is repeated multiple times, so that the pedestal of each sample approximates the default baseline value. One example of this process can be seen in Figure 3.3.1. The position of the baseline in each pixel is referred to as the pedestal value.

The above procedure is repeated roughly two times a year for the whole camera, whenever a drawer is replaced or the PMT gain is readjusted and the DAC conversion factors are stored in a MySQL database. Though, the baseline correction is not necessarily needed for regular observations, as the measured quantity is the charge integrated over 16 samples and the pedestal, which is the same for each sample, is removed. This is due to the ROI being a multiple of the line dispersion period, effectively cancelling out any event-wise shift of the baseline.

Readout window positioning

Until the L1 trigger signal arrives, the NECTAR chips will store analogue signal cyclical buffers. As soon as the triggering happens, the cells which will be read out will be inside the readout window. Therefore, it is necessary for the readout window to be placed at the region which maximises the charge of the Cherenkov pulse. The readout window adjustment needs to be done separately both for the SPE unit and the camera L1 trigger. When the NECTAR chip receives the L1 signal, the readout window will be positioned L cells before the last one which was sampled. Thus, in order to read the correct cells, it is essential to measure the trigger latency L for each chip and trigger source. This is done by illuminating the camera with a reference light pulse of high intensity (~ 100 p.e. produced either by the SPE unit, for SPE readout window repositioning, or by the FF unit in case of L1 readout window adjustment), while simultaneously varying the value stored in the chip's register N_d , which controls the start of the readout window, until the sampled pulse is at the centre of the readout window. Since the buffer is cyclical, N_d is the complementary of L over the 1024 cells of the buffer, meaning $N_d = 1024 - L$.

3.3.2 Pixel calibration parameters

The reconstructed air shower images used for Cherenkov analysis are derived from the amplitude measured in each individual PMT pixel. This amplitude is measured in the form of charge produced by the Cherenkov light in photoelectrons, normalised using the efficiency of the specific pixel in relation to the camera's mean value. This normalisation factor is referred to as the flat-field coefficient. Converting the amplitude to p.e. is achieved by determining the conversion factor (gain) between ADC counts and p.e. for each pixel.

Initially, amplitudes before correction are derived from the integral in ADC counts over the samples of the raw PMT data in the region of interest, separately for the high and low gain channels. This amplitude is

converted from ADC counts to p.e. according to the following equations, for the high gain and low gain channels respectively:

$$A^{HG} = \frac{ADC^{HG} - p^{HG}}{\gamma_e^{ADC}} \times FF \quad (3.3.1)$$

$$A^{LG} = \frac{ADC^{LG} - p^{LG}}{\gamma_e^{ADC}} \times \left(\frac{HG}{LG}\right) \times FF \quad (3.3.2)$$

where $ADC^i, i = HG, LG$ are the measured amplitudes in ADC counts, $p^i, i = HG, LG$ are the pedestal (baseline) positions for each channel, γ_e^{ADC} is the gain of the PMT high gain channel in (ADC counts / p.e), (HG/LG) is the amplification ratio between the two channels and FF is the flat-field coefficient.

The final pixel amplitude is provided by either the high gain or the low gain channel for low and high values respectively, or by a combination of both for intermediate values. More specifically, A^{HG} is used for up to ~ 150 p.e., A^{LG} is used for over ~ 200 p.e., while for values in the range 150-200 p.e., a weighted average is used, giving the final amplitude:

$$A = (1 - \epsilon) \times ADC^{HG} + \epsilon \times ADC^{LG} \quad (3.3.3)$$

where $\epsilon = \frac{ADC^{HG} - 150}{200 - 150}$.

All in all, the amplitudes measured in ADC counts for the two channels can be easily converted to p.e. given the values of the pedestal positions for the two channels, the gain γ_e^{ADC} of the high gain channel and the flat-field coefficient of the relevant pixel. The calibration uses different methods to provide all of the above values. Finally, the calibration process ensures the detection of faulty pixels, so that their measurements are not taken into account.

Determining the PMT gain

Calibration using the SPE unit is performed in order to determine the individual PMT gain, meaning the conversion factor γ_e^{ADC} between ADC counts and voltage. This is possible by doing some special SPE runs, where we vary the voltage of each PMT and illuminate it with light pulses from the SPE unit of very low intensity, such that the average amount of photons detected is less than 1. The charge distribution from an SPE calibration run can be seen in Figure 3.2.7, right, where the charge is integrated over the 16 samples of 1 ns of the readout window. This charge distribution can be modelled by a linear combination of Gaussian functions (this will be discussed more in Chapter 4). Though, despite this fit being quite robust for PMT illuminations of 0.1-0.3 p.e., it is biased, as the actual charge distribution is assymetric and skewed towards lower values. This means that the average single photoelectron amplitude is less than the amplitude at the peak of the Gaussian distribution ([43]), which is subsequently corrected in the analysis by a factor of 0.855.

This type of calibration is performed roughly every 6 months, to minimise the effects of the PMT performance degrading over time. In order to achieve a more precise gain, the procedure is reiterated several times, each with a finer voltage step. The conversion factor between ADC counts and p.e. is currently equal to ~ 60 per p.e.. In order to achieve this constant conversion factor, the voltage applied to the PMT needs to be increased or decreased accordingly, based on at which voltage variation we achieve this γ_e^{ADC} . Finally, after the calibration, the ROI needs to be re-positioned, as the PMT transit time depends on the applied voltage.

Flat-field coefficients

In order to estimate correctly the Cherenkov light arriving in each pixel, it is necessary to calibrate the differences in the light collection efficiency between the pixels of the camera. This calibration is done by illuminating the pixels homogenously with fixed intensity pulses from the flat-fielding unit. The FF coefficient for each pixel i will then be equal to the average charge \bar{Q} recorded by all the camera over the charge Q_i recorded by the specific pixel: $FF_i = \bar{Q}/Q_i$. This is done separately for the two channels. Flat-field calibration is also used in calibrating the time of the peak amount of information of each pixel (under the assumption that the pulses arrive isochronically at all pixels), as will be discussed more in detail in Chapter

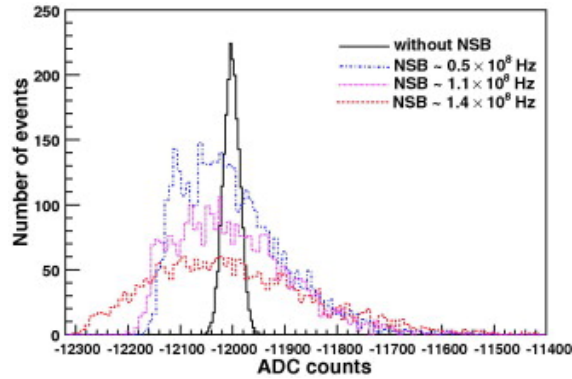


Figure 3.3.2: Impact of night sky background on pedestal width. From [9]

4. This process is performed several times per lunar month and the FF coefficients are each time averaged and stored in a MySQL database.

Estimation of pedestals and night-sky background

The pedestal position corresponds to the mean ADC count position detected under the absence of Cherenkov light.

In the dark, a narrow Gaussian distribution around the pedestal value is created by the electronic noise of the hardware. This distribution is not fixed at the baseline value, but it is also dependent on the camera temperature, which can be anywhere between 20 and 40°C, depending on the time of the year. During a single run, the temperature variation is usually 1°C, changing the pedestal position and making it necessary to calculate the pedestals separately for as short as possible time slices during the run, in order to minimise the effect of them changing position due to different temperatures in the electronics. The pedestal position $p_i, i = HG, LG$ corresponding to electronic noise can be found by measuring the ADC distributions for the two channels when the camera lids are closed.

During observations, where the camera lid is open, the pedestal width is significantly increased by night sky background (NSB), which can be seen in Figure 3.3.2. The contribution of NSB photons in the PMT charge signal is typically over 1 p.e. Though, NSB has a negligible effect on the pedestal position, as it depends only on the electronic noise. This means that the pedestal position corresponds to the number of ADC counts measured in the absence of any Cherenkov light.

It is important to correctly estimate the NSB rate in each pixel, as pixels noticeably influenced by background light, i.e. by a star in their field of view, might not give reliable results in the analysis. Therefore, they would need to be excluded. The NSB rate can be measured with two different methods: from the pedestal width as mentioned before or from the PMT currents, which in the presence of NSB shift from their dark values.

3.3.3 Trigger

In subsection 3.2.2, we described the triggering process. It is evident that it requires many parameters which need to be calibrated in order to have an efficient trigger. The most essential ones are the pixel and sector thresholds, P and Q respectively, and the pixel L0 delay d .

To calibrate the pixel threshold P , it is necessary to determine the relationship between its set value (in ADC counts or mV) and its effective value in p.e. For this purpose, special calibration runs using the SPE unit are taken, as it can provide variable-intensity light pulses. During these calibration runs, the camera is flashed with a fixed frequency f and a variable intensity I , ranging from ~ 5 to ~ 50 p.e. The pulse intensity in each pixel is measured by the mean of its charge distribution, which is divided by the relative PMT gain coefficient. The threshold P is varied during the run, and for each intensity I , the values of L0 pixel trigger efficiencies (ratio between pixel trigger rate and frequency f) are measured, resulting in a sigmoid graph, as seen in Figure 3.3.3, left. The midpoint of this graph corresponds to the threshold P needed to discriminate

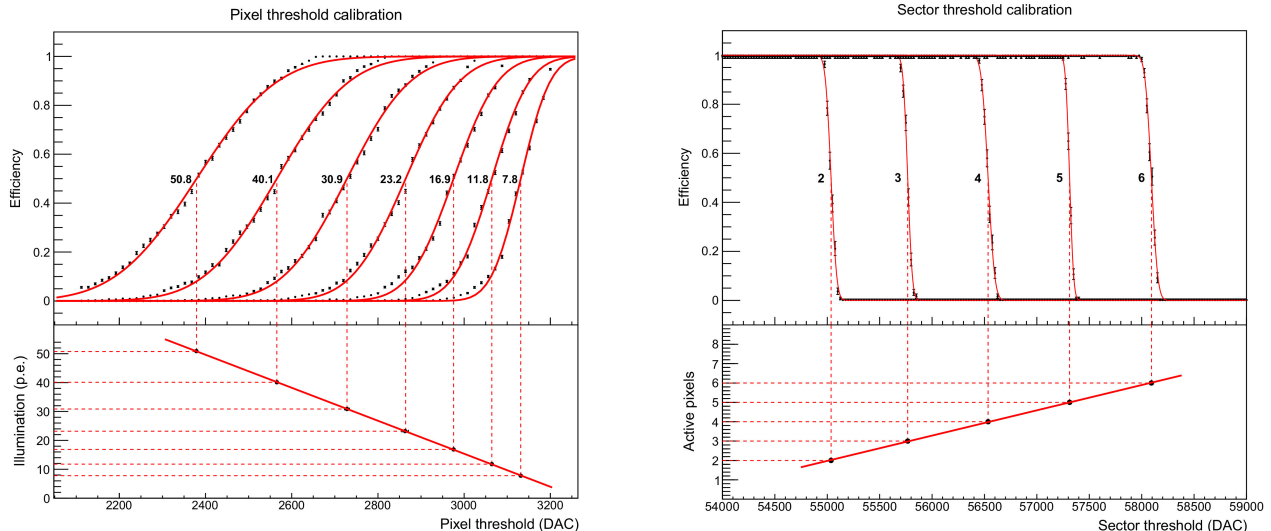


Figure 3.3.3: Sigmoid curves of pixel (left) and sector (right) trigger efficiency, for different thresholds P and Q . Thresholds are given in DAC counts (0.76 mV/count). The lower insets show the linear relationship between sigmoid centers and illumination (in p.e.) and active pixels respectively. From [10].

I photoelectrons. It is evident from the graph that the relationship between I and P is linear. This process is repeated several times, making it possible to determine the constants m and b in the linear dependency $P(I) = mI + b$, and as a result the value of P in p.e.

The calibration of the sector threshold Q is done using the flat-fielding unit, but in a similar manner to the pixel threshold calibration. More specifically, Q is varied during the flat-fielding runs, each for a different number N of active pixels per sector, during which the camera is flashed with a fixed frequency f . This time, for the different N , the sector trigger efficiencies (ratio between measured sector trigger rate and f) are measured in relation to Q . The resulting graphs (Fig. 3.3.3 right), are again sigmoid and their midpoints correspond to the values of Q for the given N . N is discrete, leading to steeper curves than in the previous case. Again, this process is repeated several times for different values of N , making it possible to determine Q as a linear function of N , $Q(N)$. Ultimately, for the designated efficiency of 3, Q is calibrated so that all sectors exhibit 100% efficiency for $N = 3$ and 0% efficiency for $N = 2$.

Moreover, the pixel L0 delays d are calibrated using a modified FPGA firmware, which sends the sampled L0 information of all pixels on the data stream, while all the pixels are illuminated simultaneously by the flat-fielding unit. The delays d are then adjusted so that the rising edges of all L0 trigger signals are aligned.

Lastly, the operating point of P is determined after all of the above calibrations are done. To do so, the value of P is varied and the different L1 and coincidence trigger rates are measured during a regular observation run. This run is performed using the whole array (including CT5) under optimal observation conditions and results in "bias curves" for CT1-4, which can be seen in Figure 3.3.4. The steep fall in coincidence rate after 5 p.e. is due to night sky background noise, while the flatter part for higher values of P is caused by air showers. Both parts can be fit by two exponential functions, and the value of P is chosen so that coincident events caused by noise are less than 1% of all triggers. This value is currently set at 5.5 p.e. for regular camera observations, ensuring stable operation even for higher frequencies of NSB events (up to ~ 250 MHz photon rate).

Finally, at the array level, it is essential to calculate the round-trip time of the signal between the array central trigger from the camera server and the camera. This is necessary for fine-tuning the fixed part of the central trigger coincidence delays, which exhibit variability depending on the pointing direction. For this purpose, the signal is sent from the central trigger via optical fiber to the DIB, which then responds to it. The time difference between transmission of the initial signal and reception of the response is measured for each camera using an oscilloscope. Consequently, the central trigger delays can be adjusted, so that all the trigger messages coincide in time.

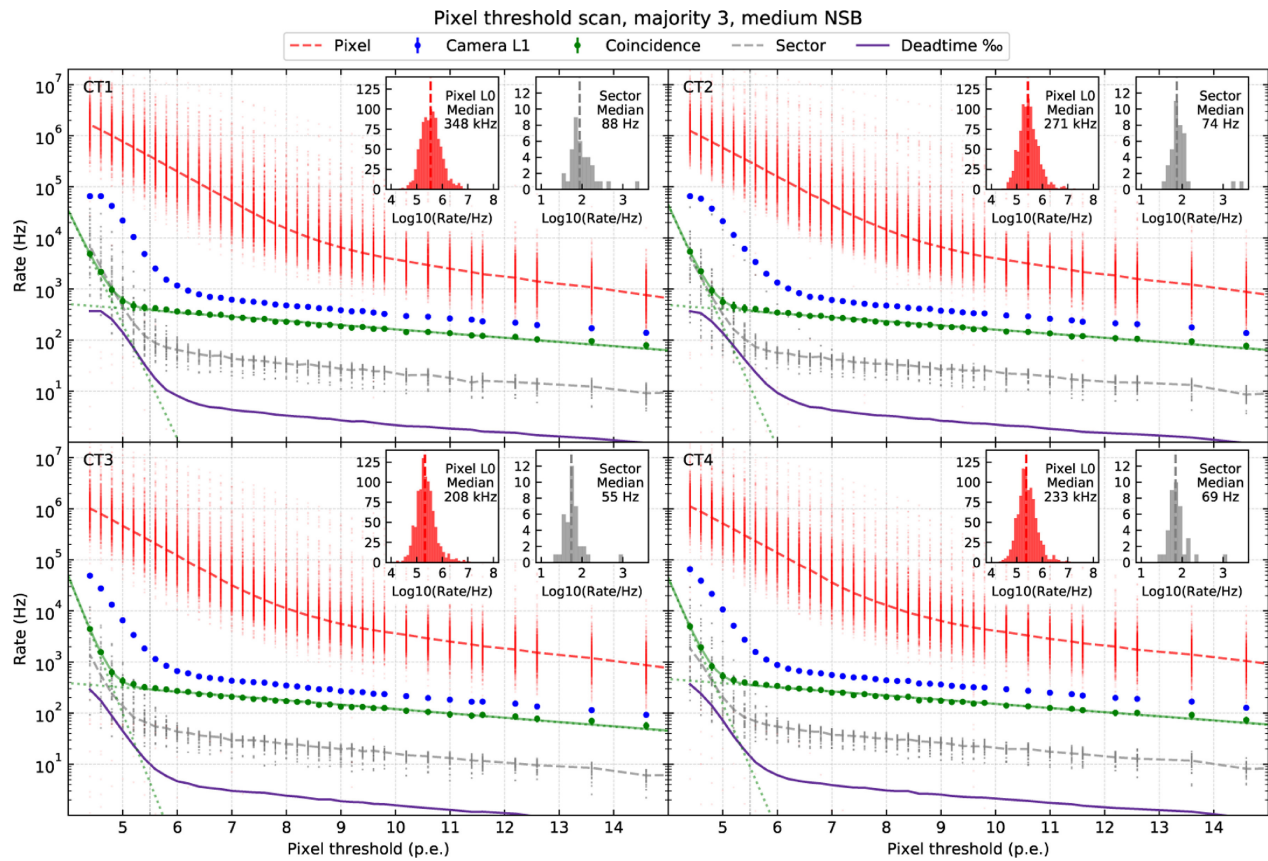


Figure 3.3.4: Results of a threshold scan during a Galactic source observation under regular NSB, showing trigger rate versus pixel threshold in photo-electrons. From [10].

Chapter 4

Improving the HESS-IU Calibration

4.1	Introduction	84
4.2	Flat Field calibration and readout window adjustment	84
4.2.1	Flat Field calibration	84
4.2.2	Global fit vs local fit	84
4.2.3	Readout window adjustment taking into account the intensity of the FF LED	85
4.2.4	Results	91
4.3	Adjusting Single Photoelectron gain calibration with a global fit	91
4.3.1	Converting ADC counts to photoelectrons	92
4.3.2	Model of the photomultiplier response	92
4.3.3	SPE Calibration	93
4.3.4	Another global fit, assuming linear gain	93
4.3.5	Results and comparison to standard algorithm	95

4.1 Introduction

In chapter 3, we discussed about the HESS-IU camera, its architecture and the various calibration techniques. In this chapter, we propose two improvements in the calibration: a new method for readout window adjustment taking into account the intensity of the flat-fielding LED, and PMT gain calibration using a global fitting method. Most of the analysis was done in python3, using the DESY grid system and HTCondor.

4.2 Flat Field calibration and readout window adjustment

4.2.1 Flat Field calibration

One of the main calibration methods of the HESS-IU Camera is flat-field (FF) calibration. As the hardware is not ideal and slowly degrades with time, different pixels may have different responses to uniform lighting[9]. In order to correct this, a different flat-field coefficient is determined for each pixel. The amplitude for each signal received by a pixel is then multiplied by its flat-field coefficient, so that its value in photoelectrons is calculated. Another difference in response to uniform lighting can be related to the timing of the readout window, as some pixels might record a light pulse later in their readout window than others.

There are specific flat-field (FF) runs performed roughly every two days. During these runs, a device called flat-fielding unit is used and is located at the center of the telescope mirror dish, 15 m from the camera. The special FF runs use LED flashers which emit short (< 3 ns FWHM) blue (390–420 nm) light pulses of fixed intensity (~ 100 p.e.– photoelectrons)[10]. The process is repeated multiple times over the course of a few minutes, in order to have an accurate distribution of the incident photons on the camera for each moment in the duration of a pulse, as the detected photons can either be originated from the FF unit or from night sky background noise. The utilisation of a holographic diffuser in front of the camera, as well as the insignificant angle between the camera and the FF unit, ensure that the illumination is uniform, with the non-uniformity below 5% RMS.

For each telescope camera, the flat-field coefficients are determined by the following process: the mean signal of the camera is calculated using the values of all pixels (excluding those which do not work properly), the ratio of every sample of the signal of each pixel in relation to the relevant sample of mean signal is placed in a histogram, from which the mean is derived. The FF coefficient for this pixel is equal to the inverse of this mean value. The coefficient will then be used to multiply the signal in p.e. from observations to assure uniformity.

Apart from determining the FF coefficients, these runs are also used to adjust the 16 ns readout window of every pixel so that the FF pulse peak is at its center. This way it is made sure that most pulses from Cherenkov photons, since they follow a similar pattern, will be saved to the buffer with their peak at the center of the readout window. It is important for the peaks of the pulses for every pixel to coincide in the recorded data, as this will lead to more precise analysis. The technique for readout window adjustment will be discussed in the following subsections.

4.2.2 Global fit vs local fit

For the purpose of adjusting the readout window, the position of which is expected to fluctuate throughout time, since the camera hardware is not ideal, it is necessary to transform the distribution histogram data from each pixel into a single pulse. After fitting the data, we remove the influence of the pedestal noise. Then, we find at which time moment the level 0 (L0) triggering for recording a detected signal happens. With the current calculation parameters, this happens at a pixel threshold $P=5.5$ p.e., meaning that we are interested in the point where each flat-field pulse reaches that intensity.

The previous algorithm employed to fit the distributions in order to find where the peak of a flat-field pulse is most likely reached, used to fit the pedestal noise serially for every one of the 16 samples with a 1 ns time distance of the readout window to a different Gaussian distribution. Thus, it was giving different positions of the pedestal, even though it is with a very high probability constant throughout a pulse of 16 ns, as it is a very short time interval for major environmental or hardware related changes to occur. Using different parameters for every pedestal distribution could lead to overestimation of one of either the pedestal or the

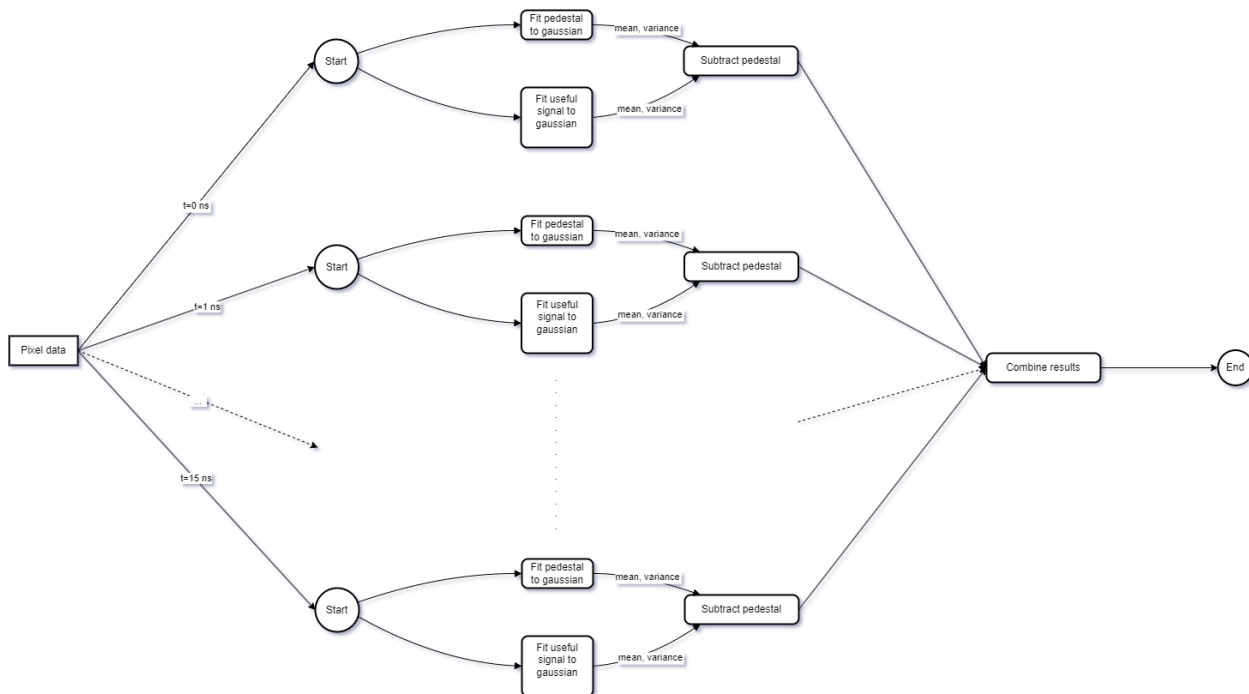


Figure 4.2.1: Local fitting scheme: each sample is fitted separately, with an individual pedestal distribution. This results in a different pedestal being subtracted from each sample.

useful signal and underestimation of the other, in samples where the two distributions are close to each other, giving biased mean and standard deviation of their distributions. A more robust fit is achieved using an algorithm which determines the pedestal values globally, for all 16 sample distributions of an FF-run of a pixel. Additionally, the previous method uses a Gaussian distribution to describe the useful signal, even though it may not be symmetric, hence adding some extra bias to the results. The local fitting scheme versus the proposed global fitting scheme can be seen in the diagrams in Figures 4.2.1 and 4.2.2 respectively.

Another issue is that the algorithm required the adjustments to be done using the on-site server, and manipulating large ROOT5 objects, taking more than 10 minutes for all necessary readout window offsets to be calculated. A useful tool to confront this challenge is the DESY Grid infrastructure[11], which offers a batch system with around 400 servers, enabling data fitting to be done simultaneously for different distributions.

4.2.3 Readout window adjustment taking into account the intensity of the FF LED

As the triggering is done when the signal reaches 5.5 p.e., the camera is calibrated towards higher amplitude signals, since the information saved temporarily in the buffer will begin after the trigger. This means that if the signal which caused the trigger does not rise beyond 5.5 p.e., it will either not be recorded at all or only its falling edge will be recorded (if the peak is equal to 5.5 p.e.), possibly losing important information. Though, with the addition of CT5, which has a lower detection threshold, H.E.S.S. is trying to reduce the threshold of the array altogether, so that lower energy Cherenkov light can also be detected and stereoscopically reconstructed. Stereoscopic reconstruction is possible if at least one more telescope, from CT1-4, also detects the same event. This issue can be addressed by shifting the 16 ns readout window, so that its center is located at the moment of the trigger, making it more possible to properly detect weaker pulses.

The ROOT format

The initial data from HESS-IU calibration runs is stored in ROOT5 format. ROOT is a data analysis framework developed by CERN [12] and written in C++, used for analysis and simulations in various particle and astroparticle physics experiments around the world. Though, its overcomplexity, with an excessive need for

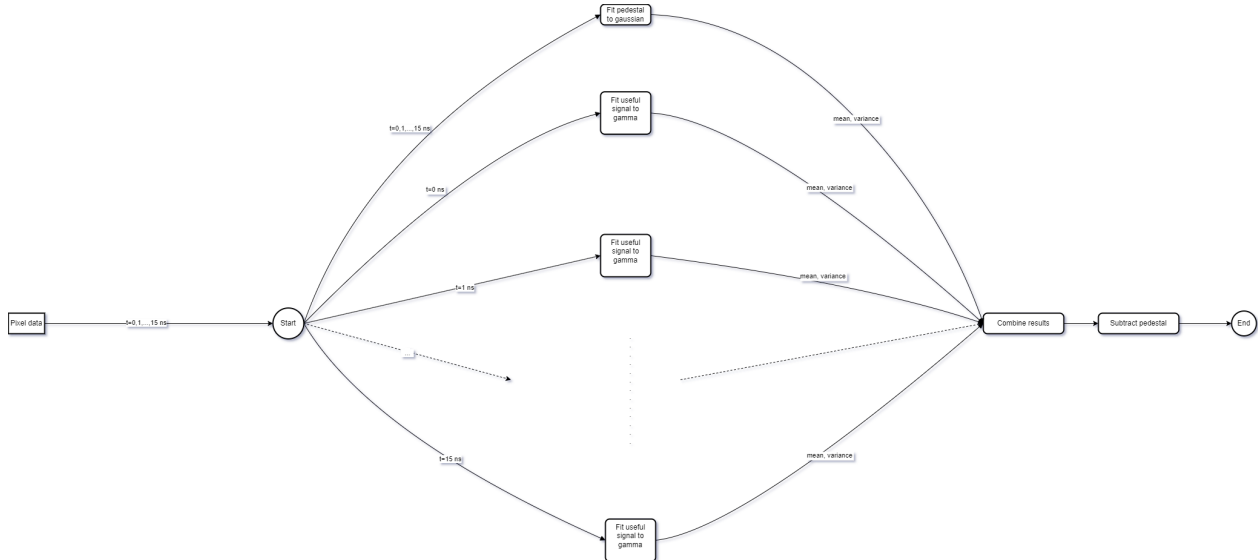


Figure 4.2.2: Global fitting scheme: one pedestal noise distribution is fitted simultaneously for all 16 samples, along with their separate useful signal gamma distributions, in contrast to the previous algorithm. The same pedestal is subtracted from each individual sample.

global variables and perplexed class hierarchy, cause some limitations in data manipulation compared to `python`. This is the reason why the following analysis is done using `python`.

Specifically for the FF runs, the data come in 3-dimensional histograms of distributions of the of the amplitudes (in ADC counts) of the voltage pulses produced by the PMTs for every pixel, for 16 samples, $\tau = 1ns$ apart. Only data from the High Gain channel is used. Profiling the histograms in two dimensions produces a histogram for each sample, as seen in Figure 4.2.3. In this plot one can also differentiate between the pedestal noise, which causes the horizontal line, and the useful signal in the form of a pulse. The pedestal remains at the same point as time passes, while the intensity and variance of the useful signal changes. In order to handle the data more easily in `python`, in this analysis the initial `.root` files are transformed into `.npy` files, using the PyROOT interface[13].

Performing a global fit on the data

In the original format, as well as in the profiled histograms, there is an evident pedestal with a mean value at around 415 ADC counts, created by electronic noise, while its width depends on night sky background (NSB). The rest of the data is the useful signal, from which the calibration parameters are derived.

In order to fit the data in parallel, for every pixel it is assumed that the pedestal follows a Gaussian distribution of fixed amplitude A , mean μ and standard deviation σ for every one of the 16 samples:

$$g_1(x) = A \frac{1}{\sigma\sqrt{2\pi}} e^{-\frac{1}{2}\left(\frac{x-\mu}{\sigma}\right)^2} \quad (4.2.1)$$

On the other hand, since the useful signal is not necessarily symmetric and may be skewed, it is considered that the signal follows a Gamma distribution with different parameters C , α and β , as well as an offset l for each sample of the same pixel:

$$g_2^{(i)}(x) = C_i \frac{(x - l_i)^{\alpha_i - 1} e^{-\beta_i(x - l_i)} \beta_i^{\alpha_i}}{\Gamma(\alpha_i)}, \quad i = 1, \dots, 16 \quad (4.2.2)$$

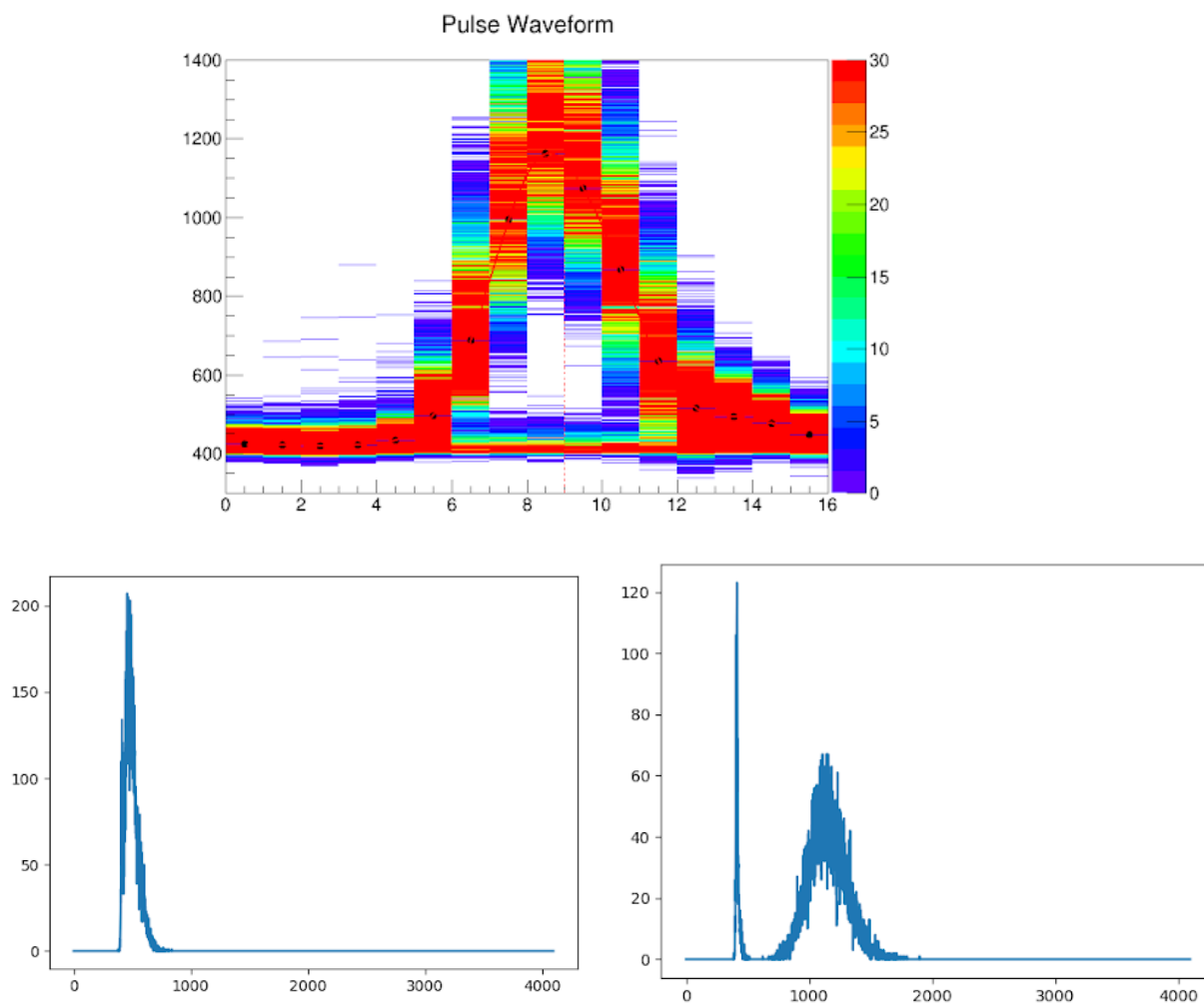


Figure 4.2.3: ROOT5 format histograms for a pixel. Top: Original ROOT5 format. The horizontal axis represents time, giving the number of each 1 ns sample, while the vertical axis represents amplitude in ADC counts. The ADC counts for each sample are given in histograms. ; Bottom: Profiled histograms for samples at 6 and 10 ns, each representing one vertical slice of the previous plot.

where $\Gamma(x)$ is the gamma function, defined as:

$$\Gamma(x) = \int_0^{\infty} s^{x-1} e^{-s} ds \quad (4.2.3)$$

The final distribution would then be equal to the superposition of the above two distributions:

$$G_i(x) = g_1(x) + g_2^{(i)}(x), \quad i = 1, \dots, 16 \quad (4.2.4)$$

Defining these functions for one pulse for a pixel creates 67 unknown variables that need to be predicted. Out of those, 3 are common across all 16 histograms and dependent from the other ones. This is necessary to ensure that the pedestal will be the same for all samples.

The algorithm contains the following steps for each pixel:

1. Preprocess every sample separately to find initial parameters
2. Fit the single gaussian distribution for the pedestal along with the gamma distributions of all individual samples
3. Calculate the mean of every gamma distribution and subtract pedestal
4. Fit the above values to recreate a single pulse
5. Calculate shift in readout window

Every sample is preprocessed in order to define some initial parameters, as the process might be too time-consuming otherwise. Each histogram is then fitted with the least squares method, which iterates over the distribution parameters, until the squared sum of the errors for all points is minimum, or the maximum number of iterations is reached, producing the above function which is a sum of a Gaussian and a Gamma distribution as seen in Figure 4.2.4.

The valuable part of the resulting function is the mean and error of the gamma distribution of each sample, as they will then be used to fit the final pulse shape. The mean of the gamma distribution is defined as:

$$\mu_i = \frac{\alpha_i}{\beta_i} - l_i, \quad i = 1, \dots, 16 \quad (4.2.5)$$

By removing the pedestal and using the means and errors of the useful information of each sample, the signal shape is defined. The resulting pulse is modelled empirically by the following analytical function:

$$f(t) = ct^q e^{-bt} \quad (4.2.6)$$

where c , b , q are the constants which need to be predicted. This is again done with the help of the least squares method.

The success of the fit is evident in Figure 4.2.5, where recreated pulses are superimposed on the original ROOT data (the mean of the pedestal has been added to the pulses for the comparison).

With the previous calibration parameters, the triggering is done at 5.5 p.e, often before the signal achieves its peak and the center of the readout window is not at the peak of the signal, since it is at 7 ns. The solution to this problem is to adjust the center of the readout window to the position of the trigger, so that the PMTs are calibrated towards the majority of the signals. This is demonstrated in Figure 4.2.6, where the proposed shift in the readout window would be the difference between the two timestamps (at 7 ns and at the time of trigger occurrence).

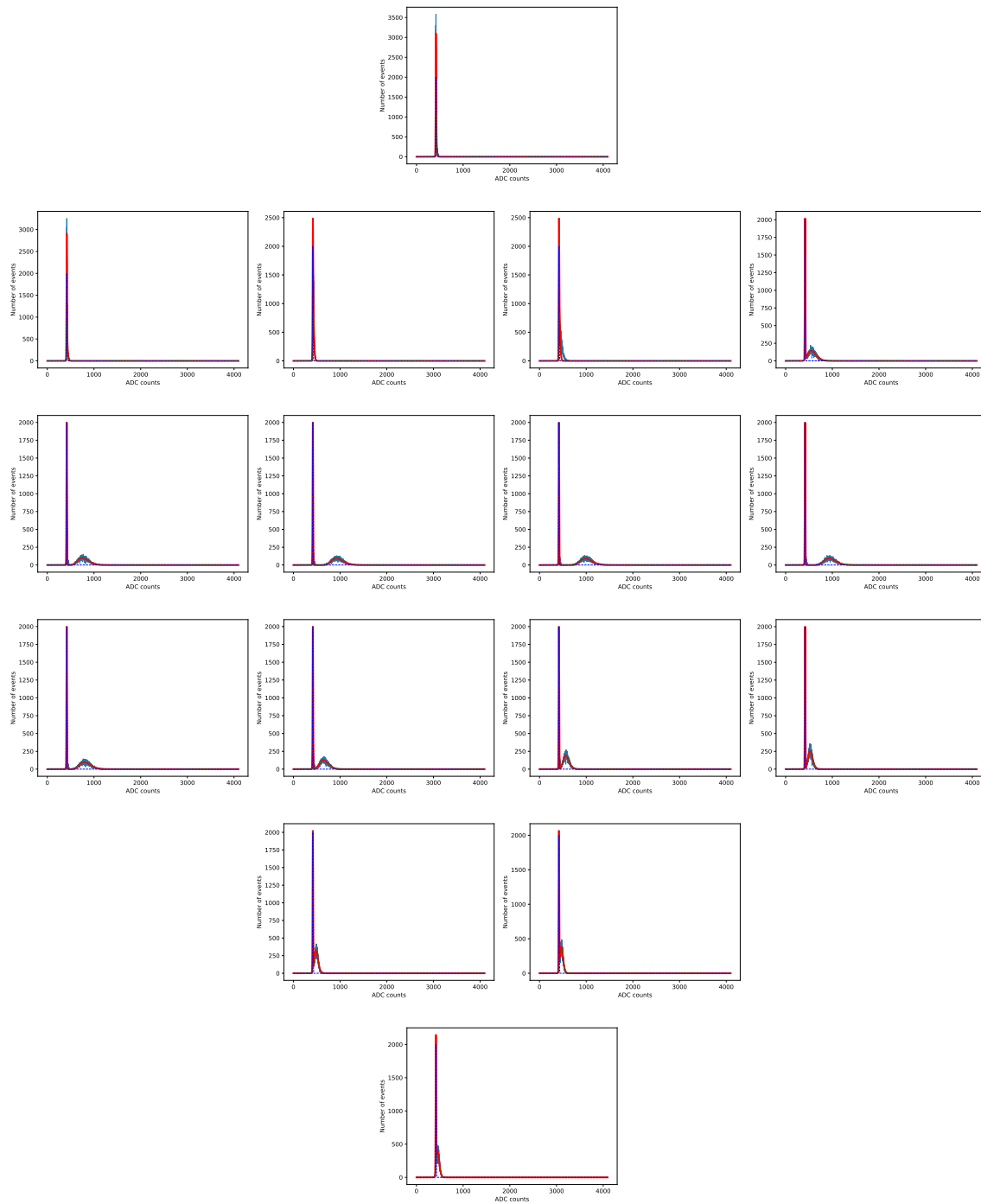


Figure 4.2.4: Sequence of samples fitted to sum of gaussian (pedestal) and gamma distribution (useful signal). The original signal is shown with blue solid line, the gaussian and the gamma distributions with dashed blue and green lines respectively, and the overall modelling function with a red solid line.

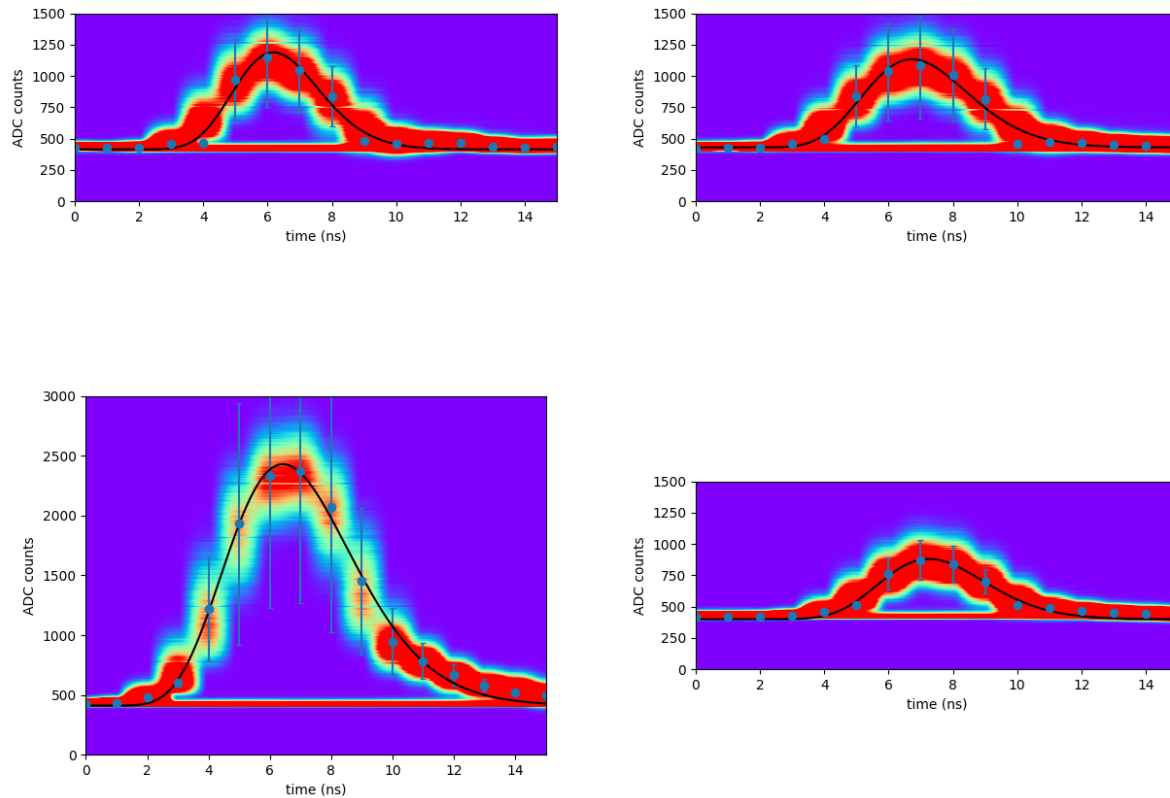


Figure 4.2.5: Recreated pulses on ROOT format histograms. Top left: CT1 pixel 255 ; Top right: CT2 pixel 7 ; Bottom left: CT3 pixel 684 ; Bottom right: CT4 pixel 778

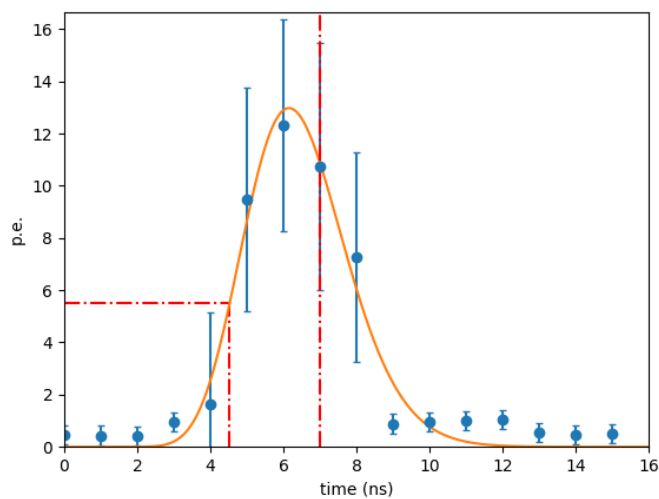


Figure 4.2.6: Pulse for CT1 pixel 255, indicating trigger threshold at 5.5 p.e. and 7 ns timestamp.

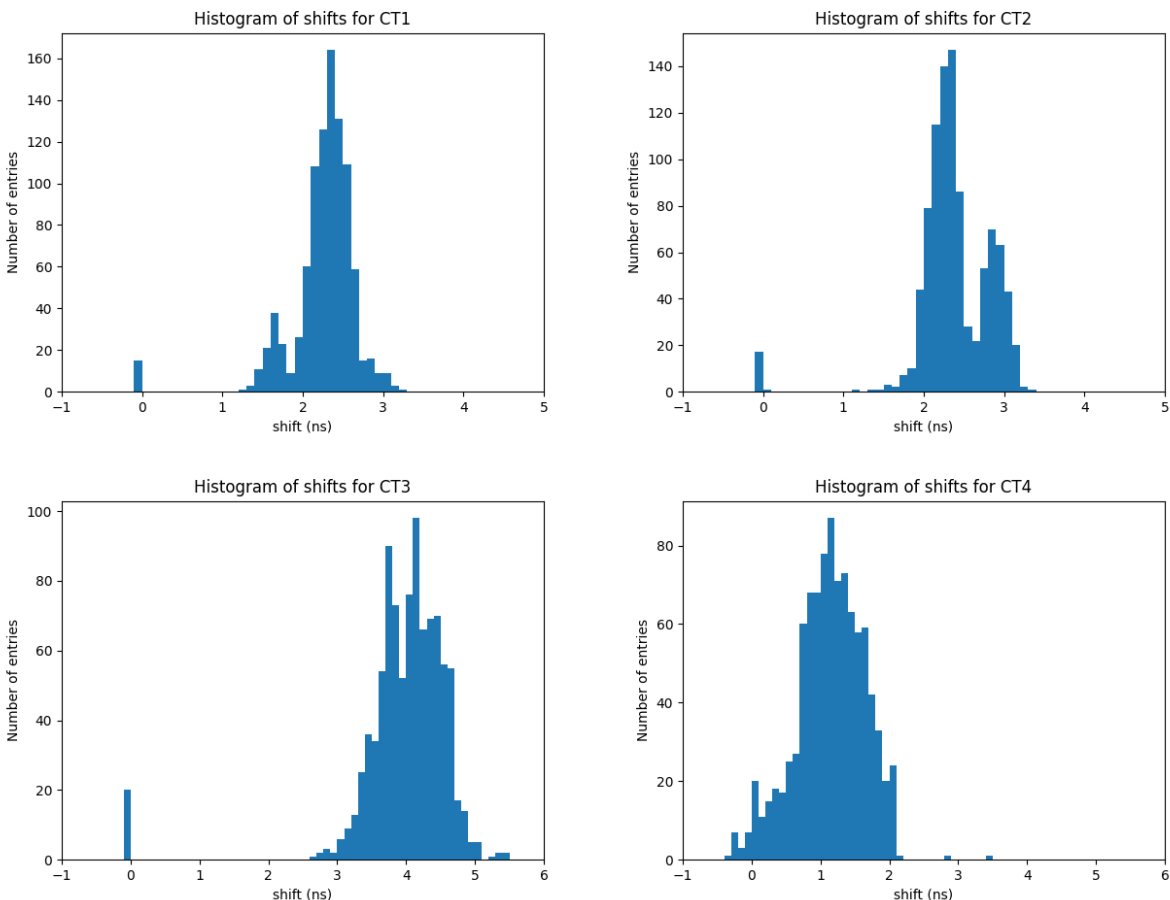


Figure 4.2.7: Histograms of proposed shifts in readout window positioning.

4.2.4 Results

Figure 4.2.7 shows the histograms of the proposed shift in the readout window positioning for all pixels for CT1-4. These were experimentally applied to the telescope, resulting in better time uniformity between the telescopes on data, since after the adjustment, there was a similar average pixel time for all telescopes. It is obvious that CT3 needed larger adjustments than the other three telescopes, as it was affected the most by the previous calibration parameters and calibrated towards higher amplitude photoelectron pulses. The zero values correspond to dead pixels.

4.3 Adjusting Single Photoelectron gain calibration with a global fit

The Single Photoelectron calibration method used in the H.E.S.S. telescopes is described in [9]. It is used to estimate the gain of each individual pixel. Even though the desired value for the PMT gain used for the analysis is fixed at 60 ADC counts for regular camera operation, the PMT gain effectively changes over time due to their aging and drifts from this value under the constant applied voltage to the PMT. Thus, since it depends on the PMT voltage, we have to find how much the voltage should change in order to reach the 60 ADC count desired value. We adjust the previous algorithm, modelling the gain as a linear function of the applied voltage and performing a global fit on the parameters of the linear relationship for all samples.

4.3.1 Converting ADC counts to photoelectrons

As with FF calibration, special Single Photoelectron (SPE) calibration runs are taken once in roughly every two days. In SPE calibration the response to different high voltages is combined in order to derive the PMT gain, which is the conversion factor between ADC counts and voltage.

The pixel gain is defined as the conversion factor from ADC counts to signal charge. Initially, the PMT voltage V_{PM} is measured in ADC counts across a resistor 16 times, every $\tau = 1$ ns and amplified into a high gain and a low gain channel, with gain G^{HG} and G^{LG} respectively. The resulting signals are converted into a digital signal, which is integrated over the 16 ns time interval. In order to convert ADC counts to Volt, this signal is then multiplied with the factor $V_{ADC} = 1.22$ mv/Count. If the signal is in the form of a single photoelectron pulse, with a shape $V_{PM,s.p.e.}(t)$, then inverting the last operation gives the pixel gain:

$$\gamma_{e,i}^{ADC} = \frac{G^i}{\tau V_{ADC}} \int V_{PM,s.p.e.}(t) dt, \quad i = HG, LG \quad (4.3.1)$$

4.3.2 Model of the photomultiplier response

As mentioned in Chapter 2, the PMT consists of two fundamental parts, the photodetector, where photoemission through a photocathode takes place, converting the flux of photons into electrons, and the electron multiplier, where the charge of the emitted electrons is multiplied by dynodes via secondary emission. According to [44], these two processes can be considered independent to each other, with the actual response being a convolution of their independent distributions.

Supposed that there is a pulsed light source, the incident photons on the PMT's photocathode produce photoelectrons. Since in reality only a portion of the photons striking the PMT is actually detected, their conversion into electrons and collection by the electron multiplier is a random binary process. As such, it can be modelled by the convolution of a Bernoulli (binary) and a Poisson distribution, which expresses the number of random events occurring in a fixed time interval, but with a known occurrence rate. The resulting distribution is also a Poisson distribution:

$$P(n; \mu) = \frac{e^{-\mu} \mu^n}{n!} \quad (4.3.2)$$

where $\mu = mq$ corresponds to the mean p.e. number leaving the photocathode and being collected by the first dynode of the multiplier, with m being the mean number of incident photons on the photocathode and q its quantum efficiency. $P(n; \mu)$ is the probability of n observed photoelectrons, with a mean occurrence rate μ .

Regarding the multiplier's response, the electron multiplication factor of the first dynode is large (>4) while it decreases gradually through the next dynodes, dropping to approximately 1 after the electrons have passed through a few dynodes. As such, its response can be modelled by a Gaussian distribution:

$$G_1(x) = \frac{1}{\sigma_1 \sqrt{2\pi}} \exp\left(-\frac{(x-1)^2}{2\sigma_1^2}\right) \quad (4.3.3)$$

with x being the output charge variable, Q_1 the mean charge when an electron is multiplied by the first dynode, and σ_1^2 the relevant variance. The mean charge can be determined by the PMT gain G and the elementary charge e as $Q_1 = eG$.

Under the assumption that the responses to different photoelectrons hitting the first dynode are mutually independent, and that photoelectrons missed by the first dynode and collected by the next ones are insignificant, the PMT charge distribution can be expressed as a convolution of different Gaussians, each corresponding to a different number of photoelectrons:

$$G_n(x) = \frac{1}{\sigma_1 \sqrt{2\pi n}} \exp\left(-\frac{(x - nQ_1)^2}{2\sigma_1^2}\right) \quad (4.3.4)$$

where n is the number of p.e., the variance is the same for each Gaussian, while the mean charge of n p.e. is a multiple of the mean charge of 1 p.e. This distribution gives no charge for $n \rightarrow 0$, since $G_0(x) \rightarrow \delta(x)$.

Then, the ideal response of a PMT is a convolution of the equations 4.3.2 and 4.3.4:

$$SPE_{ideal}(x) = \sum_{n=0}^{\infty} \frac{e^{-\mu} \mu^n}{n!} \frac{1}{\sigma_1 \sqrt{2\pi n}} \exp\left(-\frac{(x - nQ_1)^2}{2\sigma_1^2}\right) \quad (4.3.5)$$

In reality, there are processes in a PMT which generate noise. Low charge processes generating the electronic pedestal and producing a nonzero charge distribution even when there are no flashes from a pulser, can also be modelled by a Gaussian distribution with an independent smaller mean value and variance.

4.3.3 SPE Calibration

In contrast to the FF runs, SPE runs are done with the cameras in shelter, resulting in no wide pedestal distribution caused by night sky background, but only in an offset by the electronic pedestal noise in each sample. These runs use an LED pulser, located two meters away from the cameras, along with a diffuser, giving each camera a homogeneity of 0.5 factor in light intensity. The pulser emits light which illuminates each pixel with intensity corresponding to around 1 photoelectron, with a frequency of 70 Hz. The runs are programmed to have a small delay in every event before the trigger, so that the SPE pulse is at the center of the 16 ns readout window. Even though the pulser emits one photoelectron, the pixel will most likely observe more than one photoelectron, due to secondary emission. Integrating the acquired distributions of ADC counts for all of the samples in the region of interest, will give the SPE charge distribution, with different components corresponding to the integrated pedestal distribution and individual values of photoelectrons collected by the anode.

In order to model the SPE charge distribution according to the arguments of the previous subsection, the following three assumptions are made: the number of photo-electrons follows a Poisson distribution, the electronic (pedestal) noise is much smaller in width than the SPE distribution and one photoelectron is described by a Gaussian distribution. The resulting modelling function is the following:

$$SPE(q) = N \frac{e^{\langle k \rangle}}{\sqrt{2\pi}\sigma_P} \left[-\frac{(q - \mu_P)^2}{2\sigma_P^2} \right] + N_s \sum_{k=1}^{k \gg 1} \frac{e^{\langle k \rangle}}{\sqrt{2\pi k}\sigma_G} \frac{k^k}{k!} \exp\left[-\frac{(q - (\mu_P + kG))^2}{2k\sigma_G}\right] \quad (4.3.6)$$

where μ_P, σ_P are the mean and standard deviation of the pedestal distribution, G, σ_G the mean and standard deviation of the gain distribution, $\langle k \rangle$ the mean light intensity. N and N_s are normalisation factors, corresponding to the number of events in a run. According to this function, the SPE distribution is a superposition of gaussians, where the first narrower distribution corresponds to the pedestal, the second distribution corresponds to one photoelectron events, the third distribution corresponds to two photoelectron events, etc. The mean of each gaussian is proportional to the number of photoelectrons.

The aim of this analysis is to determine the gain G of the high gain channel, thus the HG superscript is omitted. As before, only the data from the high gain channel are used, since the gain in the low gain channel can be determined by multiplying G with the conversion factor between the two channels. This factor can be found by dividing the amplitude of the pedestal measured in the low gain channel with the one measured in the high gain channel.

4.3.4 Another global fit, assuming linear gain

For the purpose of determining the gain accurately, different high voltages are applied to the PMT during SPE runs and the recorded distributions in each PMT are fitted to the above superposition of gaussians. The unknown variables in the above function are 4 for each run: μ_P, σ_P and G, σ_G . Then the final value of the gain is determined combining the result from all runs.

We use $max(k) = 10$, since for higher values the distributions become insignificant compared to the data. The previous algorithm fits each run serially, considering the variables of each run independent from each other, giving 36 unknown variables. Though, as the voltage increases, so does the tail of the signal implying that

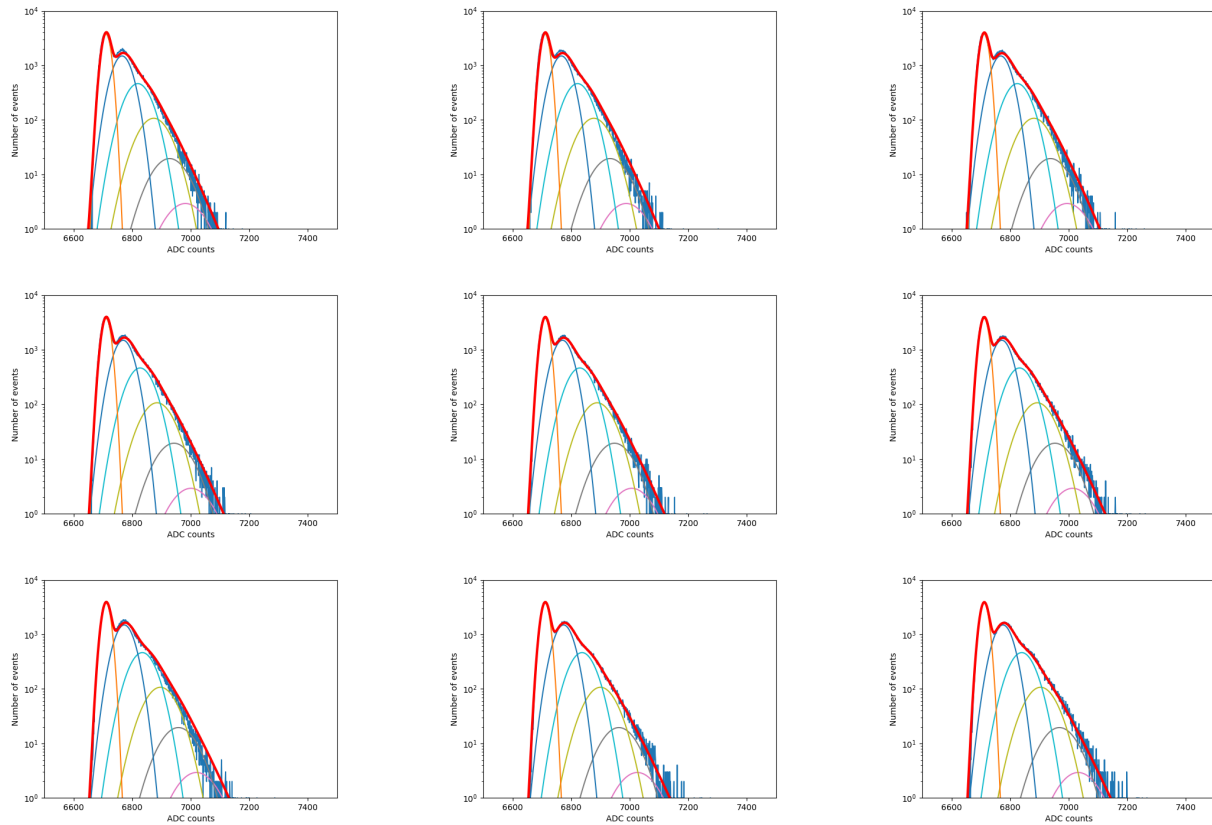


Figure 4.3.1: Global fit on gain for runs from $dV = -20$ to $dV = +20$ for CT2 pixel 0, in logarithmic scale. The original signal is marked with a dark blue line, while the different gaussian distributions corresponding to different p.e. values are marked each with a different colour. The resulting distribution is shown with red. It describes the data well, with the gain (in ADC counts) increasing as the voltage increases.

the pixel gain is roughly linear with regards to the applied voltage. This means that if the gain is modelled as a straight line, there will be less variables, making the gain determination computationally easier. Assuming linear gain:

$$G = \alpha dV + \beta, \quad \alpha, \beta : \text{constant} \quad (4.3.7)$$

the unknown variables are reduced to just 20.

Again, the initial SPE run data for each pixel are in ROOT5 format and consist of histograms of integrated ADC counts for each one of 9 different runs, each for a different high voltage dV , varying from -20 to 20 V with a step of 5V, with respect to the actual PMT voltage. Only the data from the high gain channel are used. The algorithm does the following:

1. Smoothen the signal using a Savitzky-Golay filter
2. Calculate initial values for μ_{P0} , G_0 for $dV = 0$ taking into account the first two peaks of smoothed signal
3. Perform a global fit for the SPE distribution combining all runs and predict α , β
4. Determine the required voltage difference dV in order to have $G = 60$

The results of the fit can be seen in Figures 4.3.1, where we show the fitted gain gaussians for a few of the different runs and 4.3.2, where we show the resulting gain-voltage line. Figure 4.3.3 shows the measured effective PMT gain values before any correction, where one can see that most pixels need correction in order to have the desired value.

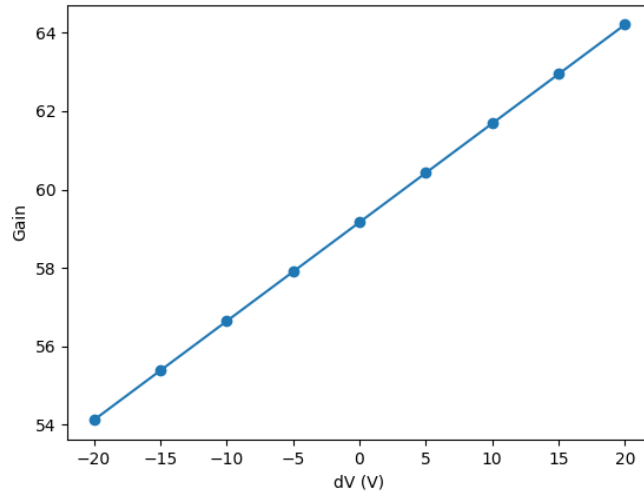


Figure 4.3.2: Resulting gain line after global fit for CT2 pixel 0. For zero adjustment to voltage, the gain is a few ADC counts below 60.

4.3.5 Results and comparison to standard algorithm

Figure 4.3.3 shows the measured effective PMT gain values before any correction, where one can see that most pixels need correction in order to have the desired value of 60. Histograms of the proposed gain changes in PMTs for the telescopes in comparison to the results from the previous (standard fit) method can be seen in Figure 4.3.4. Small differences from cross-check are within the bounds of uncertainty and were expected since we are using two different fitting methods. The new method is more robust, since it requires just one iteration. This makes the gain calibration faster compared to the standard approach, which needed often resulted in false minima and needed more than one iteration. Thus, the global fit assuming linear gain accelerates the gain determination process by using less parameters, while producing consistent results.

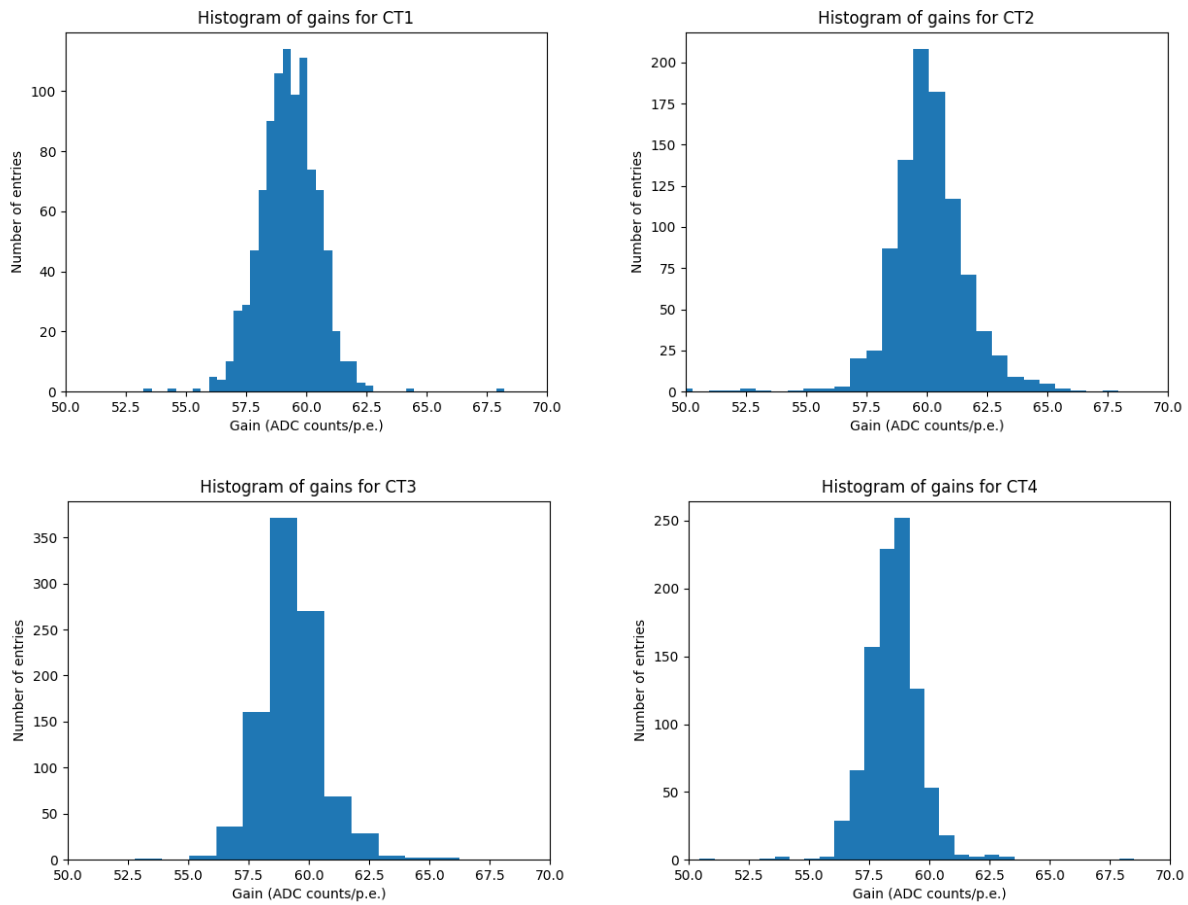


Figure 4.3.3: Histograms of PMT gain values for all telescopes. Most pixels need correction, as their gain value does not coincide with the desired value.

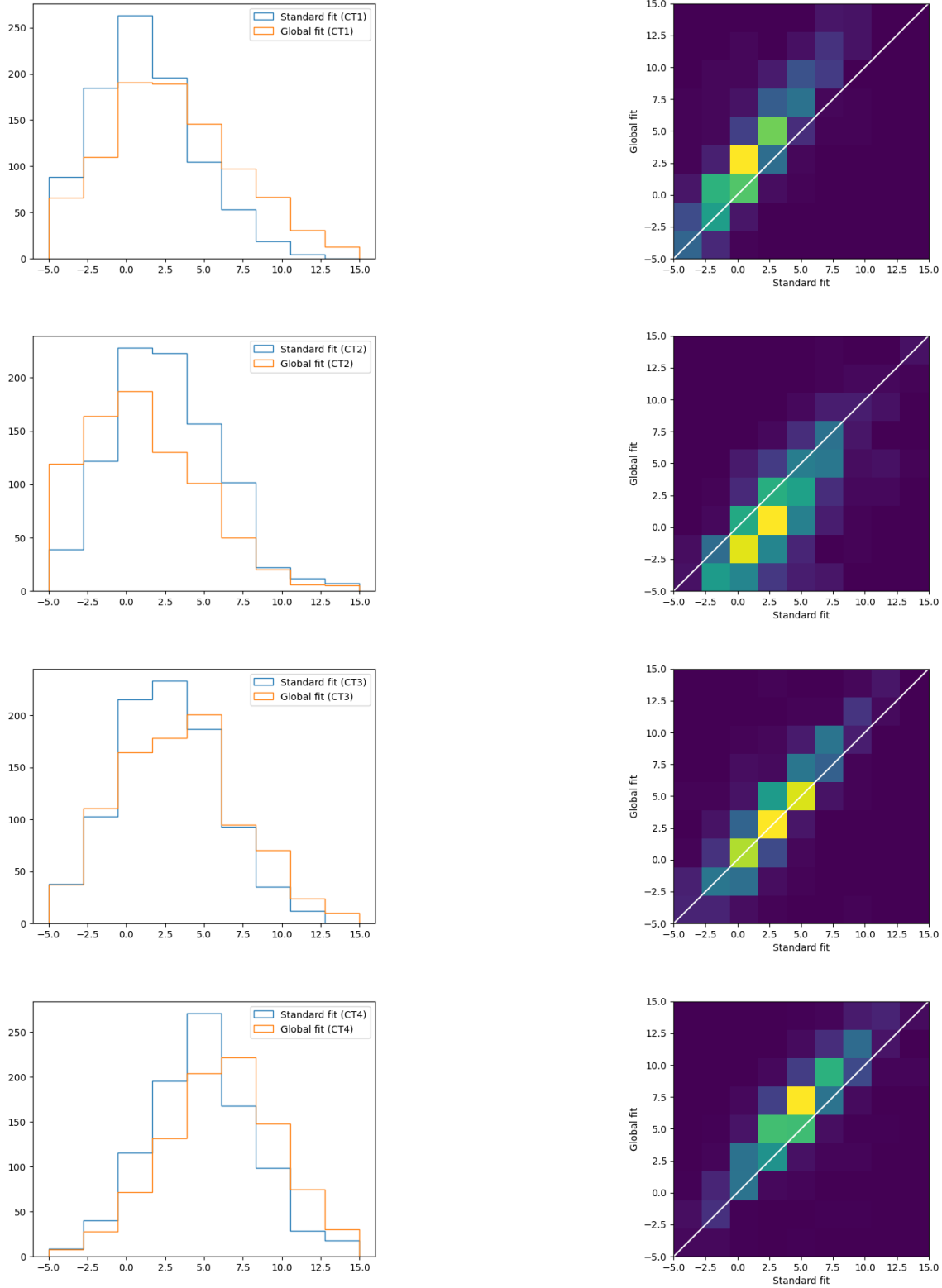


Figure 4.3.4: 1D and 2D histograms of proposed changes in pixel gain in Volts for CT1-4 according to new and old algorithm.

Chapter 5

Sample mode to charge mode converter

5.1	Introduction	100
5.2	Charge recovery and a few integrals	100
5.3	Calibration and recovery coefficients	100
5.4	Cross-check with observation data	101

5.1 Introduction

During observations, the information used to reconstruct images of gamma ray emission from sources and perform the analysis is in the form of charge, i.e. the integral in p.e. over the 16 samples of the region of interest of each PMT pulse. Analysing the 16 sample signal is referred to as sample mode, while analysing the resulting integral is referred to as charge mode. The charge is first calculated in ADC counts and then converted to an amplitude in p.e., according to Equations 3.3.1 and 3.3.2 for the high gain and low gain channel respectively.

It is obvious that the final measured amplitude heavily depends on the positioning of the readout window and can be affected in case the readout window is miscalibrated. An example of this problem occurred after a recent replacement of the cameras' trigger board, causing a bias to the amplitudes used in the image reconstruction. More specifically, the hardware change affected the L0 trigger time moment, and caused a shift of the readout window to the right. The L0 trigger signal would be activated when the falling edge of the height of the sample mode pulse reached the trigger threshold, meaning that most recorded pulses were stored missing part of their rising edge. The pulses were stored like this for a period of a few weeks, having a strong effect on the data used for the reconstruction and analysis of events. In this chapter, we will propose a method to partially recover the affected data. The analysis is done using HTCondor[14].

5.2 Charge recovery and a few integrals

For the purpose of converting sample mode data to charge mode data, we take advantage of the fact that most pulses have a similar shape, modelled by the analytical function from Eq. 4.2.6 and can vary only in width, amplitude and time of peak. Thus, if during our readout window of n samples we have recorded a sufficient portion of the sample signal, consisting of at least m samples, we can multiply its integral with a coefficient C in order to recover the integral of the whole signal. In our case, we consider that recovery of the integral of the $n = 16$ sample signal is possible with at least $m = 9$ samples. At the same time, we consider that the readout window has been shifted for a specific time offset of a few ns to the right, as has happened with the trigger board replacement.

We define the following quantities, which represent charge of a signal around its peak in ADC counts:

$$q_9 = \int_{t_0-4.5}^{t_0+4.5} f(x) dx \quad (5.2.1)$$

$$q_{16}(t') = \int_{t_0-8}^{t_0-8} f(x+t') dx \quad (5.2.2)$$

The first quantity corresponds to the 9 sample integral around the time t_0 where the peak of the signal in a regularly calibrated readout window is, while the second quantity corresponds to the 16 sample integral of the whole signal around its initial time of peak when the signal is shifted t' ns to the left (or the readout window is shifted to the right).

The 16 ns integral is the charge which we have to recover in order to properly conduct the analysis of observations. For this reason, we will use q_9 and parametrise the recovery of q_{16} .

5.3 Calibration and recovery coefficients

In order to tackle the problem, we use the data from 10 different calibration runs utilising the SPE unit and flashing the HESS-IU cameras with varying light intensity. Afterwards, these pulses are fitted and parametrised using the method described in section 4.2, with the sole difference of not having to fit a pedestal distribution, as these runs are performed with a closed camera lid, hence not affected by night sky background. This is done for all pixels of all 4 cameras for every run. An example of such a pulse can be seen in Figure 5.3.1.

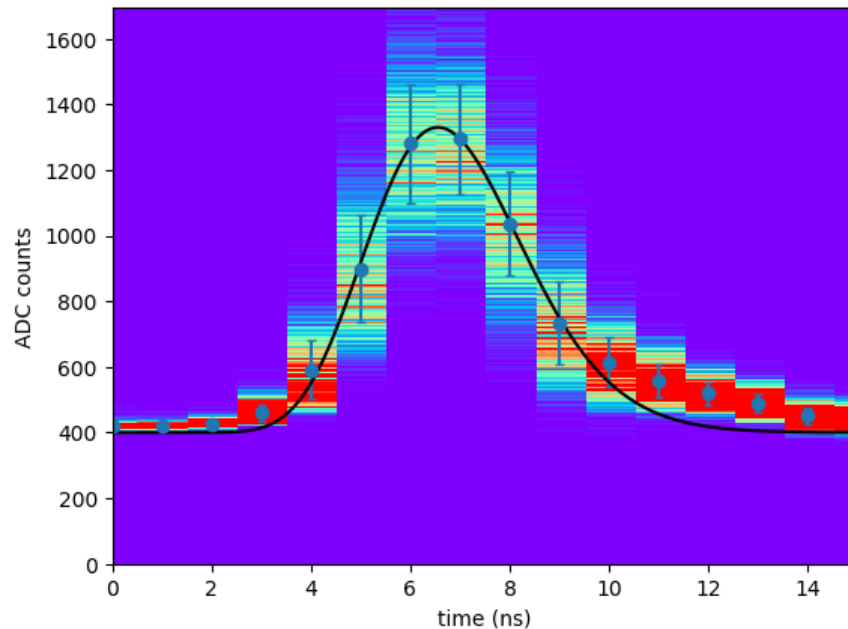


Figure 5.3.1: Pulse from the SPE unit used for the calculation of charge recovery coefficients. The pulse has been fitted to an analytical function after removing the pedestal offset and calculating the mean value of the ADC distribution for each sample.

Since the shape of the calibration pulses is similar to the shape of the observation data pulses, we can use these calibration runs to calculate the correction coefficients, with which we can multiply the q_9 integral of the observation pulses, assuming we have its approximate value, in order to recover the charge. This is done for by calculating q_9 and shifting the pulse to the left by t' ns, meaning that a part from the left of the pulse is missing, and calculating $q_{16}(t')$. This process is done for $t' = 0, \dots, 15$. Then, the correction coefficients would be:

$$C(t') = \frac{q_{16}(t')}{q_9} \quad (5.3.1)$$

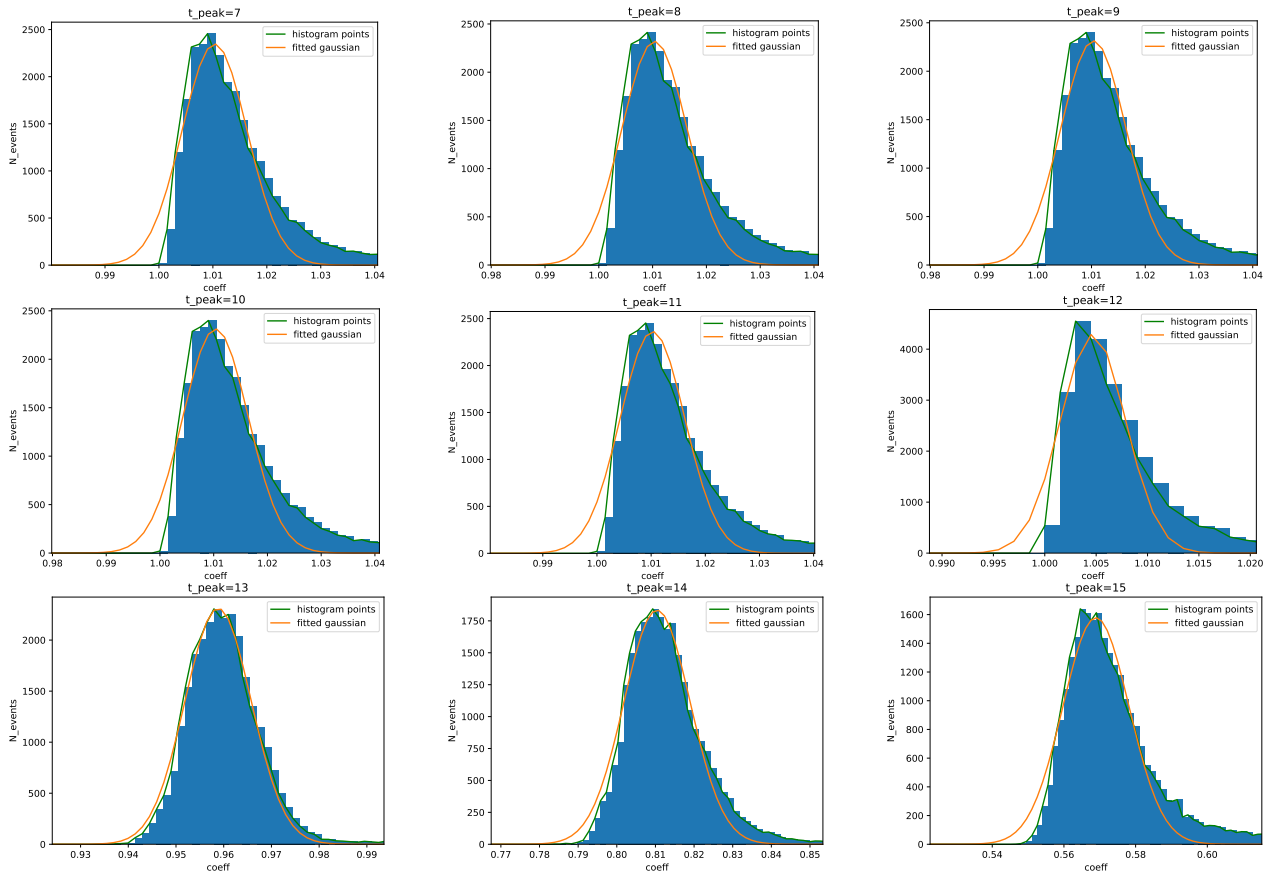
The coefficients for all runs, telescopes and pixels are then placed in a histogram, for each time of peak (equivalent to $t_0 + t'$). These histograms are presented in Fig. 5.3.2, for a time of peak up to 15 ns and in Table 5.1. It is worthy of mention that the coefficients are independent of the light intensity and the amplitude of the sample mode pulses, as seen in Fig. 5.3.4. The first two runs can be discarded for the calculation of the final coefficients, as their low light intensity is equivalent to almost no events above the pedestal and the fit is more unstable. The mean value and standard deviation of the final coefficients, resulting from the histograms of Fig 5.3.2 can be seen in Fig. 5.3.3. The standard deviation is quite small, making these coefficients quite acceptable. It is also notable that the coefficients start from a value slightly higher than 1, for a small part from the left of the signal missing and they steeply fall to 0 for more shifted pulses. This means that for small changes in the position of the readout window, we have proven that q_9 is equivalent to q_{16} . For bigger changes in its positioning, we can use the coefficients that we calculated. Finally, Figure 5.3.5 indicates the results of the crosscheck between the real q_{16} of the calibration data and the reconstructed q_{16} , calculated by multiplying q_9 with the correction coefficient. The uncertainty is quite low (within 5%), indicating that the reconstructed charge is quite close to the real one.

5.4 Cross-check with observation data

We used our parametrisation to see if it can be successfully used for data from actual observations, since our coefficients were calculated using data from calibration runs without night sky background. The dataset consists of around 10^9 events from all telescopes. Some examples of the results can be seen in Figures 5.4.1,

Time of peak (ns)	C
7	1.01
8	1.01
9	1.01
10	1.01
11	1.01
12	1.00
13	0.988
14	0.810
15	0.569
16	0.327
17	0.060
18	0.020
19	0.005
20	0.000
21	0.000

Table 5.1: Reconstruction coefficients for different times of peak.

Figure 5.3.2: Histograms of correction coefficients from q_9 to q_{16} .

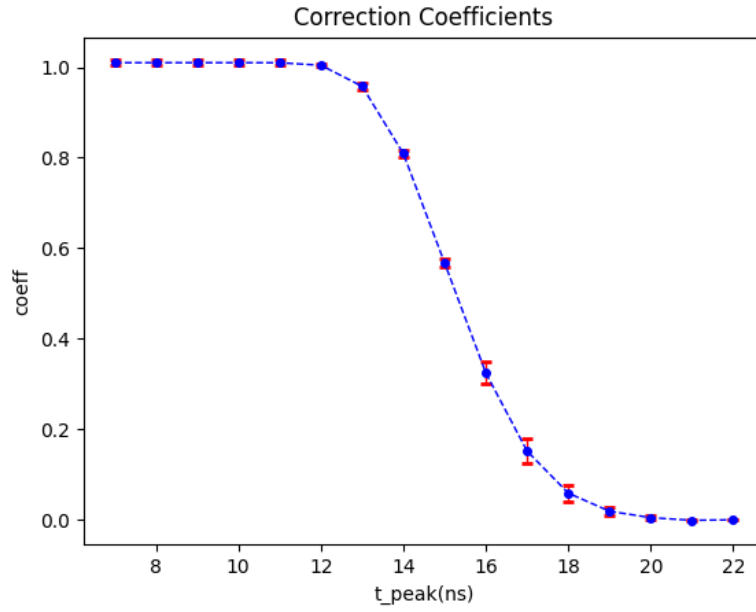


Figure 5.3.3: Mean coefficients with standard deviation. If the pulse is shifted only by a few ns, q_{16} almost equal to q_9 , while for time of peak higher than 12, their ratio steeply falls to zero.

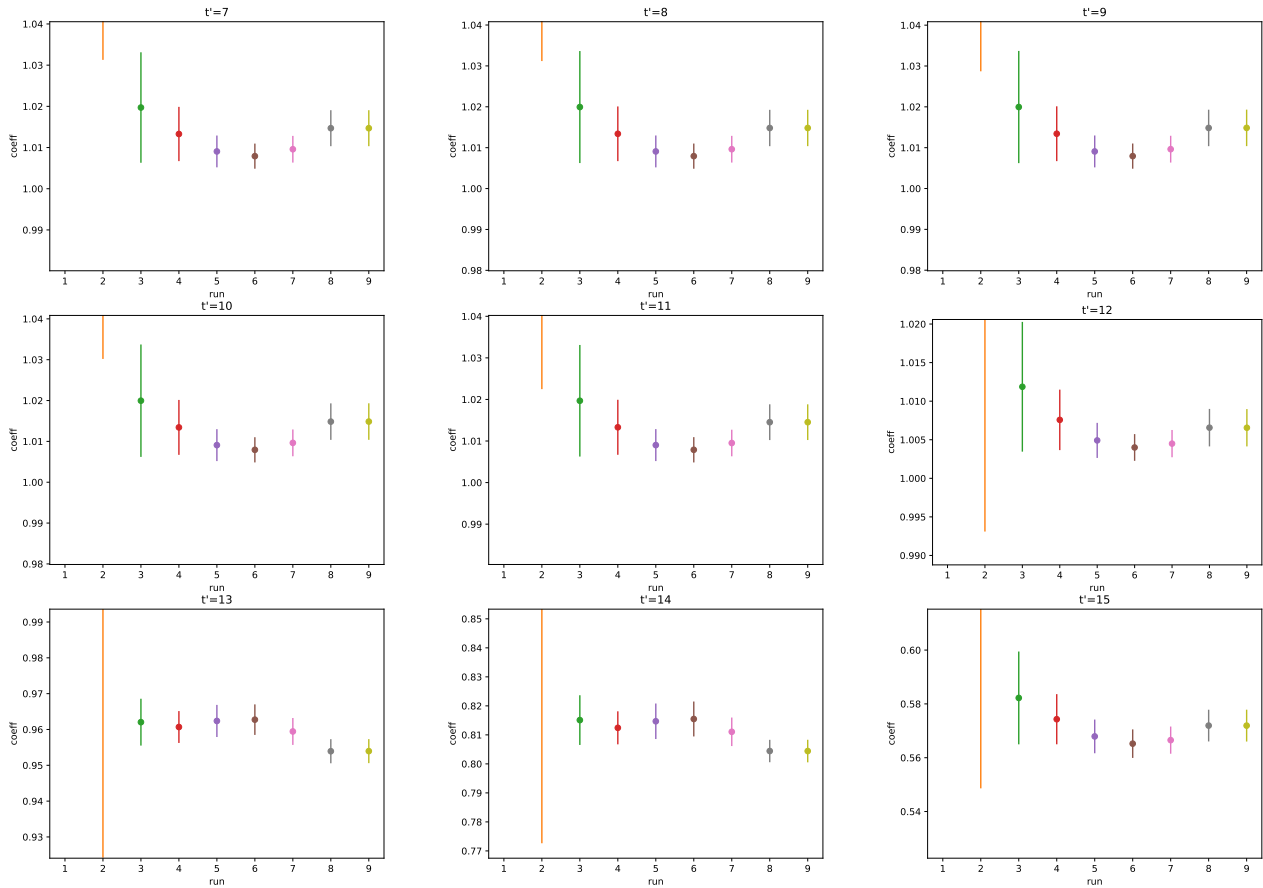


Figure 5.3.4: Coefficients in relation to run (with rising light intensity). There is a higher uncertainty for the first two runs, but it is diminished when the runs have higher intensity.

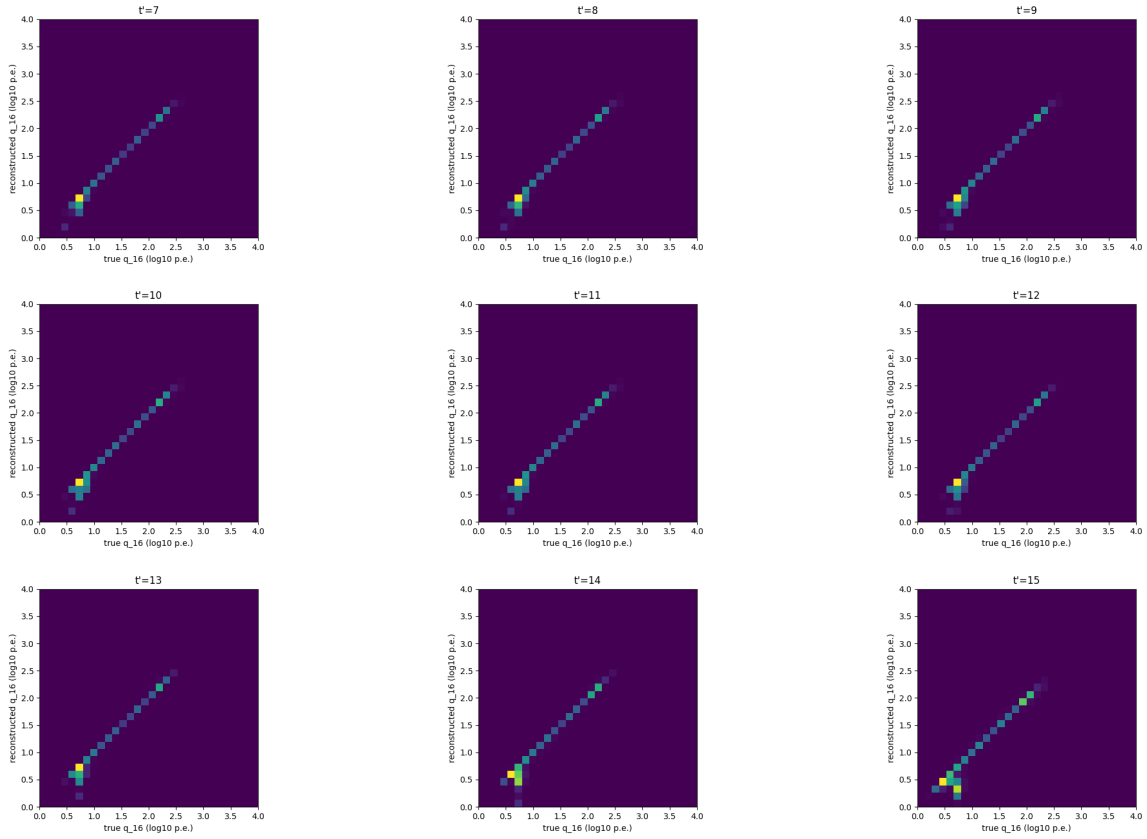


Figure 5.3.5: Cross-check between true q_{16} of calibration data and reconstructed q_{16} for different readout window positions.

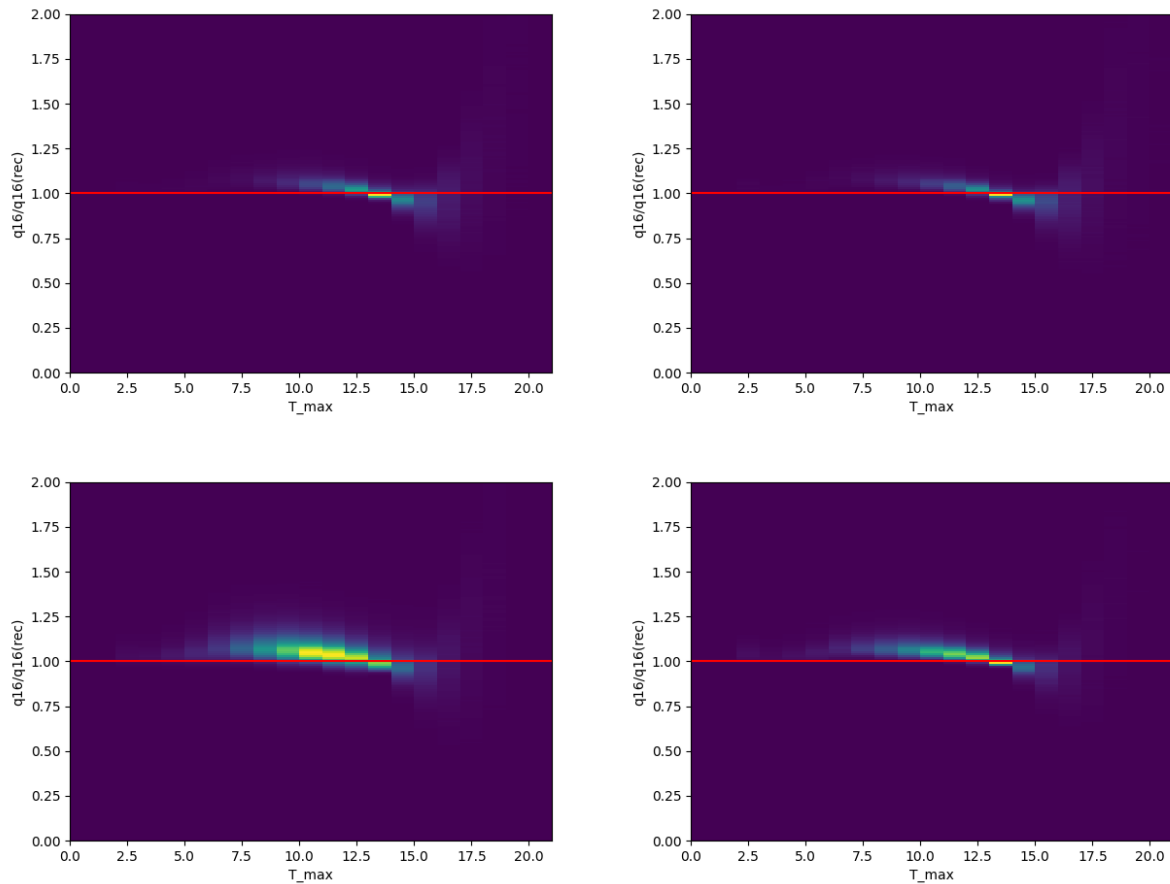


Figure 5.4.1: Ratio between true q_{16} from observation data versus its reconstructed value using q_9 and our coefficients, in relation to time of peak. The plots correspond to different pixels of the four telescopes. Values different than 1 for higher time offset imply the existence of noise. Top left: CT1; Top right: CT2; Bottom left: CT3; Bottom right: CT4.

5.4.2 and 5.4.3. It seems that the reconstruction using our recovery coefficients can be achieved. Though, it exhibits a bias with increasing time of peak, since for a higher offset in the readout window position the charge (q_{16}) should be zero according to our parametrisation. We see that this is not the case with our dataset, where there are high values for q_{16} as time increases, implying that the signal has a long tail. We assume that this happens because of different methods of pedestal subtraction used for calibration and observation. It could be that some night sky background survived the image cleaning process (discussed in Subsection 2.4.6), an issue that was not predicted by our method as we used calibration runs with the SPE unit, with a closed camera lid. Nevertheless, our method is quite promising, if we take into account real observation conditions.

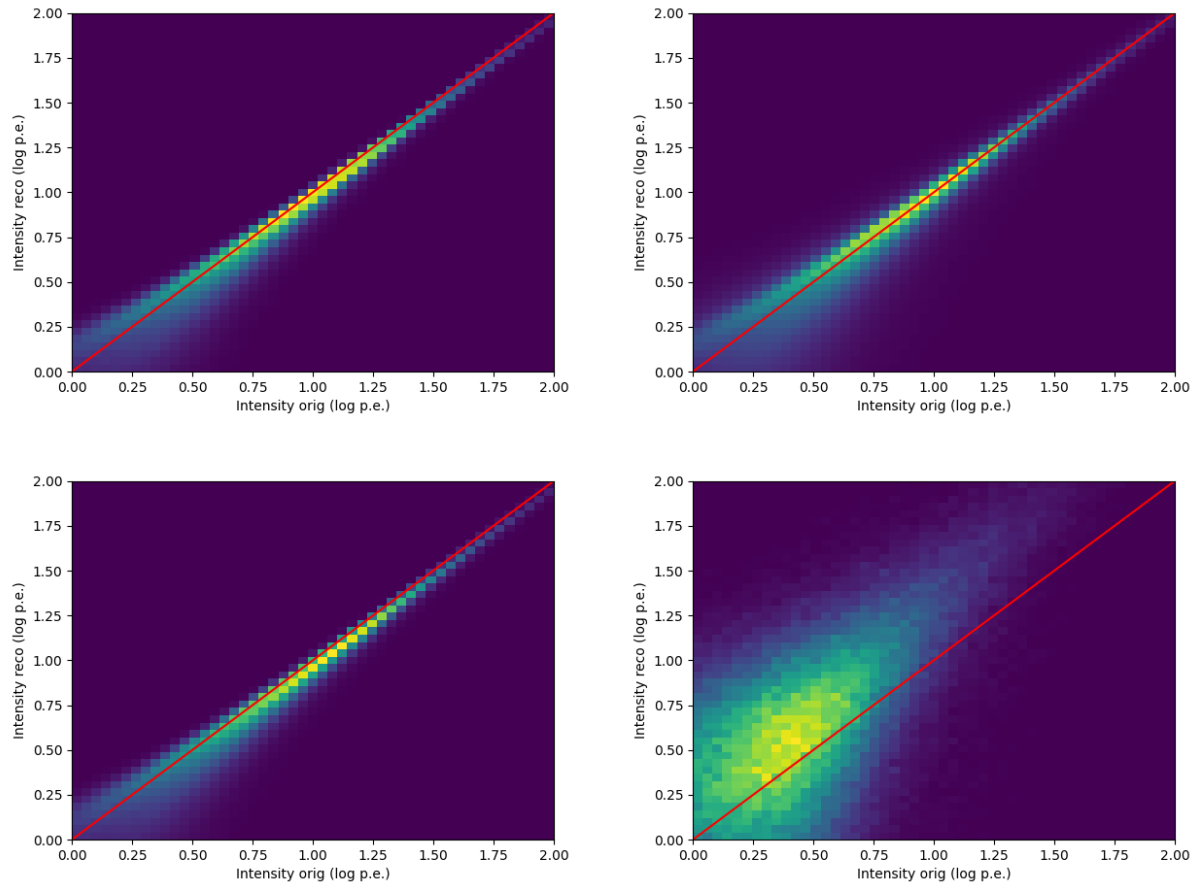


Figure 5.4.2: Comparison between true and reconstructed intensity from observation data. As time of maximum increases, there is higher uncertainty. Top left: CT1, $t=11$; Top right: CT2, $t=9$; Bottom left: CT4, $t=9$; Bottom right: CT4, $t=19$.

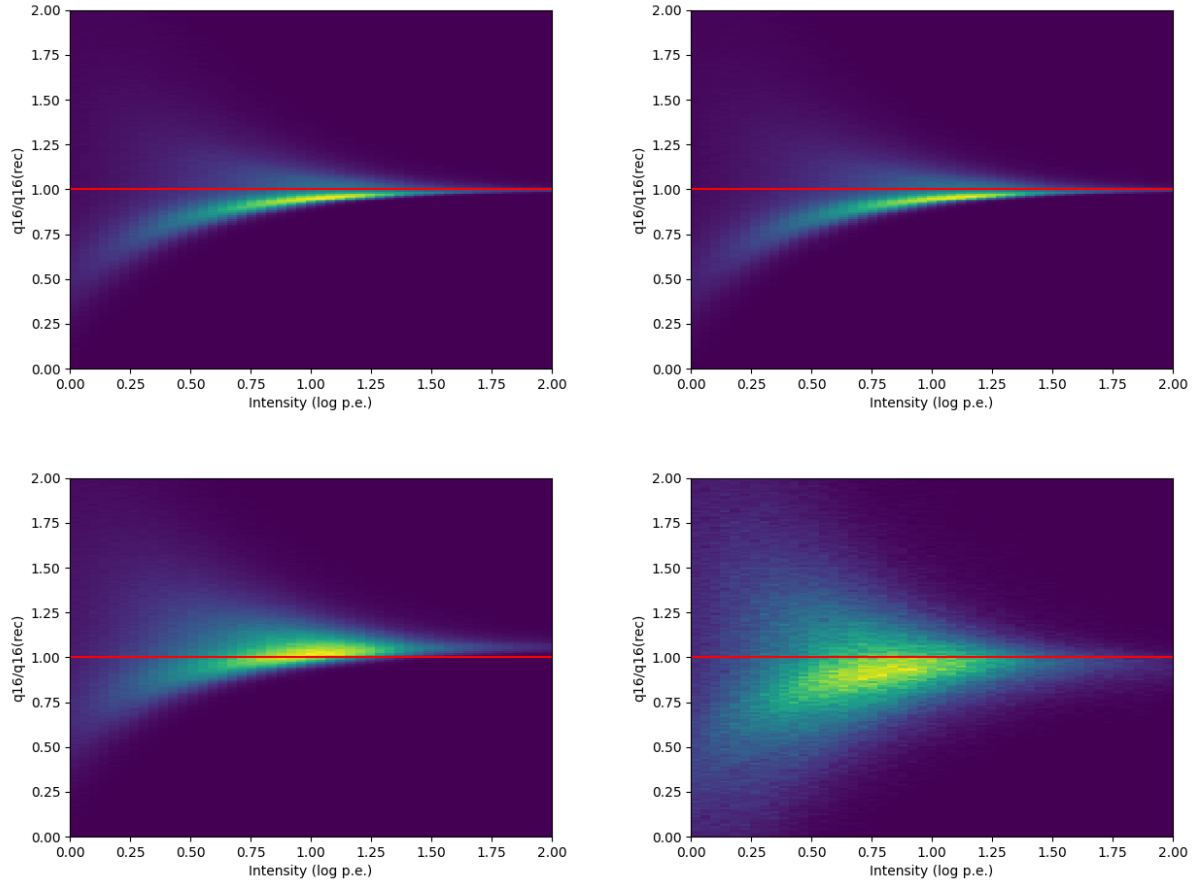


Figure 5.4.3: Ratio between true and reconstructed q_{16} from observation data in relation to intensity. We see that for lower intensity there is higher uncertainty, as was the case with our crosscheck using only calibration data. Also, as time of peak increases, there is higher uncertainty, presumably because of noise. Top left: CT1, $t=13$; Top right: CT2, $t=3$; Bottom left: CT3, $t=10$; Bottom right: CT3, $t=15$.

Chapter 6

Conclusion

6.1	Summary and conclusions	110
6.2	Limitations and future work	110
6.3	Future application of technique and impact on CTA	110

6.1 Summary and conclusions

The High Energy Stereoscopic System (H.E.S.S.) is an array of 5 Imaging Atmospheric Telescopes located in Namibia. Its purpose is to explore the sky in the very high energy gamma-ray domain and has been in operation since 2002. It can be separated in 2 phases: H.E.S.S. I consisting of the 4 12m telescopes and H.E.S.S. II characterised by the installment of a fifth 28m telescope. The H.E.S.S. I telescopes were upgraded in 2015 with the HESS-IU upgrade, which introduced new cameras with a NECTAr chip based readout system. In this thesis, we studied the function of these cameras and their calibration.

In order to preserve their optimal performance, the telescope cameras need to be calibrated regularly, as their hardware is not ideal and degrades with time, introducing unwanted effects and affecting the quality of observations. We introduced two improvements, regarding the cameras' readout window positioning and the deduction of the gain of their pixels. They both include fitting the different data from calibration runs using a global fitting method, which correlates modelling parameters in the different samples, resulting in a more precise readout window adjustment and a more robust gain fitting algorithm.

Another issue was the miscalibration of the readout window for a notable portion of data collected from observation runs, due to hardware replacement. Since the physical quantity used to analyse observations is the charge, meaning the integral of the sampled light pulse over the readout window, we developed a parametrisation which aims to recover the charge mode data from sample mode data.

Considering all the evidence we have using calibration data, the above work has led to significant results. First of all, the readout window readjustment will make the trigger work at the peak of lower intensity signals, making them more centered in the recorded data. It will also address the miscalibrated CT3 timing, resulting in more time uniformity between the telescopes. Additionally, the use of a global fit to describe the pixel gain with a linear equation seems to nicely represent the distribution of the gain calibration data. A comparison with the old method shows a small but acceptable bias, while the new algorithm results in a more robust fit needing less iterations. Lastly, we have successfully parametrised the retrieval of charge mode data using the nine sample integral around the peak of the signal. We performed a cross-check using the derived coefficients, with the reconstructed values from calibration runs giving a very close approximation of the true values. While the cross-check with real data provided satisfactory results, it also indicated the need for us to adapt our method to the conditions under which real observations are made.

In closing, the the HESS-IU calibration has been revisited and improved. Additionally, the conversion from C++ to `python3` has almost eliminated the `ROOT5` dependency, ensuring more efficient data manipulation. The calibration adjustment can now be done using HTCondor or the DESY Zeuthen grid system instead of the server on site and takes only ~ 10 minutes instead of ~ 2 hours. The proposed changes have been presented in H.E.S.S. collaboration meetings and are to be implemented. Finally, we are planning to write a paper regarding the global fit method for gain calibration.

6.2 Limitations and future work

This work, like any other work, obviously faces some limitations, regarding the available time, data and resources. The limited time did not allow us to focus much on fine-tuning the fitting parameters and methods, which could result to an even more precise results and minimum bias. In the future, we could also try training a neural network for the fitting instead of classical approaches, such as the least squares method. Another future direction would be to adjust our data recovery method taking into consideration the effect of noise in observations. At the same time, H.E.S.S. special calibration runs and data can be accessed with specific permission, which means that there was a limited amount of calibration data, some of which could not be used. More data availability could lead to better statistics in cross-check between algorithms and reconstructed versus true data.

6.3 Future application of technique and impact on CTA

The concepts in this thesis can not only have an impact in the calibration of HESS-IU cameras and subsequently their observation data quality, but also in the cameras of the next generation observatory, CTA. The

Cherenkov Telescope Array (CTA)[45] is currently being built and will be the largest and the first gamma ray observatory which will have sites both in the north and south hemispheres. Its medium-sized telescopes (MSTs) in the northern site in La Palma, Spain, will also equip the NECTAr chip. This means that the camera calibration techniques regarding the timing of the readout window and the pixel gain can be improved using the proposed approaches in this thesis. Also, the sample mode to charge mode conversion method can be equipped in case of a miscalibrated readout window in the future due to hardware changes.

Bibliography

- [1] C. Li and B.-Q. Ma. “LHAASO discovery of highest-energy photons towards new physics”. In: *Science Bulletin* 66.22 (Nov. 2021), pp. 2254–2256. DOI: [10.1016/j.scib.2021.07.030](https://doi.org/10.1016/j.scib.2021.07.030).
- [2] J. Hinton and W. Hofmann. “Teraelectronvolt Astronomy”. In: *Annual Review of Astronomy and Astrophysics* 47.1 (Sept. 2009), pp. 523–565. DOI: [10.1146/annurev-astro-082708-101816](https://doi.org/10.1146/annurev-astro-082708-101816).
- [3] H.E.S.S. Collaboration et al. “The H.E.S.S. Galactic plane survey”. In: *A&A* 612 (2018), A1. DOI: [10.1051/0004-6361/201732098](https://doi.org/10.1051/0004-6361/201732098).
- [4] J. D. Jackson. *Classical electrodynamics*. 3rd ed. New York, NY: Wiley, 1999. ISBN: 9780471309321.
- [5] M. de Naurois and D. Mazin. “Ground-based detectors in very-high-energy gamma-ray astronomy”. In: *Comptes Rendus Physique* 16 (2015), pp. 610–627. DOI: [10.1016/j.crhy.2015.08.011](https://doi.org/10.1016/j.crhy.2015.08.011).
- [6] W. Hoffman. *The H.E.S.S. Telescopes*, URL: <https://www.mpi-hd.mpg.de/HESS/pages/about/telescopes/>.
- [7] CTA. *Gamma Rays Cosmic Sources*, URL: <https://www.cta-observatory.org/science/gamma-rays-cosmic-sources/>.
- [8] G. Giavitto et al. *A major electronics upgrade for the H.E.S.S. Cherenkov telescopes 1-4*. 2015. arXiv: [1509.01232](https://arxiv.org/abs/1509.01232) [[astro-ph.IM](#)].
- [9] F. Aharonian et al. “Calibration of cameras of the H.E.S.S. detector”. In: *Astroparticle Physics* 22.2 (2004), pp. 109–125. ISSN: 0927-6505. DOI: <https://doi.org/10.1016/j.astropartphys.2004.06.006>.
- [10] T. Ashton et al. “A NECTAr-based upgrade for the Cherenkov cameras of the H.E.S.S. 12-meter telescopes”. In: *Astroparticle Physics* 118 (2020), p. 102425. ISSN: 0927-6505. DOI: <https://doi.org/10.1016/j.astropartphys.2019.102425>.
- [11] A. Haupt et al. “The DESY Grid Centre”. In: *Journal of Physics: Conference Series* 396.4 (Dec. 2012), p. 042026. DOI: [10.1088/1742-6596/396/4/042026](https://doi.org/10.1088/1742-6596/396/4/042026).
- [12] CERN. *About ROOT*, URL: <https://root.cern/about/>.
- [13] CERN. *Python interface: PyROOT*, URL: <https://root.cern/manual/python/>.
- [14] HTCondor. *What is HTCondor?*, URL: <https://htcondor.org/description.html>.
- [15] M. S. Longair. “Cosmic rays”. In: *High Energy Astrophysics*. 3rd ed. Cambridge University Press, 2011, pp. 493–535. DOI: [10.1017/CB09780511778346.016](https://doi.org/10.1017/CB09780511778346.016).
- [16] B. Degrangé and G. Fontaine. “Introduction to high-energy gamma-ray astronomy”. In: *Comptes Rendus Physique* 16.6 (2015). Gamma-ray astronomy / Astronomie des rayons gamma, pp. 587–599. ISSN: 1631-0705. DOI: [10.1016/j.crhy.2015.07.003](https://doi.org/10.1016/j.crhy.2015.07.003).
- [17] IceCube. *Measuring Cosmic Rays*, URL: <https://masterclass.icecube.wisc.edu/en/icetop/measuring-cosmic-rays/>.
- [18] E. Fermi. “On the Origin of the Cosmic Radiation”. In: *Phys. Rev.* 75 (8 Apr. 1949), pp. 1169–1174. DOI: [10.1103/PhysRev.75.1169](https://doi.org/10.1103/PhysRev.75.1169).
- [19] T. Hassan et al. *Extragalactic source population studies at very high energies in the Cherenkov Telescope Array era*. 2017. arXiv: [1708.07704](https://arxiv.org/abs/1708.07704) [[astro-ph.HE](#)].
- [20] D. Bose et al. “Galactic and extragalactic sources of very high energy gamma rays”. In: *The European Physical Journal Special Topics* 231 (1 Jan. 2022), pp. 27–66. ISSN: 1951-6401. DOI: [10.1140/epjs/s11734-022-00434-8](https://doi.org/10.1140/epjs/s11734-022-00434-8).
- [21] D. Viganò et al. “An assessment of the pulsar outer gap model – I. Assumptions, uncertainties, and implications on the gap size and the accelerating field”. In: *Monthly Notices of the Royal Astronomical Society* 447.3 (Jan. 2015), pp. 2631–2648. ISSN: 0035-8711. DOI: [10.1093/mnras/stu2564](https://doi.org/10.1093/mnras/stu2564).

- [22] T. C. Weekes et al. “Observation of TeV Gamma Rays from the Crab Nebula Using the Atmospheric Cerenkov Imaging Technique”. In: 342 (July 1989), p. 379. DOI: [10.1086/167599](https://doi.org/10.1086/167599).
- [23] W. B. Atwood et al. “THE LARGE AREA TELESCOPE ON THE FERMI GAMMA-RAY SPACE TELESCOPE/MISSION”. In: *The Astrophysical Journal* 697.2 (May 2009), pp. 1071–1102. DOI: [10.1088/0004-637x/697/2/1071](https://doi.org/10.1088/0004-637x/697/2/1071).
- [24] D. Bose et al. “Ground-based gamma-ray astronomy: history and development of techniques”. In: *The European Physical Journal Special Topics* 231.1 (Dec. 2021), pp. 3–26. DOI: [10.1140/epjs/s11734-021-00396-3](https://doi.org/10.1140/epjs/s11734-021-00396-3).
- [25] Ν. Δημητριάδης. *Τροπική Γεωμετρία και Εφαρμογές σε Μηχανική Μάθηση και Βελτιστοποίηση*. 2020. DOI: <http://artemis.cslab.ece.ntua.gr:8080/jspui/handle/123456789/17716>.
- [26] J. Matthews. “A Heitler model of extensive air showers”. In: *Astroparticle Physics* 22.5 (2005), pp. 387–397. ISSN: 0927-6505. DOI: <https://doi.org/10.1016/j.astropartphys.2004.09.003>.
- [27] M. de Naurois. “Very High Energy astronomy from H.E.S.S. to CTA. Opening of a new astronomical window on the non-thermal Universe”. Habilitation à diriger des recherches. Université Pierre et Marie Curie - Paris VI, Mar. 2012.
- [28] M. de Naurois. “L’expérience CELESTE: Reconversion d’une centrale solaire pour l’astronomie gamma. Première observation de la Nébuleuse du Crabe et du Blazar Markarian 421 entre 30 et 300 GeV.” Michel BAUBILLIER: Président Hélène SOL: Rapporteur François LE DIBERDER: Rapporteur David SMITH Patrick FLEURY Marie Claude COUSINOU René ONG. Theses. Université Pierre et Marie Curie - Paris VI, May 2000.
- [29] S. O. Flyckt and C. Marmonier. *Photomultiplier tubes: principles and applications; 2nd ed.* Brive: Photonis, 2002.
- [30] A. J. Smith. “The MILAGRO Gamma Ray Observatory”. In: *29th International Cosmic Ray Conference (ICRC29), Volume 10*. Vol. 10. International Cosmic Ray Conference. Jan. 2005, p. 227.
- [31] A. Abeysekara et al. “On the sensitivity of the HAWC observatory to gamma-ray bursts”. In: *Astroparticle Physics* 35.10 (2012), pp. 641–650. ISSN: 0927-6505. DOI: <https://doi.org/10.1016/j.astropartphys.2012.02.001>.
- [32] G. Marsella. “Physics and astronomy results with the ARGO-YBJ experiment”. In: *Nuclear Physics B - Proceedings Supplements* 188 (2009). Proceedings of the Neutrino Oscillation Workshop, pp. 280–282. ISSN: 0920-5632. DOI: <https://doi.org/10.1016/j.nuclphysbps.2009.02.065>.
- [33] G. Di Sciascio. “The LHAASO experiment: From Gamma-Ray Astronomy to Cosmic Rays”. In: *Nuclear and Particle Physics Proceedings* 279-281 (2016). Proceedings of the 9th Cosmic Ray International Seminar, pp. 166–173. ISSN: 2405-6014. DOI: <https://doi.org/10.1016/j.nuclphysbps.2016.10.024>.
- [34] J. Kildea et al. “The Whipple Observatory 10m gamma-ray telescope, 1997–2006”. In: *Astroparticle Physics* 28.2 (2007), pp. 182–195. ISSN: 0927-6505. DOI: <https://doi.org/10.1016/j.astropartphys.2007.05.004>.
- [35] J. M. Davies and E. S. Cotton. “Design of the quartermaster solar furnace”. In: *Solar Energy* 1.2 (1957), pp. 16–22. ISSN: 0038-092X. DOI: [https://doi.org/10.1016/0038-092X\(57\)90116-0](https://doi.org/10.1016/0038-092X(57)90116-0).
- [36] T. L. Holch. “Exploring the γ -ray sky around the stellar cluster Westerlund 2 with the H.E.S.S. Experiment”. PhD thesis. Humboldt-Universität zu Berlin, Mathematisch-Naturwissenschaftliche Fakultät, 2021. DOI: <http://dx.doi.org/10.18452/22390>.
- [37] S. Ohm and S. Wagner. “Current status and operation of the H.E.S.S. array of imaging atmospheric Cherenkov telescopes”. In: *Nuclear Instruments and Methods in Physics Research Section A: Accelerators, Spectrometers, Detectors and Associated Equipment* 1055 (2023), p. 168442. ISSN: 0168-9002. DOI: <https://doi.org/10.1016/j.nima.2023.168442>.
- [38] H.E.S.S. *High Energy Stereoscopic System*, URL: <https://www.mpi-hd.mpg.de/HESS/pages/about/>.
- [39] K. Bernlöhr et al. “The optical system of the H.E.S.S. imaging atmospheric Cherenkov telescopes. Part I: layout and components of the system”. In: *Astroparticle Physics* 20.2 (2003), pp. 111–128. ISSN: 0927-6505. DOI: [https://doi.org/10.1016/S0927-6505\(03\)00171-3](https://doi.org/10.1016/S0927-6505(03)00171-3).
- [40] R. Cornils et al. “The optical system of the H.E.S.S. imaging atmospheric Cherenkov telescopes. Part II: mirror alignment and point spread function”. In: *Astroparticle Physics* 20.2 (2003), pp. 129–143. ISSN: 0927-6505. DOI: [https://doi.org/10.1016/S0927-6505\(03\)00172-5](https://doi.org/10.1016/S0927-6505(03)00172-5).

-
- [41] B. Bi et al. “Performance of the new FlashCam-based camera in the 28m telescope of H.E.S.S.” In: *Proceedings of 37th International Cosmic Ray Conference — PoS(ICRC2021)*. Sissa Medialab, July 2021. DOI: [10.22323/1.395.0743](https://doi.org/10.22323/1.395.0743).
- [42] C. Naumann et al. “New electronics for the Cherenkov Telescope Array (NECTAr)”. In: *Nuclear Instruments and Methods in Physics Research Section A: Accelerators, Spectrometers, Detectors and Associated Equipment* 695 (2012). New Developments in Photodetection NDIP11, pp. 44–51. ISSN: 0168-9002. DOI: <https://doi.org/10.1016/j.nima.2011.11.008>.
- [43] K. Bernlöhr. “Simulation of imaging atmospheric Cherenkov telescopes with CORSIKA and $\text{sim}_{telarray}$ ”. In: *Astroparticle Physics* 30.3 (2008), pp. 149–158. ISSN: 0927-6505. DOI: <https://doi.org/10.1016/j.astropartphys.2008.07.009>.
- [44] E. Bellamy et al. “Absolute calibration and monitoring of a spectrometric channel using a photomultiplier”. In: *Nuclear Instruments and Methods in Physics Research Section A: Accelerators, Spectrometers, Detectors and Associated Equipment* 339.3 (1994), pp. 468–476. ISSN: 0168-9002. DOI: [https://doi.org/10.1016/0168-9002\(94\)90183-X](https://doi.org/10.1016/0168-9002(94)90183-X).
- [45] *Science with the Cherenkov Telescope Array*. WORLD SCIENTIFIC, Feb. 2018. DOI: [10.1142/10986](https://doi.org/10.1142/10986).